Proceedings
of the
21ˢᵗ International Conference on Biomedical Applications of
ELECTRICAL IMPEDANCE TOMOGRAPHY

(EIT 2021)

Edited by Barry McDermott, Marcin J. Kraśny, Laura Farina, Niko Ištuk, Ana González-Suárez, Hamza Benchakroun, Alistair Boyle

National University of Ireland, Galway
14–16 June 2021

This document is the collection of papers accepted for presentation at the

21ˢᵗ International Conference on Biomedical Applications of Electrical Impedance Tomography
EIT 2021, Galway, Ireland.

Layout design:
Marcin J. Kraśny

Photo credits (front & back cover):
Dr Chaosheng Zhang @ZhangChaosheng

NUI Galway Translational Medical Device Lab
National University of Ireland
Galway,
University Road,
Galway, Ireland
H91 TK33
https://tmdlab.ie

eit2021.ie

Table of Contents

About the Event

The National University of Ireland Galway, and the Translational Medical Device Lab are pleased to host the 21st International Conference on Biomedical Applications of Electrical Impedance Tomography (EIT2021). The conference has been organised by Barry McDermott, Marcin J. Kraśny, Laura Farina, Niko Ištuk, Ana González-Suárez, Hamza Benchakroun, Alistair Boyle.

We regret you are not able to be with us in Ireland for the conference due to the ongoing pandemic but have been delighted by the support shown by the electrical impedance tomography (EIT) community for the event.

This is testament to the resilience and strength of the conference, EIT, and you the researchers and delegates.

The conference gives a platform for investigators in all aspects of EIT and related areas such as bioimpedance to converse on common fields of interest, whilst also being an opportunity for the community to broaden its outlook in clinical applications and new technologies. This interaction and opportunity to share cutting edge research is key to the development of impedance tomography and its applications. We hope you have an enjoyable and productive couple of days as our virtual guest here in Galway.

Céad míle fáilte romhaibh go léir go Gaillimh.
EIT 2021 Organising Committee

Organising Committee

Barry McDermott

Dr Barry McDermott is a Senior Research Fellow and Adjunct Lecturer in both the School of Engineering, and the School of Medicine at NUI Galway. Barry holds a Ph.D. in Medical Device Engineering with his thesis based on EIT applied to the stroke problem. Additionally Barry holds professional level degrees in Engineering, Pharmacy and Veterinary Medicine. Barry's research includes EIT applied to clinical problems, but he also actively works on the development of innovative therapeutics for conditions such as osteoarthritis, and particularly is interested in the interface between drugs and devices.

Niko Ištuk

Niko is a Marie Skłodowska-Curie Fellow in Innovative Training Network EM-ERALD. He is currently working towards his PhD in Electrical and Electronic Engineering at the National University of Ireland Galway under the supervision of Dr Martin O'Halloran. His main research area is characterisation of tissue dielectric properties. Niko received his BSc in Electrical Engineering and Information Technology in 2010. and MSc in Communication and Information Technology in 2013, both from University of Split.

Laura Farina

Dr Laura Farina is a Research Fellow in the Translational Medical Device Laboratory, NUI Galway, and Adjunct Lecturer at the School of Engineering, NUI Galway. She received her Ph.D. in ICT (Applied Electromagnetism) in 2017, from Sapienza University of Rome, and she was a Marie Skłodowska-Curie MedTrain Fellow at CÚRAM, NUI Galway, from 2018 to 2020. Laura's research interests include novel electromagnetic-based medical applications, from thermal treatments optimisation to innovative monitoring solutions, through accurate characterisation of the electrical properties and physiological changes of the biological tissue.

Marcin J. Kraśny

Dr Marcin J. Kraśny is a postdoctoral researcher in the Smart Sensors Lab in the School of Medicine at NUIG working on impedance-based ablation assessment system for improved atrial fibrillation treatment. He holds a PhD in the field of characterisation of piezoelectric materials for energy harvesting applications from the University of Bath (UK). His previous work includes development of EIT systems and electrical characterisation of gels used for MRI phantoms. He worked for several years in industry as an electronics engineer. Marcin received his M.Sc.Eng. degree in Electronics and Communication with specialisation in Microsystems from the Wrocław University of Science and Technology (Poland).

Ana González-Suárez

Dr Ana González-Suárez is a Senior Research Fellow in the Translational Medical Device Lab and Adjunt Lecturer in the School of Engineering at NUI Galway. She received her Ph.D. in Biomedical Engineering from Universitat Politècnica de València (Spain) focused on RF ablation techniques for removing cardiac arrythmias and tumors in a minimally invasive way. She conducted research stays at Wellman Center for Photomedicine, Massachusetts General Hospital-Harvard Medical School (Boston, USA) and at Mount Sinai Hospital (New York, USA). Ana's research interests include the development of a disruptive solution to treat cardiac arrhythmias in collaboration with AtriAn, which is an Irish Medical Device company based in Galway.

Hamza Benchakroun

Hamza Benchakroun is a Ph.D. student in the Translational Medical Device Lab. His AuriGen Medical funded project involves an investigation into a reliable probe set up to measure the electrical properties of biological tissues in order to improve arterial fibrillation therapy using optimised pulsed field ablation. He is a graduate of The Faculty of Sciences Semlalia of Marrakech, Morocco in Electronics Engineering and Industrial Computing, and holds a Masters degrees in Electrical and Telecommunication Engineering at Abdelmalek Essaadi University, Tetouan, Morocco with first-class honours. After his Masters degree, he spent two years working with The Institute of Telecommunications and Multimedia Applications (iTEAM) in the scientific park at the Polytechnic University of Valencia developing systems for Microwave Breast Cancer Imaging.

Alistair Boyle

Dr Alistair Boyle is CTO at Kite Medical, an Irish company developing an EIT-based system to detect kidney reflux (vesicoureteral reflux, VUR) in young children. VUR is a condition where urine flows backwards from the bladder to kidneys. Alistair holds a PhD and MASc from Carleton University, Canada where he focused on EIT electrode movement in biomedical and geophysical settings. He previously worked in integrated circuit design at small startups and large international companies.

Conference Sponsors

Session 1: Thorax I

Patient Specific Adaptation in Neonatal Chest EIT

Nima Seifnaraghi[1], Serena de Gelidi[1], Merja Kallio, Inéz Frerichs, Erich Sorantin, Andrew Tizzard[1], Andreas Demosthenous Richard H. Bayford[1]

[1]Middlesex University, n.seifnaraghi@mdx.ac.uk

Abstract: An algorithm is designed to estimate the closest match to the actual patient model via applying an absolute/static imaging technique prior to EIT monitoring. Probabilities are assigned based on observed images, nominating a candidate patient thoracic cross-section model from a pre-stored model library. Implementing the updated models instead of the in use default model, may improve the calculated clinical parameters by 250% to 400% using GREIT and tSVD reconstructions respectively.

1. Introduction

One the superior features of EIT technique is its non-invasiveness. However, the assumed thoracic cross-section model plays a crucial role within the solution to reconstruction inverse problem and moreover, in estimating some of the clinical parameters such as silent spaces (the parts of the lungs with little tidal ventilation). The model needs to cover the domains occupied by the heart, left and right lungs in addition to thorax boundary and electrode positions. While the latter issue can still be addressed non-invasively by embedding gravity sensors in EIT belt [1] the former one could be done by either CT-scans or MRI imaging. In infants even MRI faces challenges such as sedation, time and financial costs. Consequently, the computations are often performed based on a pre-assumed model. The presented algorithm is able to provide a closer match to each individual patient with no additional hardware setups.

2. Methods

The method acts as a calibration step in advance to EIT recording. Employing the externally achieved information a homogeneous thorax cross-section is formed and an image is reconstructed applying Gauss-Newton absolute imaging. Meanwhile all the library models are scaled according to the perimeter of the patient thorax at the level of the EIT belt. The internal domains of these scaled models are taken out and fitted to the known exterior boundary of the patient thorax. Hence at this point the candidate models all share the same exterior contour but they are different in their interior organ domain configurations (see Fig.1).
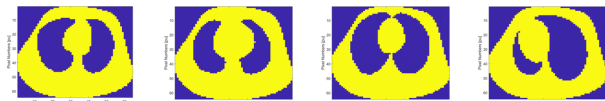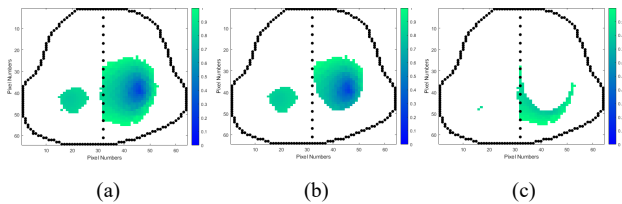

Figure 1: Fitted internal configurations in the estimated thorax contour. The absolute image is then used to evaluate which model is the most likely to be responsible for the measured surface potentials. This is done by pixelating the reconstructed image -an example is shown in Fig. 2- and assigning the pixels to various sets. These sets are representing the pixels each M_j could enclose with its corresponding domain (Γ_{*j}) and the ones which cannot be covered (Λ_{*j}). An example of such procedure in case of real patient is shown in Fig. 3.

Using these subsets the likelihood for each M_j can be defend (1).
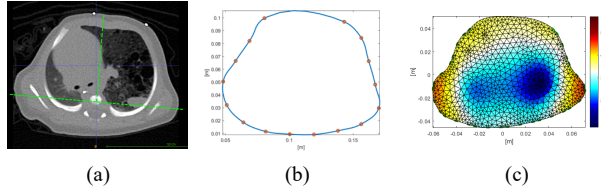
**Figure 2:** (a) CT-scan, (b) estimated boundary, (c) reconstructed image.

Figure 3: (a) sets S_l and S_r, (b) subsets Γ_{l32} and Γ_{r32}, (c) Λ_{l32} and Λ_{r32}.

$$\mathcal{L}(M_j, \mathcal{O}) = \left(\frac{\sum_\mathbf{x} \delta(\mathbf{x} - \mathbf{x}_{\Gamma_{lj}})}{\sum_\mathbf{x} \delta(\mathbf{x} - \mathbf{x}_{\phi_{lj}})} - \frac{\sum_\mathbf{x} \delta(\mathbf{x} - \mathbf{x}_{\Lambda_{lj}})}{\sum_\mathbf{x} \left(\delta(\mathbf{x} - \mathbf{x}_{\Psi_l}) - \delta(\mathbf{x} - \mathbf{x}_{\phi_{lj}}) \right)} \right) \cdot \left(\frac{\sum_\mathbf{x} \delta(\mathbf{x} - \mathbf{x}_{\Gamma_{rj}})}{\sum_\mathbf{x} \delta(\mathbf{x} - \mathbf{x}_{\phi_{rj}})} - \frac{\sum_\mathbf{x} \delta(\mathbf{x} - \mathbf{x}_{\Lambda_{rj}})}{\sum_\mathbf{x} \left(\delta(\mathbf{x} - \mathbf{x}_{\Psi_r}) - \delta(\mathbf{x} - \mathbf{x}_{\phi_{rj}}) \right)} \right). \tag{1}$$

where $\mathbf{x}$ represents pixels spatial coordinates and $\mathcal{O}$ is the observed absolute image. The posterior probability $P\{M_j|\mathcal{O}\}$ can be calculated using the Bayesian theory. The algorithm then selects the model with the highest probability and updates the prior model for further reconstruction during the EIT monitoring. The capability of method at selecting the proper model has been validated against tank data [2], simulated data and one rare patient who was monitored by EIT as well as undergoing CT-scan. For further details, please refer to [3].

3. Conclusions

The significant impact on the computation of silent spaces for the lungs applying GREIT and tSVD reconstructions is evident. As an example mean values of 10 consecutive breaths for the detected patient model against three models including the second most probable and the two least probable ones from the library are shown in Fig. 4.
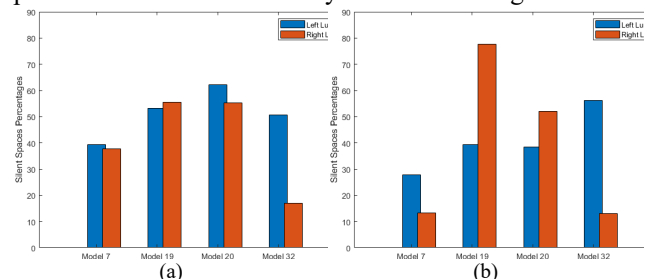
Figure 4: Extracted silent spaces using (a) GREIT, and (b) tSVD.

References

[1] S. de Gelidi et al. *PhysiolMeas*, 39: 74001, 2018.
[2] D. Isaacson et al. *IEEE Trans. Med. Imaging*, 821–828, 2004.
[3] N. Seifnaraghi et al., *TBME,* doi: 10.1109/TBME.2021.3053463.

Mechanical Ventilation Control System Guided by Electrical Impedance Tomography

Zhixi Zhang[1], Hao Yu[1], Kang Fu[1] and Jiabin Jia[1]

[1]Agile Tomography Group, Institute for Digital Communication, School of Engineering, The University of Edinburgh,
Zhixi.Zhang@ed.ac.uk

Abstract: The mechanical ventilator is a piece of developed medical equipment and has become indispensable for critically ill patients. The conventional ventilator control strategy relies on lung pressure or volume. This work implements a ventilator control system guided by electrical impedance tomography (EIT) in simulation.

***Index Terms*:** Electrical impedance tomography, PID controller, mechanical ventilation, respiratory systems.

1 Introduction

For critically ill patients who suffer from acute respiratory illness and even fatal acute respiratory distress syndrome (ARDS) [2], the mechanical ventilator is their lifeline. Pressure control and volume control are conventional ventilator control modes. However, both pressure and volume only provide a total value related to lungs, regardless of localised lung condition.

The basic principle of EIT is that different tissues in the human body have different electrical conductivities under different physiological and pathological conditions [4]. Real-time lung images captured by EIT can add extra impedance information into the ventilator control loop to enhance safety, comfort, and liberation of mechanical ventilation.

2 Mechanical ventilation guided by EIT

Since lung volume changes can be monitored from the EIT images, real-time EIT can be included in feedback control for the ventilator. The EIT-guided closed-loop ventilation control system is described in Fig.1.

The system is divided into the controller, blower, lung model, and EIT measurement. The lung model consists of the chest, lungs and electrodes. Other body parts are ignored for simplicity. The respiratory cycles are simulated by adjusting the internal electrical conductivity of the lungs. The lung conductivities at end-expiratory state and end-inspiratory state are set as 0.12 mS/m and 0.06 mS/m respectively. The amplitude of excitation current is 10mA. The response voltages are recorded to reconstruct cross-sectional lung images.

Assuming that both lungs are cylinder, that is, the cross-sectional areas of different heights are the same, so the relationship between the cross-section and volume of the lungs can be obtained. The reference value is a preset ideal tidal volume change, and the output is the tidal volume the ventilator produced. The first transform module before the EIT module converts tidal volume into the lungs conductivity. The output of the EIT module is the reconstructed images. The second transform module after the EIT module extracts the lung tidal volume from the cross-sectional area of the lungs. Finally, the lung tidal volume is fed back to the system to compare with the reference value.
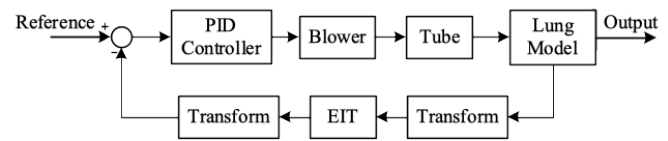

Figure 1: Structure of EIT-guided ventilation system.

3 Results

The images of EIT in Fig. 2. show one respiratory cycle in simulation with 50dB white Gaussian noise. An evident conductivity change can be observed in the cross-sectional lung images. The simulation results of the control system in Fig.3 demonstrates two different patient cases. The left one indicates a normal case, where the patient has no spontaneous breathing. The right one is an anesthesia case, where the spontaneous breathing of the patient is weakened gradually. They show that the controlled tidal volume closely tracks the reference values, however the error is relatively larger at the peak, and there is a slight delay between the two values, due to the moment of inertia of the blower.
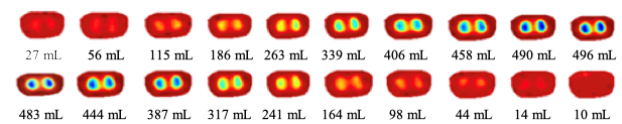
Figure 2: Lung volume in a breathing cycle measured using EIT with 50dB white Gaussian noise.
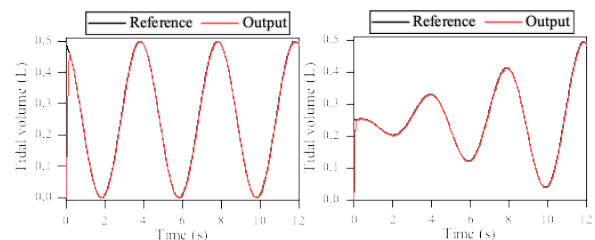
Figure 3: Controlled tidal volume cycle.

4 Conclusions

The real-time 2D EIT image can provide more comprehensive lung information than pressure and volume to guide the mechanical ventilation control system and make timely adjustments as demonstrated in the simulation results. The ongoing work is estimating realistic 3D lung volume based on the EIT images. In addition, we are working on a demo ventilator with an EIT imaging system to test overall performance.

References

[1] H. F. J. Tregidgo, M. G. Crabb, A. L. Hazel, and W. R. B. Lionheart, "On the feasibility of automated mechanical ventilation control through EIT," IEEE Trans. Biomed. Eng., vol. 65, no. 11, pp. 2459–2470, 2018.

[2] T. J. Kao et al., "Real-time 3D electrical impedance imaging for ventilation and perfusion of the lung in lateral decubitus position," 2014 36th Annu. Int. Conf. IEEE Eng. Med. Biol. Soc. EMBC 2014, pp. 1135–1138, 2014.

Respiration Monitoring in PACU using EIT: A Feasibility Study

Hee Yong Kang[1], Ann Hee You[1], You Jeong Jeong[2], Geuk Young Jang[2], Tong In Oh[2],
Yongmin Kim[3] and Eung Je Woo[2]

[1]Department of Anesthesiology and Pain Medicine, Kyung Hee University Hospital, Seoul, Korea
[2]Department of Biomedical Engineering, College of Medicine, Kyung Hee University, Seoul, Korea, tioh@khu.ac.kr
[3]Department of Creative IT Engineering, POSTECH, Pohang, Korea

Abstract: The importance of perioperative respiration monitoring is highlighted by high incidences of postoperative respiratory complications. In order to detect hypoventilation and respiratory events using EIT device and the sidestream capnography, we did an observational study with 13 non-intubated patients in PACU after general anesthesia.

1 Introduction

Respiratory depression and hypoventilation due to residual anesthetics and the use of opioids cause hypoxemia and hypercapnia and may lead to permanent disability or life-threatening complications, e.g., organ failure, brain damage, coma, and death, in post-anesthesia care unit (PACU) [1]. Therefore, respiration monitoring would be needed in these situations. Currently, monitoring of peripheral oxygen saturation (SpO$_2$) and/or end-tidal carbon dioxide (EtCO$_2$) are commonly used to detect hypoxemia or hypercapnia. However, they often trigger false/delayed alarms and/or causes alarm fatigue.

In this study, we used an EIT system with the sidestream capnography to simultaneously measure all of TV (tidal volume), RR (respiration rate), MV (minute ventilation), SpO$_2$, and EtCO$_2$ from non-intubated patients in PACU after total knee arthroplasty. We acquired ventilation and gas exchange parameter values breath-by-breath and assessed their capability in detecting hypoventilation and respiration events.

2 Methods

The Capnostream^{TM}35 (Medtronic, U.S.A) measured the sidestream capnography signal and SpO$_2$, and output EtCO$_2$ and RR$_{Cap}$ derived from the capnography signal. In addition, it detected apneic events and provided the Integrated Pulmonary Index (IPI) [2]. TV, MV, and RR$_{EIT}$ were simultaneously measured using an electrical impedance tomography (EIT) device (AirTom^{TM}-R, BiLab, Korea) originally developed for regional lung ventilation imaging [3, 4]. The respiratory status of each patient was monitored for about 60 minutes after transferred to PACU. During the first half of the period, 4 L/min (36% FiO$_2$) of oxygen was provided to each patient through an oronasal cannula. It was removed for the other half of the period. This clinical study protocol was approved by the Institutional Review Board at Kyung Hee University Hospital (KHUH-2019-08-058-007).

We used the respiratory volume signal (RVS) and TV data to detect respiratory events of apnea, hypopnea, bradypnea, and inspiratory breath-hold (IBH). In order to determine the respiratory event, we assumed the predicted normal TV (TV$_{PRED}$) and predicted normal MV (MV$_{PRED}$) for each patient [5].

Fig. 1 is an example of the acquired respiratory signals from patient #7 using the AirTom-R and Capnostream^{TM}35. The IPI alarm was continuously turned on between 24 and 36 minutes, most likely by the low RR$_{Cap}$ values during the same time interval. However, this IPI alarm was false positive since the TV values during the same time period were large, and the MV values were mostly above $0.4 \times$ MV$_{PRED}$. On the other hand, the MV value became relatively low between 36 and 54 minutes due to the significantly reduced TV values. It caused a desaturation in SpO$_2$ with a time delay and an increase in EtCO$_2$. The IPI fluctuated during this time period but mostly staying above the alarm threshold of 3. This hypoventilation period was ended by a clinician's respiratory intervention at 54 minutes, resulting in the TV and MV values increasing above $0.4 \times$ MV$_{PRED}$.
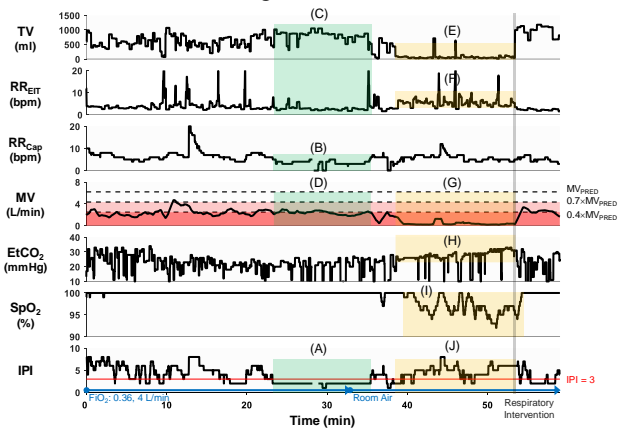
Figure 1: Measured respiratory signals (TV, RR$_{EIT}$, RR$_{cap}$, MV, EtCO$_2$, SpO$_2$, IPI) in PACU after general anaesthesia.

3 Conclusions

Perioperative respiration monitoring to detect incidences of hypoventilation, oxygen desaturation and respiratory events reliably and timely needed with various signals such as TV, RR, MV, and SpO$_2$. More clinical studies are needed to develop a new index.

4 Acknowledgements

References

[1] LA Lynn, *et al.*, *Patient Saf. Surg*, 5:3, 2011
[2] M Ronen, *et al.*, *J Clin Monit Comput*, 31:435-442, 2017
[3] TI Oh, *et al.*, *Physiol. Meas*, 32:835-849, 2011
[4] GY Jang, *et al*., *Sci Rep*, 10:11242, 2020
[5] ARDSnet, *NIH-NHLIB ARDS Network*, 2008

Early individualized PEEP guided by EIT in ARDS: a randomized controlled clinical trial

Huaiwu He[1], Chi Yi[1], Yun Long[1*], Siyi Yuan[1], YingYing Yang[1], Zhanqi Zhao[2,3]

[1]Department of Critical Care Medicine, Peking Union Medical College Hospital, Peking Union Medical College, Chinese Academy of Medical Sciences, Beijing, China, *iculong_yun@163.com
[2]Department of Biomedical Engineering, Fourth Military Medical University, Xi'an, China
[3]Institute of Technical Medicine, Furtwangen University, Villingen-Schwenningen, Germany

Abstract: The objective was to determine whether early PEEP titration with EIT improved outcomes in ARDS. A total of 117 ARDS patients were randomly assigned to EIT group or control group. Mortality rate was lower but not statistically significant in the EIT group (23% vs. 29%). Significant lower SOFA was found in EIT.

1 Introduction

Positive end-expiratory pressure (PEEP) is often used in acute respiratory distress syndrome (ARDS) with the aim to open collapsed lung regions and keep the lung open. However, inappropriate setting of PEEP may induce further injury to the lung tissue. It remains challenging for the physicians to balance the regional recruitment and overdistension during the PEEP setting.

More and more clinical studies have validated the use of Electrical impedance tomography (EIT) for guiding the PEEP setting in various clinical conditions such as ARDS, acute hypoxemia, general anesthesia and post-operative cardiac surgery patients at the bedside [1-3]. However, no randomized controlled trial has been conducted to compare PEEP setting using EIT and the lower PEEP/FiO_2 table [4] in ARDS patients. The aim of this randomized controlled study was to explore whether PEEP setting guided by EIT could improve outcomes compared to PEEP/FiO_2 table from the ARDS Network in ARDS patients.

2 Methods

The study was approved by the Institutional Research and Ethics Committee of the Peking Union Medical College Hospital. Informed consent was obtained from all patients or next of kin before data were included into the study.

A total of 191 ARDS patients were screened and 126 were enrolled: 63 patients in the EIT group and 63 in the control group. Two patients in the EIT group and 7 patients in the control group were erroneously randomized because of mis-classification of ARDS. Thus, 117 subjects (61 EIT group, 56 control group) were included in the primary analysis.

Patients assigned to the control group continued to receive the low-PEEP strategy using the PEEP/FiO_2 table of the ARDS Network protocol. In the EIT group, PEEP titration by EIT was performed at the enrolment with a method described previously [5]. The optimal PEEP determined by EIT was applied for 24 hours. Afterwards, PEEP was set by the attending physician based on the low PEEP/FiO_2 table. EIT measurements were performed with PulmoVista 500 (Dräger Medical, Lübeck, Germany). EIT measurements were continuously recorded at 20 Hz when the patients were at relatively stable condition after medical treatment. Apart from the PEEP selection scheme at the day 1, other aspects of care such as small tidal volume ventilation and adjuvant therapies of ARDS were the same for both groups based on local ARDS therapy regulation in our department.

3 Results

On day 28 after randomization, the death from any causes had occurred in 14 of 61 patients (23%) in the EIT group and 16 of 56 patients (28.5%) in the control group (P = 0.487). There were no significant differences in ventilator-free day at day 28, rate of successful extubations, length of ICU day, adjuvant therapies of ARDS between the groups. The incidence of new barotrauma was zero.

Sequential organ failure assessment (SOFA) was calculated and compared. Significantly lower SOFA at day 1 and at day 2 compared to day 0 were found in the EIT group. Moreover, the EIT group exhibited a significant decrease of SOFA at day 2 compared with day 0 (paired t-test, difference by -1 (-3.5, 0), p=0.001). However, the control group did show a similar decrease (difference by 1 (-2, 2), p=0.131).

4 Discussion and Conclusion

As limitations, the study was not blinded, and the severities of ARDS in the study groups were different. Besides, more than 40% of patients received prone positioning in this study, which might be a confounding factor that limited the effect of PEEP titration.

Nevertheless, early individualized PEEP setting by EIT might results in a faster early recovery of organ function. Our study did not find optimal PEEP by EIT to decrease mortality in patients with ARDS, possibly because of the limited study power. Whether individualized PEEP setting by EIT in ARDS can decrease mortality should be assessed in a future clinical trial.

References

[1] K Liu, C Huang, M Xu, et al. *Ann Transl Med* 7:757, 2019
[2] Z Zhao, MY Chang, MY Chang, et al. *Annals of intensive care* 9:7, 2019
[3] J Karsten, C Grusnick, H Paarmann, et al. *Acta Anaesthesiol Scand*, 59:723-732, 2015
[4] RG Brower, PN Lanken, N MacIntyre, et al *N Engl J Med*, 351:327-336, 2004
[5] EL Costa, JB Borges, A Fau-Melo et al. *Intensive Care Med* 35:1132-7, 2009.

Exploring Respiratory Motion Tracking through EIT

Qi Wang[1], Xin Ding[1] and Jiabin Jia[2]

[1]School of Electronics and Information Engineering, Tianjin Polytechnic University, Tianjin, China, wangqitju@163.com
[2]School of Engineering, The University of Edinburgh, Edinburgh, UK

Abstract: In this paper, preliminary research of lung movement during the respiratory process is first studied based on Electrical impedance tomography(EIT).A modified total variation (MTV) algorithm is used for the estimation of lung volume and movement based on 3D EIT images, which improve the quality of reconstruction by approximately 30% and 20% compared with the traditional Tikhonov method and the total variation (TV) method, respectively.

1 Introduction

Most of the applications and researches for lung EIT only focus on the estimation of the lung volume, i.e. ventilation and perfusion based on reconstructed images [1]-[3]. In this paper, the respiratory motion of lung is first monitored based on EIT reconstructions. The real 3D thorax models for specific statuses, i.e. end-expiration and end-inspiration, are built based on CT slices for the simulation study. A MTV algorithm is proposed for 3D reconstruction to improve the estimation accuracy of lung movement. Lung characteristics and respiratory motion are studied based on 3D lung EIT images of different respiratory statuses.

2 Methods

2.1 3D model construction for EIT forward problem

According to the movement of the lungs in the thoracic cavity, a realistic three-dimensional chest model with two specific states (end-inspiration and end-expiration) is constructed.According to the 3D effect of the electric field, both on and off plane images could be reconstructed through measured data from one electrode plane.To evaluate the image quality on each plane, the relative errors between the reconstructed image and the real conductivity distribution on each layer are calculated and plotted.To improve spatial resolution on the z-axis and reduce the influence of off-plane objects, we select 20 reconstruction layers 5 cm apart between adjacent rings to cover the whole thorax area. The models with 5 electrode rings are shown in fig.1

(a)　　　　　**(b)**
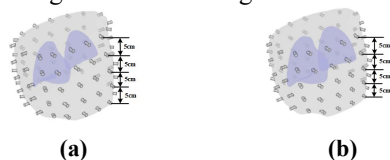
Figure 1: 3D thorax models with 5 electrode rings. (a) end-expiration status; (b)end-inspiration status.

.2.2 The improved TV algorithm based on split-bregman iteration

To preserve sharp boundaries and improve the accuracy of the reconstructed image，this paper applies the MTV regularization scheme to 3D EIT.

$$\arg \min_{\sigma,u}\left\{\|V - J\sigma\|_2^2 + \lambda_1\|\sigma - u\|_2^2 + \lambda_2\|u\|_{TV}\right\} \text{(1)}$$

where λ_1 and λ_2 are the regularization parameters, and u is the auxiliary variable.

3 Conclusions

In fig. 2, 3D reconstructions of lung images are achieved utilizing the Tikhonov algorithm, TV algorithm, and MTV algorithm, respectively.
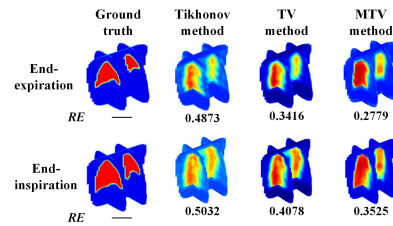
Figure 2: 3D lung reconstruction results based on simulation data.

From fig. 2, the 3D reconstructed images can suggest the variation of lung volumes under different respiratory statuses. The reconstruction results of the MTV regularization improve the edge-preserving performance in the inversion result compared with the Tikhonov and traditional TV methods.

(a)

(b)
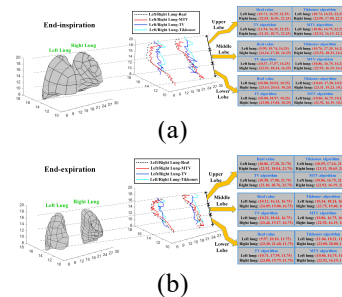
Figure 3: The center of lung lobe obtained from EIT reconstruction with simulation data. (a) end-expiration status. (b) end-inspiration status.

From fig.3,the ones calculated based on the MTV image is closer to the true position.

References

[1] X. Li, X. Chen, Q. Wang, J. Wang, X. Duan, Y. Sun and H. Wang, "Electrical-impedance-tomography imaging based on a new three-dimensional thorax model for assessing the extent of lung injury," AIP Adv., vol. 9, no. 12, 125310, 2019.

[2] M. Kircher, G. Elke, B. Stender, M. Hernandez Mesa, F. Schuderer, O. Dollel, M. K. Fuld, A. F. Halaweish, E. A. Hoffman, N. Weiler and I. Frerichs, "Regional lung perfusion analysis in experimental ARDS by electrical impedance and computed tomography," IEEE Trans. Med. Imaging, vol. 40, no. 1, pp. 251-261, 2021.

Changes in Tidal Volume of Respiratory Events from OSA Patients during Overnight Polysomnography

Tae Wook Chang[1], Tingting Zhang[1], Geuk Young Jang[1], Tong In Oh[1], Yongmin Kim[2],

Eung Je Woo[1]

[1]Department of Biomedical Engineering, College of Medicine, Kyung Hee University, Seoul, Korea, tioh@khu.ac.kr
[2]Department of Creative IT Engineering, POSTECH, Pohang, Korea

Abstract: Targeting the patients of obstructive sleep apnea-hypopnea syndrome (OSAS) diagnosed through the routine polysomnography (PSG), EIT was exploited to analyse the changes of ventilation volume based on six types of sleep respiration disorders, and the changes of ventilation were compared between event period and post-event period.

1 Introduction

Obstructive sleep apnea syndrome (OSA) occurs due to repeated decreases or temporary cessation of airflow due to obstruction of the upper airway during sleep. Overnight polysomnography (PSG) is currently used as the standard diagnostic method for OSA. The severity of OSA is categorized as the apnea-hypopnea index based on the changes of PSG signals included nasal pressure and oronasal thermistor [1]. However, oversimplified AHI is insufficient to describe the physiological phenomena of complicated sleep-related breathing disorder events without considering the actual ventilation of the lungs. Also, there were not many studies about the physiological changes in hypopnea combined with oxygen desaturation or arousal. In this study, the measurements of electrical impedance tomography (EIT) [2] were performed on OSA patients during overnight-PSG in order to analyze the changes in tidal volume (TV) according to various sleep respiration disorders.

2 Methods

The synchronized PSG signals and EIT images were collected from 8 subjects aging from 19 to 75. All of them suffered from the OSA with an AHI of 5 or higher. Through PSG analysis, the following six sleep-related breathing disorder events (Flow limitation (FL), respiratory effort-related arousal (RERA), arousal hypopnea (Ha), arousal & desaturation hypopnea (Had), desaturation hypopnea (Hd), and apnea (A)) were identified according to the conventional AASM rule [3], and the event type and period were determined.
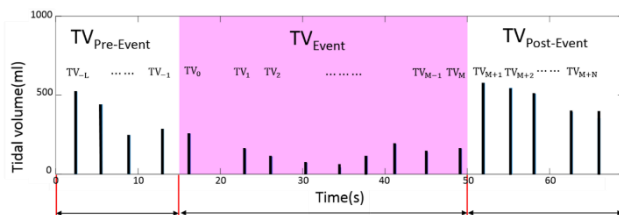

Figure 1: Breath by breath TV values in pre/during/post respiratory events obtained by EIT images.

From the respiratory volume signal extracted from the reconstructed EIT images [4] measured simultaneously, the TV change during (TV_{Event}) and after ($TV_{Post-Event}$) the above six events was calculated in % units with respect to the TV just before the event. Fig. 1 shows an example of TV changes before and after the occurrence of an apnea event.

3 Results

The mean TV during all hypopneas and apneas were reduced, as shown in Fig 2. Among three different hypopnea types, the reductions in TV during Hd and Had were greater than those during Ha, while the TV reductions during Ha and FL were similar. After RERA, Ha, Had and apnea, there was an overshoot in tidal volume values, whereas there was no overshoot after FL and Hd.
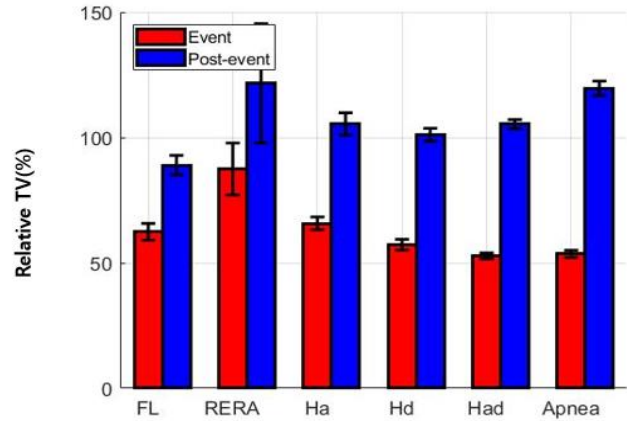
Figure 2:. The relative tidal volume changes (in percentage) during and after each specific respiratory event.

4 Conclusions

From the EIT measurements during overnight PSG, the TV changes between event and post-event were compared to pursue deeper insights into the influence of each sleep-related breathing disorder on the amount of ventilation. It would be necessary to take into account the TV and AHI togeterh to diagnosis the severity of OSA.

5 Acknowledgements

References

[1] J Durán, S Esnaola , et al. *American journal of respiratory and critical care medicine*, 163: 685-9, 2001.
[2] F Sériès, I Marc. *Thorax,* 54: 506-510, 1999.
[3] RB Berry, L Claude, SM Albertario, RM Harding, DT Lloyd et. al. *The AASM manual for the scoring of sleep and associated events: rules, terminology, and technical specifications*, 2018
[4] T Zhang, GY Jang, TI Oh, KW Jeung, H Wi, EJ Woo *SIAM Journal on Applied Mathematics*, 80: 499-520, 2020

Assessment of the Anti-Gravity Straining Manoeuvre using electrical impedance tomography

Lin Yang[1], Meng Dai[2], Feng Fu[2] and Zhanqi Zhao[2,3]

[1]Department of Aerospace Medicine, Fourth Military Medical University, Xi'an, China
[2]Department of Biomedical Engineering, Fourth Military Medical University, Xi'an, China
[3]Institute of Technical Medicine, Furtwangen University, Villingen-Schwenningen, Germany
Zhanqi.zhao@hs-furtwangen.de

Abstract: High gravity imposes substantial physiological demands on the pilot. Anti-gravity straining manoeuvre helps to reduce the occurrence of gravity-induced loss of consciousness. This study evaluated the feasibility of using electrical impedance tomography to assess the performance of anti-gravity straining manoeuvre.

1 Introduction

High gravity imposes substantial physiological demands on the pilot. Anti-gravity straining manoeuvre (AGSM) helps to reduce the occurrence of gravity-induced loss of consciousness. The pilot should strain skeletal muscles (mainly lower body parts) to prevent the blood pooling in the lower extremities. Simultaneously, the pilot needs to take a preparatory inspiration of less than 1 s and forcefully exhale for 3-4 s against a partially or completely closed glottis to increase intrathoracic and intra-abdominal pressure. Systemic arterial blood pressure of aortic valve at the heart level would increase, and thereby minimize the blood pressure reduction. With AGSM, the pilot can maintain adequate cerebral blood perfusion to withstand the sustained hyper +Gz force (high G in the direction from head to toe).

The training is intense, however, no tools can judge whether the trainees have performed the AGSM correctly or not. Electrical impedance tomography (EIT) is a real-time imaging tool to monitor ventilation. This study evaluated the feasibility of using EIT to assess the performance of AGSM.

2 Methods

The study protocol was approved by local Ethics Committees. Ten undergraduates and three teachers majoring in aerospace medicine, who were familiar with the technique of AGSM, were included in the study. An experienced professor from the department of aerospace medicine reviewed the key points of AGSM (L-1 manoeuvre) with each subject. The professor rated the performance of the subjects after the subjects considered they had managed the manoeuvre (maximum 16 points when it satisfied all criteria). EIT measurement was simultaneously performed during the AGSM. The professor reviewed the impedance-time curves recorded with EIT and rated the subjects' performance again accordingly. The results were compared with student t-test. A p value < 0.05 was considered to be statistically significant.
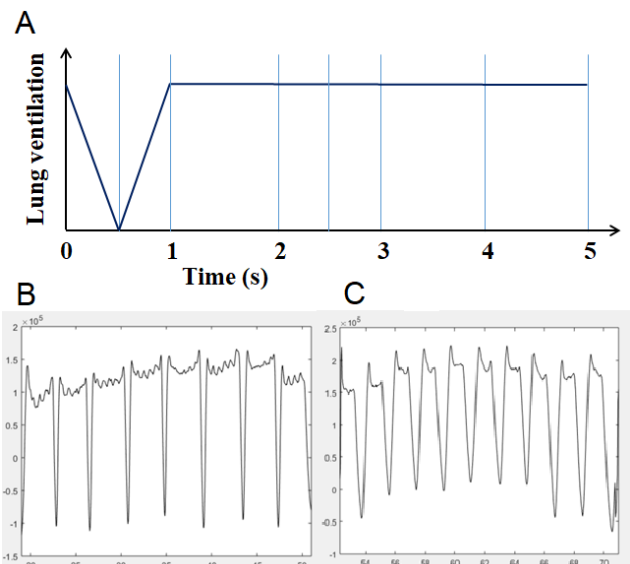
Figure 1: A, ideal L-1 manoeuvre; B, measurement recorded from a teacher and C, record from a student.

3 Results

The ideal curve and two examples of EIT impedance-time curves are plotted in Fig. 1. The rating scores with help of EIT was significantly lower than that without any help ($p<0.0001$; Table 1).

Table 1: Summary of the rating regarding the performance (maximum 16 points).

subject number	rating w/o EIT	rating with EIT
1	13	7
2	11	7
3	16	12
4	15	10
5	14	8
6	15	10
7	14	7
8	16	9
9	15	12
10	12	7
11	16	8
12	15	13
13	15	14

4 Conclusion

EIT is able to provide useful information for the trainers to evaluate the performance of AGSM from the trainees and may help to improve their learning.

Detection of Different COVID-19 Pneumonia Phenotypes with Bedside Electrical Impedance Tomography

Rongqing Chen[1], András Lovas[2], Balázs Benyó[3], Knut Möller[1]

[1]Institute of Technical Medicine, Furtwangen University, rongqing.chen@hs-furtwangen.de
[2]Department of Anesthesiology and Intensive Therapy, University of Szeged
[3]Department of Control Engineering and Information Technology, Budapest University of Technology and Economics

Abstract: In this contribution, alveolar overdistention and collapse was analysed on two severe COVID-19 pneumonia patients with long-term EIT monitoring. The result showed different reactions of COVID-19 phenotypes to the PEEP trial, revealed the progressive status change, and indicted a possible phenotype transition in one patient.

1 Introduction

COVID-19 induced acute respiratory distress syndrome (ARDS) could have two different phenotypes due to the fact that more than 50% of the patients were observed to have severe hypoxemia, but with a near normal respiratory system compliance[1]. These patients were called L-type patients characterized by low recruitability, while H-type patients in contrast are with high recruitability. The reaction of the L-type patients to the PEEP trial is not as good as that of H-type patients. Sometimes the higher PEEP might induce lung injuries which will eventually compromise the outcome. A common method to identify the different COVID-19 pneumonia phenotype is through CT scans. However, daily CT scans on a severe COVID-19 patient is not practical while the course is developing fast. It is suggested that the EIT bedside monitoring can play an important role detecting the different phenotypes of the COVID-19 pneumonia in addition to CT examination[2]. The objective of this work is to show the insight of a possible EIT method to provide supplementary information for the COVID-19 phenotype diagnosis in terms of alveolar collapse and overdstention estimation.

2 Methods

The study was approved by the Human Investigation Review Board University of Szeged (approval number 67/2020-SZTE). The trial was registered on ClinicalTrials.gov under NCT04360837. Both patients were deep sedated, intubated and ventilated. The ventilator was operated in pressure-controlled mode. The EIT measurement was performed with a Dräger PulmoVista 500 device (Dräger Medical, Lübeck, Germany). Patient A was monitored for 7 days, Patient B 12 days. Time difference EIT images were reconstructed using the Newton-Raphson algorithm. An averaged tidal image was obtained from the last 10 breathing cycles of each PEEP step.

The lung area of each tidal image was horizontally segmented to 8 layers with different plateau pressures as shown in Fig. 1a. The measured airway pressure was considered equal to the $P_{plateau}^1$ at the layer 1. The $P_{plateau}^n (n \leq 8)$ at layer n was set to be 2 cmH$_2$O larger than the plateau pressure at the previous layer. For each pixel of the tidal image, the pixel compliance was calculated as:

$$Compliance_{pixel} = \frac{\Delta Z}{P_{plateau}^n - PEEP} \qquad (1)$$

It is assumed that the regional lung reaches the best compliance when the corresponding pixel compliance is the largest, e.g. in Fig. 1b.
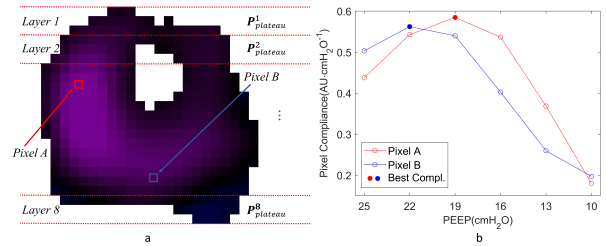
Figure 1: (a) An example of a lung area segmented to 8 layers with different plateau pressures, where pixel A and B are at different layers; (b) Respective pixel compliances of pixel A and B during a decremental PEEP trial, where the best pixel compliances are reached at different PEEP steps

In a decremental PEEP trial, the reduction of overdistention is observed with an increase of pixel compliance, while the collapse (derecruitment) is accompanied by a decrease of pixel compliance. The algorithm to estimate the cumulative collapse and overdistention ratio in a decremental PEEP trial is designed by Costa et al[3].

3 Conclusions

Patient A witnessed a steeper cumulative collapse ratio increase than Patient B during the decremental PEEP trial. The overdistention ratio at highest PEEP was found increasing over days in Patient A, while that of Patient B oscillating. The result suggests that Patient A is not as recruitable as Patient B. Patient A was a L-type patient, while Patient B was a H-type patient. It is also suggested a possible transition from a L-type to a H-type in Patient A.

4 Acknowledgements

References

[1] Gattinoni, Luciano and Chiumello, Davide and Caironi, Pietro and Busana, Mattia and Romitti, Federica and Brazzi, Luca and Camporota, Luigi *Intensive Care Medicine*, 46:1099–1102, 2020

[2] Zhao, Zhanqi and Kung, Wan-Hsuan and Chang, Hou-Tai and Hsu, Yeong-Long and Frerichs, Inéz *Critical Care*, 24, 2020

[3] Costa, Eduardo L. V. and Borges, João Batista and Melo, Alexandre and Suarez-Sipmann, Fernando and Toufen, Carlos and Bohm, Stephan H. and Amato, Marcelo B. P. *Intensive Care Medicine*, 35:1132–1137, 2009

Session 2: Algorithms I

A systematic analysis of an a priori D-Bar EIT algorithm using the GREIT figures of merit

Jöran Rixen[1], Steffen Leonhardt[1], Chuong Ngo[1]

[1]Medical Information Technology, Aachen Germany, `rixen@hia.rwth-aachen.de`

Abstract: We evaluated the effect of a-prioir information on an a-priori D-Bar algorithm for electrical impedance tomography (EIT) reconstructions with the help of the Graz consensus Reconstruction algorithm for electrical impedance tomography (GREIT) figures of merit. We analyzed different parameters like the truncation radius for the a-priori information.

1 Introduction

The D-Bar algorithm is a relatively new reconstruction algorithm. It was first numerically implemented by Siltanen et al. [1]. The D-Bar method has several benefits like robustness towards noise in the injected currents, robustness towards noise in the voltage measurements and robustness towards electrode displacement [2].

Since EIT belongs to the class of inverse problems, the D-Bar method has an integrated regularization scheme. This sacrifices spatial resolution for the robustness towards noise. However, when other measurement modalities are present the spatial resolution can be enhanced. We investigate the benefits of incorporating additional information in the D-Bar algorithm with the help of the GREIT figures of merit [3].

2 Methods

We analyzed a simplified version of the a-priori D-Bar algorithm proposed by Alsaker and Mueller [4] with the help of the GREIT figures of merit. The D-Bar algorithm is based on transforming the Lapalce equation into the Schrödinger equation. The D-Bar algorithm takes the Dirichlet to Neumann map as an input. From this, the scattering transformation - sometimes also called the non linear Fourier transformation - is calculated. The scattering transformation is mapping a given signal to non-linear waves with complex frequency like components. As opposed to the Fourier transformation, which maps a given signal to sinusoidal waves with frequency components in the real numbers. In order to incorporate a regularization strategy, values in the k-space of the scattering transformation with $|k| > R_1$ are set to 0, which can be regarded as some kind of low-pass filtering. With the help of the k-space the D-Bar equation is solved and the conductivity is obtained.

In order to incorporate additional information we use a simplified technique from Alsaker and Mueller. As opposed to their method we only augment the k-space by a-priori information, rather then altering the computation of the scattering transform. The a-priori information is transformed into the k-space. All values with $R_1 < |k| \leq R_2$ are added to the k-space of the scattering transform from the EIT data, while the other vlaues are left out. This concept is shown in figure 1.

In figure 2 the GREIT figures of merit Amplitude Response (AR), Position Error (PE), Resolution (RES), Shape Deformation (SD) and Ringing (RNG) are plotted for each

value of the outer truncation radius R_2.
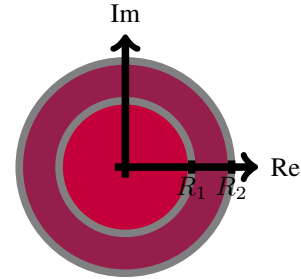
Figure 1: Visualization of the k-space, in red the EIT data is present, in bordeaux the a-priori data is stored. Every value outside of R_2 is 0.
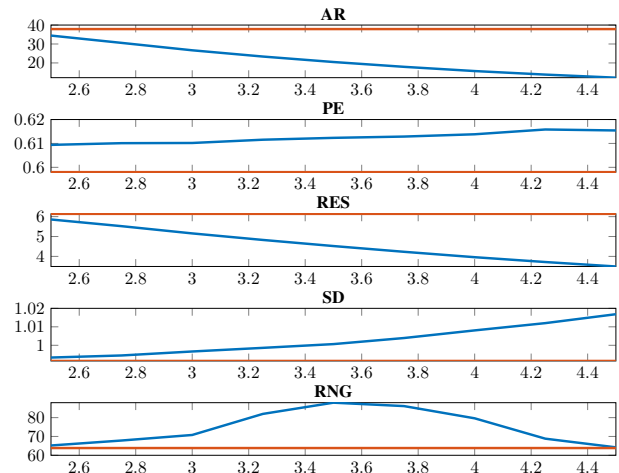
Figure 2: GREIT figures of merit for an increasing truncation radius R_2.

3 Conclusions

Augmenting EIT-measurements with other modalities through the D-Bar algorithm provides useful additional information, and tends to increase the spatial resolution of the reconstruction. However, depending on the type of a-priori information the truncation radius for the augmented data must be chosen with care. A too large radius may cause the to incorporate artefacts into the reconstruction.

References

[1] Samuli Siltanen and Jennifer Mueller and David Isaacson. Inverse Problems An implementation of the reconstruction algorithm of A Nachman for the 2D inverse conductivity problem *Inverse Problems*, 16:681–699, 2000

[2] Ethan K. Murphy and Jennifer L. Mueller. Effect of Domain Shape Modeling and Measurement Errors on the 2-D D-Bar Method for EIT *IEEE Transactions on Medical Imaging*, 28:1576–1584, 2009

[3] Andy Adler, John H. Arnold, Richard Bayford and others. GREIT: a unified approach to 2D linear EIT reconstruction of lung images *Physiological measurement*, 30:35–55, 2009

[4] Melody Alsaker, Jennifer L. Mueller. A D-Bar Algorithm with A Priori Information for 2-Dimensional Electrical Impedance Tomography *SIAM Journal on Imaging Sciences*, 9:1619–1654, 2016

Region of Interest Guided Stimulation Pattern Selection Strategy for Electrical Impedance Tomography

Hari Om Aggrawal and Alistair Boyle

KITE Medical, Ireland, {hari.aggrawal, alistair.boyle}@kitemedical.ie

Abstract: The proposed method identifies an optimal set from all possible combinations of stimulation patterns for a fixed number of electrodes. The reconstructions using the optimal set achieve better localization within the region of interest compared to the common stimulation patterns.

1 Introduction

In electrical impedance tomography, stimulation patterns highly influence the attainable spatial resolution and distinguishability in a reconstruction [3]. Typically, these patterns are decided based on personal experiences and simulations. In this paper, we propose a methodology to select stimulation patterns such that we obtain high quality reconstructions in our region of interest (ROI).

2 Method

The proposed method has three steps. Given N electrodes, the number of possible pair-drive stimulation configurations are $N(N-1)/2$. We quantify the importance of each pair-drive for reconstructing a point target x (one mesh-element) in the ROI by calculating the goodness score

$$GS_k = \|\Sigma_k \, V_k^\top x\|_2 \qquad (1)$$

where we use the SVD decomposition of the sensitivity matrix defined for the kth pair-drive, $i.e.$, $J_k = U_k \Sigma_k V_k^\top$. In (1), we measure how well the basis functions represent the point-target, weighted with the singular values.

Now, we build an optimal stimulation set starting with the highest scored pair-drive. We add high scoring pair-drives one by one in the set until the criteria holds:

$$\text{Rank}(\bar{J}) \le \lfloor s \, \text{Rank}(J) \rfloor \qquad (2)$$

where the sensitivity matrix $\bar{J}$ is built with pair-drives in the optimal set and J with all $N(N-1)/2$ pair-drives. At each step, we eliminate high scoring pair-drives if they do not increase the rank of $\bar{J}$. It is likely that high scoring pair-drive sensitivity matrices are linearly dependent to each other.

The tuning parameter $s \in (0, 1]$ enables us to choose only the most important pair-drives if a high frame rate is desired for data acquisition. For $s = 1$, the optimal $\bar{J}$ is similar to J in the sense of the number of linearly independent vectors in the sensitivity matrix. The value of s can also be adjusted by analyzing the singular values of J.

In the last step, we repeat the first two steps for a number of targets covering the entire ROI. The union of optimal sets, identified for each point-target, is the final optimal set that we use for reconstruction of an object in the ROI.

3 Experiments

We define an ellipsoid ROI of semi-axis $(0.2, 0.2, 0.5)$cm at origin $(0, 0.5, 0)$ inside a cylinder of radius 1cm and height 1.4cm. Total $N = 2 \times 16$ electrodes are placed at two planes $z = \pm0.3$cm. We take single-ended measurements with respect to a reference electrode for each stimulus pair. We apply current stimulus at all electrodes but the reference electrode. Hence, the total stimuli are $S = (N-1)(N-2)/2$.

We reconstruct a 2D slice at $z = 0$ of a spherical target with 10% contrast of radius 0.15cm placed at $y = 0.5$cm and multiple heights h; see Fig. 1 for reconstructions with full stimulus patterns, popular skip-4 square pattern, and three patterns obtained with the proposed approach.

Measurements are with noise of variance 10^{-8}. We calculate regularization parameters λ using the image signal to noise ratio (SNR) measure with SNR = 0.5 [1].

The reconstructions are highly localized near to the reconstruction plane with both full and the proposed stimuli compared to the skip-4 pattern; as also illustrated through the GREIT resolution measure (lower is better) [2]. But, with the target further away from the reconstruction plane, performance decreases with a reduced number of patterns.

h from center	0.0	0.2	0.4	0.6
full pattern, S = 465 λ = 0.0738				
resolution	0.366	0.371	0.375	0.392
skip-4 square, S = 30 λ = 0.0769				
resolution	0.525	0.505	0.479	0.491
s = 1.0, S = 140 λ = 0.0737				
resolution	0.40	0.397	0.402	0.435
s = 0.6, S = 81 λ = 0.0737				
resolution	0.424	0.397	0.399	0.417
s = 0.2, S = 29 λ = 0.0727				
resolution	0.488	0.428	0.434	0.455

Figure 1: Reconstructions with five stimulation patterns. Black circle represents the ground-truth target position.

4 Conclusion

We proposed a method to obtain stimulation patterns targeting a specific ROI. Our results shows that highly localized reconstructions are possible through optimally selected stimulation patterns. Future work involves improving the method by removing redundancy in the optimal set.

References

[1] F Braun $et.al.$, $IEEE\ Biomedical\ Engg.$, 64(10):2321-2330, 2017,
[2] A. Adler $et.al.$, $Physiol.\ Meas.$, 30(6):S35-S55 2009,
[3] A. Adler $et.al.$, $Physiol.\ Meas.$, 32(7):731-744 2011.

Generating forward models from CT images for ventilation monitoring in ARDS patients

Symon Stowe[1], Zhanqi Zhao[2], Emily Huxter[1], Huaiwu He[3], Yun Long[3], Andy Adler[1]

[1]Carleton University, Ottawa, Canada, symonstowe@sce.carleton.ca
[2]Institute of Technical Medicine, Furtwangen University, Furtwangen, Germany
[3]Department of Critical Care Medicine, Peking Union Medical College, Chinese Academy of Medical Sciences, Beijing, China

Abstract: A tool was designed to automatically segment and manually correct boundaries of CT images from ADRS patients to generate custom forward models. These models were used to reconstruct EIT images and estimate global inhomogeneity index of the lungs.

1 Introduction

Acute respiratory distress syndrome (ARDS) is a form of respiratory failure caused by widespread swelling and accompanied by an accumulation of fluid in the lungs. We present a method to use diagnostic CT images to improve EIT model accuracy. ADRS patients may have occlusions from fluid and collapse making it challenging to identify the lung regions correctly. We created a tool to segment and correct the boundaries of the lungs in ARDS patients and compared the resulting model against a generic model using the Global Inhomogeneity (GI) index [1].

2 Methods & Results

Data from 4 ARDS patients with CT and EIT were used to develop a segmentation and correction tool to identify the lungs and boundary of the body. Segmentation was done using the 4th intercostal space, with 10 adjacent CT slices to form an enclosed chest cavity. The lungs and exterior boundary were identified by increasing the contrast and identifying an appropriate threshold. Each segmentation was downsampled to 20 points that could be edited by the user in Matlab. The mesh was generated using `ng_mk_extruded_model` [2] in EIDORS 3.10 [3]. Images were reconstructed using GREIT [4]. The GI index was calculated using the method presented by Zhao et al. [1] using the lung regions from the forward model. A ventilated lung estimate was made using the segmentation as $\frac{A_{\text{ventilated lung}}}{A_{\text{total lung}}}$.
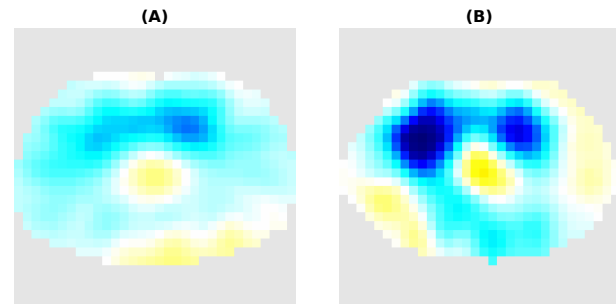
Figure 1: Single breath using: A) generic model B) custom model

Results in fig. 1 show a reconstructed image with more separable lungs in the enhanced model, and a mean GI index for each breath in the 1 minute recording that follows trend of the ventilated lung percentage in table 1.

Table 1: Ventilated lung estimate vs. GI index scores.

Subject	Ventilated lung (%)	GI (basic model)	GI (custom model)
1	99.9	0.353±0.004	0.690±0.005
2	85.5	0.640±0.022	0.771±0.020
3	79.6	0.695±0.007	0.857±0.009
4	27.0	0.614±0.011	1.81±0.053

References

[1] Z Zhao *Intensive Care Med.*, 35:11, 2009
[2] B Grychtol et al. *IEEE Trans Med Imag* 31:9, 2012
[3] A Adler *Conf 19th EIT*, p.63, London, UK, Jun 2019
[4] A Adler et al. *Physiol Meas*,30:S35-S55, 2009
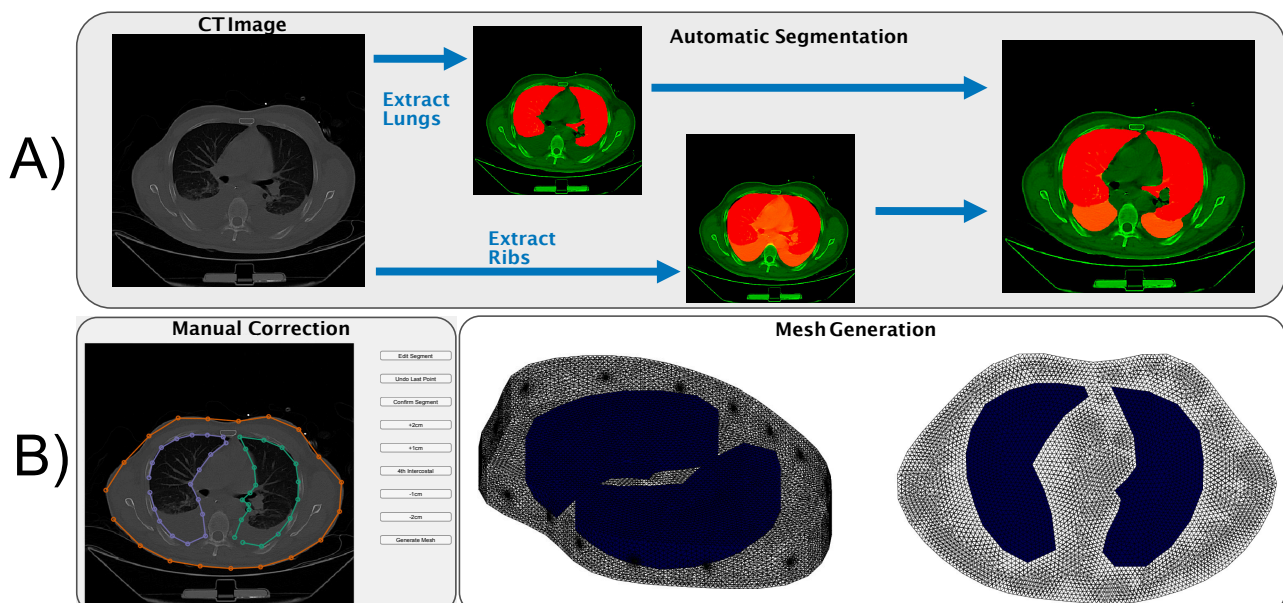
Figure 2: An overview of the segmentation and editing process showing: A) A sample raw CT which was thresholded, scaled and adjusted over several adjacent slices to identify the lung regions and an enclosed rib area, and the resulting lung estimate; and B) A screen capture of the manual mesh correction process and 2 views of the generated mesh.

An equilibrium finite element method for the forward problem of electrical impedance tomography with the shunt model

Erfang Ma

Department of Applied Mathematics, School of Science, Xi'an Jiaotong-Liverpool University, `erfang.ma@xjtlu.edu.cn`

Abstract: A new numerical method for the forward problem of EIT is presented. It finds the distribution of current density by minimizing the heat consumed, and reconstructs the potential distribution with the current density. Simulation results show that the method is more accurate than the traditional finite element method for some models of EIT.

1 Introduction

The forward problem of EIT is often solved with the finite element method in terms of the potential distribution over the region [1]. Instead of potential, this paper presents and tests an equilibrium finite element method [2] in terms of current density for the forward problem.

2 Methods

The new method is based on the principle that the current density j in equilibrium minimizes the total Joule heat consumed [3]. Given a mesh over the EIT region Ω, the total heat consumed is a quadratic functional of j, i.e.

$$\sum_m \frac{1}{\sigma_m} \int_{T_m} j \cdot j \, \mathrm{d}x = J^T K(\boldsymbol{\sigma}) J \tag{1}$$

Here σ_m is the constant conductivity in the m-th element T_m. The J is a column vector of Cartesian components of j in every element of the mesh. The $K(\boldsymbol{\sigma})$ is sparse and depends only on the conductivity distribution $\boldsymbol{\sigma}$ and the mesh.

The current density J is determined with minimizing the total heat (1) subject to the constraints

$$\mathrm{div}\, j = 0 \quad \text{in } \Omega, \tag{2a}$$

$$j \cdot n = 0 \quad \text{on } \partial\Omega / \cup_{l=1}^{L} e_l, \tag{2b}$$

$$\int_{e_l} j \cdot n \, \mathrm{d}s = I_l, \quad l = 1, 2, ..., L. \tag{2c}$$

Here I_l is the current through the l-th electrode e_l, and n is unit out normal on the boundary. The constraints (2) can be encapsulated as

$$AJ = F. \tag{3}$$

where both A and F are sparse and depend only on the mesh.

Overall, we find J by solving the KKT system

$$\begin{pmatrix} 2K & A^T \\ A & 0 \end{pmatrix} \begin{pmatrix} -J \\ \lambda \end{pmatrix} = \begin{pmatrix} 0 \\ -F \end{pmatrix} \tag{4}$$

with λ the Lagrange multiplers.

Given the current density, the potential distribution is found by solving a system of linear equations that relates the potential difference between neighboring nodes in the mesh, to the electric field.
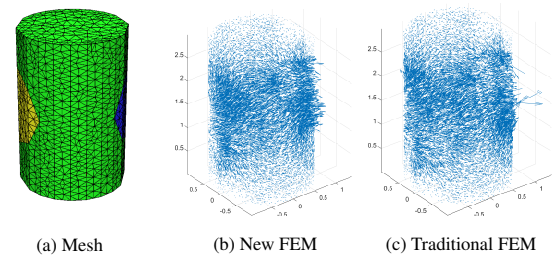
3 Results

Figure 1 (a) shows a mesh for a 2D EIT with 16 electrodes of shunt models and uniform conductivity distribution. Figure 1 (b) compares the error in approximating the voltages at all the electrodes, obtained with the traditional FEM with linear and quadratic elements, and the new method. It indicates the results of the new method is the most accurate.

(a) Mesh   (a) errors of approximations
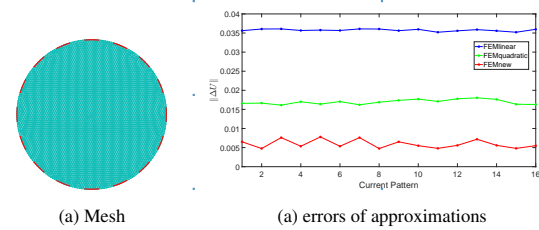
Figure 1: Simulations results on a 2D EIT

Figure 2(a) shows a mesh for a 3D EIT with two electrodes of shunt model. Conductivity is non-uniformly distributed with low value at the core of the region and around the two electrodes. Figure 2(b,c) compares the current density obtained by the traditional FEM with linear elements and the new FEM. As seen, the current density obtained with the new method changes more smoothly around the edge of electrodes.

(a) Mesh   (b) New FEM   (c) Traditional FEM
Figure 2: Simulations results on a 3D EIT

4 Conclusions

The new FEM seems to outperform the traditional FEM for the forward problem of EIT with the shunt model. Experimental tests and theoretical study of this method could be done in the future.

References

[1] DS Holder *Electrical Impedance Tomography* IOP Publishing: Bristol, 2005

[2] J.P. Almeida and E.A. Maunder *Equilibrium Finite Element Formulations* Wiley: 2017

[3] E Ma *Inverse Prob. & Imaging*, 14(2):385–398, 2020

Modular Expandable Programming Architecture for Interactive Web-Based EIT Data Exploration

Hervé Gagnon[1], Jeff Dawson[1], Andy Adler[1]

[1]Carleton University, Ottawa, Canada, `adler@sce.carleton.ca`

Abstract: We designed a modular and expandable programming architecture for EIT data analysis. It is coded in Python, HTML, CSS and JavaScript to favor code reuse and contribution while minimizing use of third-party solutions. Modules can be interconnected to provide custom interactive web-based solutions for EIT data exploration.

1 Introduction

Several software packages have been developed for EIT data analysis and research. EIDORS allows reconstruction of images and waveforms from simulated or real EIT data [1]. Ibex is a freely available software for EIT image analysis [2]. Most EIT equipment manufacturers also provide their own software for EIT data processing and exploration. However, no software tools exist to provide interactive web-based data processing and exploration for EIT while providing an open environment that can be fully customized to a user needs. We developed such an architecture using an approach similar to the modular expandable multi-threaded architecture described in [3].

2 Methods

The software is designed in Python, Javascript, HTML and CSS building on the strength of each language and minimizing requirements for third-party libraries. Each module provides an arbitrary number of inputs, outputs and timers that are defined in the Python language. The architecture is event-driven: whenever new data is received at an input or a timer expires, processing occurs and results are transmitted to the relevant outputs. Python is also used to connect the output from one module to the input of another module through channels than can be buffered or not. The HTML, CSS and Javascript languages are used to provide the web-based graphical interface for the python modules. The graphical user interface is therefore accessible from any web browser.

3 Conclusion

Several modules have been realized to read, process and display EIT data as shown in Figure 1. EIT images can be displayed and analyzed at real-time speed. The user can select different types of data processing, browse through the acquired data and explore the results of frame-by-frame, breath-by-breath or time-interval EIT data analysis.

References

[1] A Adler and WRB Lionheart *Physiol. Meas.*, 27:S25:S42, 2006.
[2] PL Róka, AD Waldmann, SH Bohm, C Karagiannidi, and F Ender *EIT2015*, p.59, Neuchâtel, Switzerland, Jun 2015.
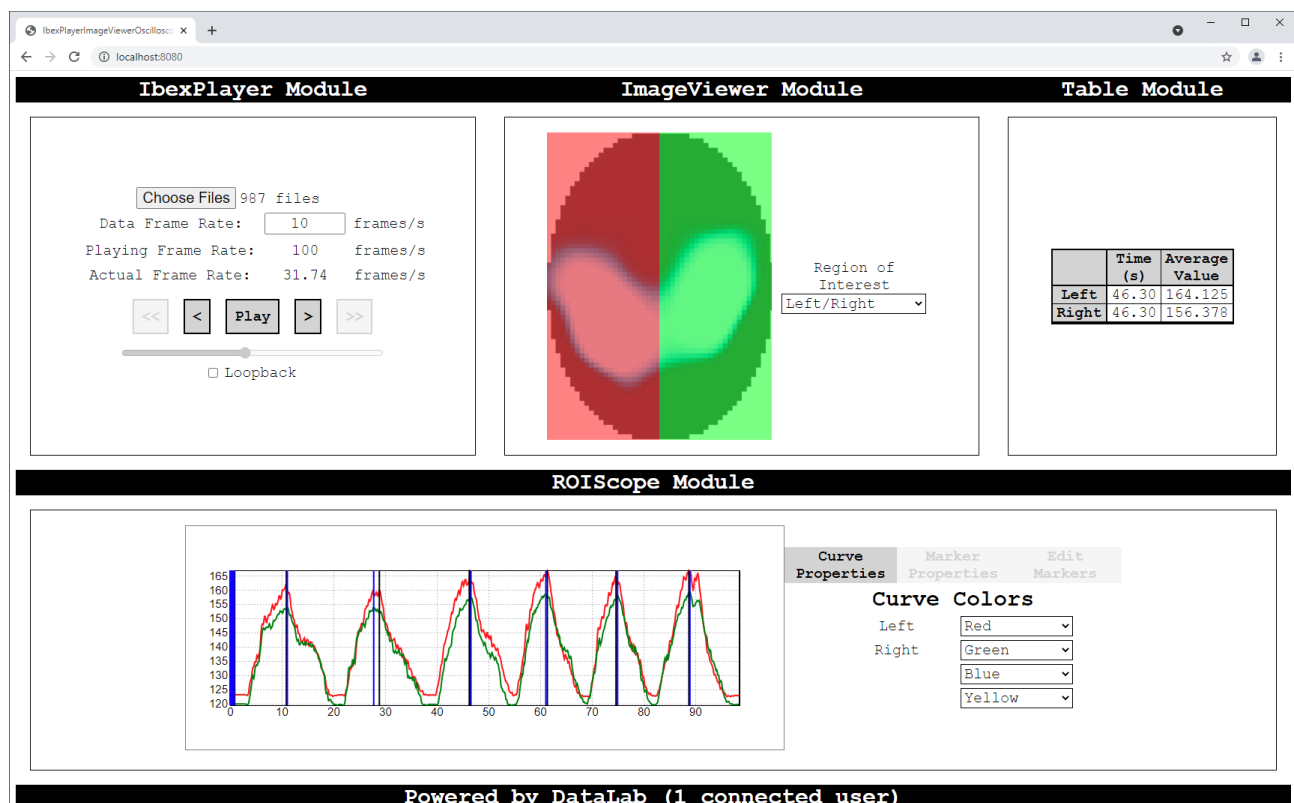[3] H Gagnon, *Ph.D. Thesis*, Polytechnique Montreal, Canada 2003.

Figure 1: Example of an application for EIT data exploration designed with the described programming architecture.

EIT parameter configuration selection framework

Diego Corona-Lopez,

School of Electrical and Electronic Engineering, The University of Manchester, diego.coronalopez@manchester.ac.uk

Abstract: Selection of EIT parameters such as electrode separation, skip, and stimulation protocols are key in determining the quality of reconstructions, especially in 3D. In the present work we propose a framework to assess and select a balance set of parameters using an statistical approach and considering the final goal of the application.

1 Introduction

EIT can be seen as an optimisation problem, where there are multiple parameters to fine tune. Typically, EIT configuration aspects are selected heuristically or still use legacy methodologies e.g. acquisition protocols. Most EIT systems use the pair-driven method thus, any combination of pair-driven measurements is referred as a stimulation and measurement pattern (S/M pattern for short). [1] have highlighted the importance of the adequate selection of S/M patterns, and have proposed steering away from the traditional adjacent pattern to 'skip' patterns that offer higher sensitivities (specially at centre of the vessel). Furthermore, when dealing with 3D reconstructions the benefit of skip not only become apparent but essential to improve the vertical resolution of the system. This present work proposes a framework to help design an optimised EIT system through the evaluation of different parameters.

2 Methods

Since it is common for EIT to have lower sensitivity values near the geometry's centre, we are interested in achieving the maximum sensitivity possible in this region through the careful selection of both the electrode vertical separation and S/M patterns. Therefore, Simulations of a FEM cylindrical geometry were conducted based on a real pipe of dimensions 18×16 cm with two electrode rings comprised of sixteen 2×2 cm electrodes. We employ a fine mesh with 1.9×10^5 elements with a higher mesh density near the electrodes . The analysis starts with the rings in close proximity being positioned at the middle of the vessel (to be specific at 7 and 9 cm respectively), then we separate the rings one centimetre at a time calculating the sensitivity for each new model using both planar and square S/M patterns with multiple skip configurations. For each stimulation the normalised sensitivity across the geometry computing each FEM element contribution using its element or volume size (Ni):

$$S = \frac{\sqrt{\sum J^2}}{N_i} \qquad (1)$$

where J represents the Jacobian. Fig.1 shows the sensitivity at the middle of the geometry for both planar and square protocols across skips going from S1-S8 and M1-M8 patterns at vertical position 4. An SVD analysis was conducted to obtain the condition number for all S/M patterns and electrode positions. Opposite patterns (e.g. S8/M8) are not evaluated due to their 'mirror' effect when conducting reconstructions.
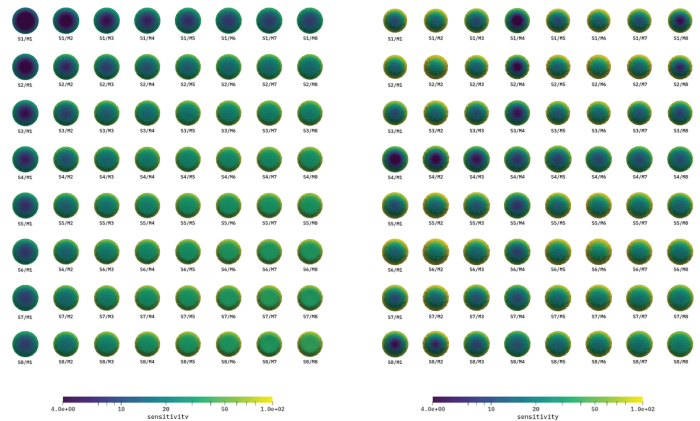
Figure 1: Sensitivity maps for planar (left) and square (right) protocols for different skip combinations.

Fig. 2 shows the violin plot corresponding to the distribution of the condition number for both planar and square patterns across the seven rings' positions tested. From Fig. 2 we observe that it is possible to obtain lower condition numbers when selecting a square pattern. Furthermore, it appears that square patterns offer what we can consider as a logarithmic normal distribution through all positions, being more bottom skewed when reaching the last two positions. On the other hand, the condition number pertaining to planar arrangements increases with the position, performing poorly on the last position where the distribution is top skewed.
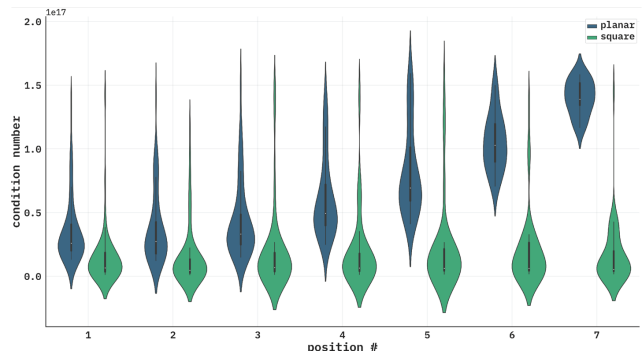
Figure 2: Violin plot corresponding to the condition numbers obtained from all possible S/M combinations in both planar and square methods, tested in seven vertical electrode rings' positions.

3 Conclusions

The framework presented is to evaluate multiple EIT parameters based on the geometry of the final application. Evaluating the presented parameters should serve as a guide for the vertical positioning of the electrodes in a real geometry, and the selection of an S/M patterns based on a balance between the achieved sensitivity and its corresponding condition number.

References

[1] Adler A, Arnold JH, et al. *Physiol meas. 30(6):S35-55*, Epub, Jun 2009

Using esophageal electrodes for increased sensitivity to cardiac-frequency impedance changes

Symon Stowe[1], Nathalie Samson[2], Charlène Nadeau[2], Christophe Morin[2], Jean-Paul Praud[2], Étienne Fortin-Pellerin[2], Andy Adler[1]

[1]Carleton University, Ottawa, Canada, `symonstowe@sce.carleton.ca`
[2]Université de Sherbrooke, Sherbrooke, Canada

Abstract: We use EIT measurements made on an 4 electrodes placed in the esophagus to improve the sensitivity of the impedance image to central changes. Results across 3 subjects in an ovine model show increased sensitivity to cardiac-frequency impedance changes.

1 Introduction

Electrical Impedance Tomography (EIT) is most sensitive to changes in impedance near the electrodes and typically has limited sensitivity in the center-most regions of the model. 3D configurations of external electrodes help to give a more uniform sensitivity distribution and limit the effect of off-plane impedance changes compared to a single ring of electrodes [1].

EIT has been used as a tool to continuously monitor mechanical ventilation in critical care patients. but has limited sensitivity near the heart and central regions of the lungs. For many of these patients nasogastric tubes may already be in place and could be used in conjunction with internal electrodes to significantly increase internal EIT sensitivity without additional invasiveness. Previous work has shown that 4 internal electrodes can greatly improve sensitivity near to the internal probe [2], but can be sensitive to motion. EIT has been proposed for use as a blood pressure monitoring tool using pulse wave velocity [3], but external configurations have limited sensitivity to changes in the descending aorta. Internal electrodes present the opportunity to obtain a significantly higher sensitivity and with motion correction may be used to give a more accurate estimate of arterial pressure. This abstract presents a method of using internal electrodes while correcting for motion of the internal probe to yield high internal sensitivity.

2 Methods

The forward model was constructed using EIDORS version 3.10 [4] using `mk_library_model` [5] the internal electrode was added as an extra structure. This model was also used to identify the heart and lung regions. The sensitivity of the lamb model was calculated from the Jacobian using the method from [2]. Sensitivity profiles using 32 electrodes with and without 4 internal electrodes are shown in fig. 1.

Data were collected in 3 ewes during ventilation under general anesthetic using the SenTec EIT Pioneer Set. 30 second recordings were made during regular ventilation with a volume of 400 ±50 ml, frequency of 0.2 ±0.05 Hz, and peep of 6. Recordings were repeated for several ventilation scenarios including: high volume (+100 ml), low volume (-100 ml), high frequency (+0.17 Hz), low frequency (0.07 Hz), high peep (10) and low peep (4).

All breaths in each 30 second segment were ensemble averaged to give one representative breath for each scenario.
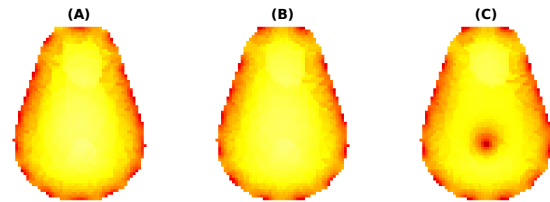
Figure 1: Sensitivity distribution averaged across 10 evenly spaced layers between the electrode planes in the lamb model for: A) 32 external electrodes B) 28 external electrodes c) 28 external electrodes and 4 internal electrodes

Images of one averaged breath per recording were reconstructed using the 3D GREIT algorithm [1] which minimizes the effect of electrode motion on the resulting image. Results were compared for both external only and internal electrode configurations using the same recording. To obtain results with only external electrodes all injections and measurements using internal electrodes were removed prior to reconstruction. Measurements on injecting electrodes were always removed. Images from one subject during regular ventilation are shown below in fig. 2. With internal electrodes, impedance changes at the cardiac frequency had an amplitude of 6.4% ±0.8% of the ventilation frequency and without internal electrodes the amplitude of the cardiac frequency was 0.8% ±0.2% of the ventilation frequency.
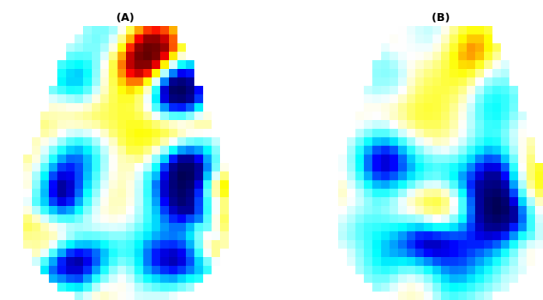
Figure 2: A single breath imaged with: A) no current injections or measurements on internal electrodes b) internal electrodes

3 Conclusions

The use of an internal probe yeilded higher sensitivity near the descending aorta. Reconstructions using the GREIT algorithm with internal electrodes on an esophageal probe were able to give increased sensitivity to cardiac-frequency impedance changes and may allow for better measures of blood pressure and pulse wave velocity.

References

[1] B Grychtol et al. *Physiol Meas* 37:785, 2016
[2] S Stowe and A Adler *IEEE EMBC*, Montreal, CAN, Jul 2019
[3] J Solà et al. *Med Biol Eng Comput* 49:409415, 2011
[4] A Adler *Conf 19th EIT*, p.63, London, UK, Jun 2019
[5] B Grychtol et al. *IEEE Trans Med Imag* 31:9, 2012

Session 3: Brain & Nerve

Feasibility of EIT in the Brain with an Extremely Compact Intracortical Array

Adam Fitchett[1] adam.fitchett.16@ucl.ac.uk, David S. Holder[1] and Kirill Aristovich[1]

[1]Department of Medical Physics & Biomedical Engineering, University College London

Abstract: This modelling study demonstrated the feasibility of intracortical EIT with a highly compact depth array. EIT could image circuit activity with a higher spatial resolution than LFP but lower than single-unit recording.

1   Introduction

Electrical impedance tomography (EIT) is a technique that aims to image neural activity at the circuit level while overcoming many of the shortfalls of alternative techniques (such as low spatial or temporal resolution, expense, lack of portability, sensitivity to dipole orientation and absence of a unique inverse solution) [1][2][3].

However, intracortical depth probes able to avoid excessive cortical damage (such as neural lace [4]) have extremely small electrodes. This is problematic for EIT, which requires low contact impedance to achieve a suitable signal to noise ratio [5].

This study used computational modelling to investigate two main questions: (1) Is intracortical EIT feasible with highly compact depth probes? (2) How does EIT's range and resolution compare to LFP and single unit spike recording?
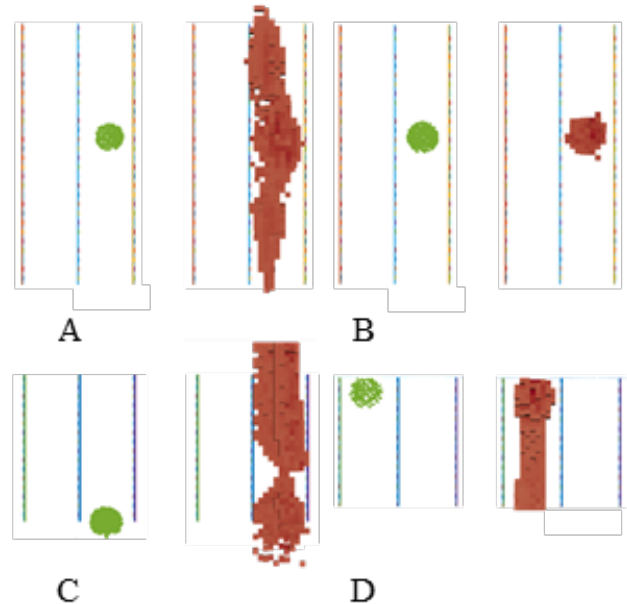
2   Methods

EIT in the cortex was simulated with the parallel EIT solver (PEITS), using a 2 million element mesh created in COMSOL Multiphysics®. The mesh contained a model of a highly compact intracortical array. This array, inspired by neural lace [4], had nine shanks in a 3x3 grid, each with 32 14*24 μm rectangular electrodes on one side and one 1596*20 μm electrode on the other side. Shank spacing was 300 μm.

Injection current amplitude was 80 μA. Neural activity was simulated as a spherical perturbation of 1% conductivity change relative to background. Activity was reconstructed on a hexahedral mesh by inverting the Jacobian matrix.

Volume error was calculated as the difference between the volume of the original and reconstructed perturbation as a percentage of the original volume; position error was calculated as the Euclidean distance between the original and reconstructed centre of mass as a percentage of the perturbation's original diameter.

Table 1: Error in position (E pos) and volume (E vol) of various reconstructions. Dist. = distance from nearest shank.

Depth	Radius	Dist.	E (pos)	E (vol)
75 μm	75 μm	75 μm	498%	3900%
75 μm	85 μm	65 μm	315%	410%
75 μm	85 μm	55 μm	327%	1600%
800 μm	85 μm	65 μm	32%	111%
1600 μm	85 μm	65 μm	114%	8600%

Figure 1: Original (left) and reconstructed (right) perturbations. (A) Radius 75 μm, distance 65 μm, depth 800 μm. (B) R 85 μm, dist 65 μm, dep 800 μm. (C) R 85 μm, dist 65 μm, dep 1600 μm. (D) R 85 μm, dist 55 μm, dep 75 μm.

3   Conclusions

EIT of circuit activity could be conducted successfully in the cortex with a highly compact depth array. The smallest perturbation that could be reconstructed successfully had a radius of 85 μm and was 65 μm away from the nearest shank. 85 μm corresponds to approximately 14 pyramidal neurones and provides a higher spatial resolution than LFP (approx. 200 μm) but lower than single-unit spike recording (as used by Musk & Neuralink (2019) [4]).

In general, perturbations near the centre of the array were reconstructed better than those placed deeper or higher up. For instance, for a perturbation of radius 85 μm at a distance of 65 μm from the nearest shank and a depth of 800 μm below the surface, volume error was 111 %; by contrast, when the depth was 75 μm, volume error was 410%, and when the depth was 1600 μm, it was 8600%.

Since it is probable that the electrode array geometry used in this study was sub-optimal, our future work will aim to optimise the geometry of depth arrays for EIT.

References

[1] Aristovich, K. Y. *et al.. Neuroimage* **124**, 204–213 (2016).
[2] Witkowska-Wrobel, A., Aristovich, K., Faulkner, M., Avery, J. & Holder, D. *Neuroimage* **173**, 311–321 (2018).
[3] Aristovich, K. *et al.. J. Neural Eng.* **15**, 56025 (2018).
[4] Elon Musk & Neuralink. *bioRxiv*. (2019).
[5] Gilad, O. & Holder, D. S. *Neuroimage* **47**, 514–522 (2009).

EIT-Based Stroke Detection: Skip Impact on Classification Accuracy

Jared Culpepper[1], Hannah Lee[1], Barry McDermott[3], Adam Santorelli[2] and Emily Porter[1]

[1]Electrical Engineering, University of Texas at Austin, Emily.porter@austin.utexas.edu
[2]Biomedical Engineering, University of Texas at Austin
[3]Translational Medical Device Lab, National University of Ireland Galway

Abstract: EIT has shown promise for stroke detection and stroke-type differentiation. In this work, we simulate a realistic head model using EIDORS. We examine the classification accuracy of differentiating lesion type (between bleed and clot) using support vector machine classifiers for data from different skips.

1 Introduction

It is vital to detect a stroke as quickly as possible to enable the correct treatment and support optimal outcomes. Electrical impedance tomography (EIT) has the potential to provide a low-cost, accessible tool for rapid stroke detection and stroke-type differentiation.

2 Methods

In this work, the head model used to represent a normal human head consists of three layers: a solid brain in the middle, a uniform shell of cerebrospinal fluid (CSF) of thickness 4.2 mm (3.5 mm in the scaled model) around the brain, and an outer layer of skull and skin aggregate. The model volumes are reduced by 41% for ease in computation. This model is discussed in detail in [1], and only minor changes have been made to the geometry here. The conductivity of CSF used in this work is 1.79 S/m, which is a realistic value at body temperature [2]. A summary of the conductivity and sizes of each tissue included in the models are provided in Table 1.

For the stroke cases, a sphere representing a lesion is added to the brain volume. Four different lesion locations (at the front, left, right, and back of the head) and two different lesion sizes (10 mL and 30 mL) are simulated. For each of these head models, the voltage measurements are simulated at a signal-to-noise ratio (SNR) of 40 dB since it is feasible to achieve this SNR in realistic settings. In total, 2000 observations for each of the two stroke types is recorded. Each observation contains 208 features (voltage measurements from each injection-measurement electrode pair).

Table 1: Description of Simulated Head Models.

Tissue Type	Conductivity (S/m)	Model Volume (mL)	Realistic Volume (mL)
Skull/skin aggregate	0.1	1945	3297
CSF	1.79	142	241
Brain aggregate	0.3	683	1158
Bleed	0.7	5.9, 17.8	10, 30
Ischemic	0.08	5.9, 17.8	10, 30

A nested testing methodology is used classify the data using a support vector machine (SVM) classifier with a radial-basis function (RBF) kernel, as seen in [3]. The data set (in total, 4000 observations of 208 features) is separated into ten separate folds, each with a unique training data set and testing data set that is made up of 90% and 10% of the original data set, respectively. The training data set is used to optimise the SVM classifier hyper-parameters, using a Bayesian optimization procedure. The final trained SVM classifier is created with these optimised hyper-parameters and the excluded test data set is used to obtain the performance metrics for the final classifier. This procedure is then repeated for all ten of the unique training-testing data pairs. This nested testing methodology provides a more generalised and robust indication of classifier performance.

Additionally, as in [3], we use principal component analysis (PCA) to reduce the number of features for the classifier from 208 to 10. PCA is performed on only the training data, with the transformative coefficients stored and then applied to the test-set data. This ensures that there is no knowledge of the test-set data when performing PCA, avoiding any data contamination between training and testing. This nested testing methodology is applied to all the data collected for the various injection pair skip patterns. In Fig. 1, a box and whisker plot summarizes the classifier performance at each skip number. The trend is as expected, wherein the accuracy is approximately the same for skips that involve the same number of skipped electrodes.
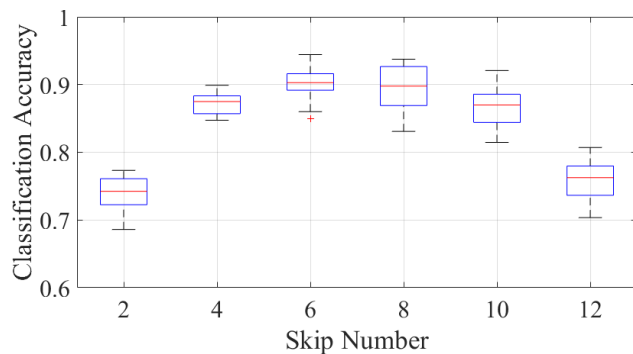
Figure 1. Bleed vs. clot classification accuracy for each skip.

3 Conclusions

The ability to classify bleed versus clot is skip-dependent. By optimizing skip selection, the overall classification accuracy may be improved. Additionally, future work could consider combined classification using multiple skips to further enhance the classification accuracy.

References

[1] H. Lee, J. Culpepper, A. Farshkaran, B. McDermott, E. Porter, *43rd Ann. Intl. Conf. IEEE Eng. Med. Biol. Soc.*, 2021, [submitted].

[2] S. B. Baumann, D. R. Wozny, S. K. Kelly, F. M. Meno, *IEEE Trans. Biomed. Eng.*, 44(3):220-223, 1997.

[3] B. McDermott, E. Dunne, M. O'Halloran, E. Porter, A. Santorelli. (2019). Brain and Human Body Modeling, Computational Human Modeling at EMBC 2018, S. Makarov, M. Horner, G. Noetscher (Eds.), pp. 211-244, Cham, Switzerland: Springer, 2019.

Bioimpedance-based Focal and Global Secondary Injury Differentiation in a Pig Model

Alicia Everitt[1], Brandon Root[3], Daniel Calnan[3], David Bauer[3] and Ryan. J. Halter[1,2]

[1]Thayer School of Engineering, Dartmouth College, Hanover, NH, USA, alicia.c.everitt.th@dartmouth.edu
[2]Geisel School of Medicine, Dartmouth College, Hanover, NH, USA
[3]Dartmouth Hitchcock Medical Centre, Lebanon, NH, USA

Abstract: This paper summarizes a large animal study on monitoring and detecting secondary traumatic brain injury (TBI) using bioimpedance. The data collected in this study validates the ability of impedance to 1) detect intracranial volume changes as low as 0.39 mL and 2) differentiate focal from global intracranial injury events. The measurements of resistivity changes during TBI provide in-vivo benchmarks for use in future tomographic applications.

1 Introduction

Traumatic brain injury (TBI) is a leading cause of disability in the United States and causes more deaths in men 35 and younger than all other diseases combined[1]. TBI contributes to nearly a third of injury-related deaths, is the fourth leading cause of the death in the U.S.[2,3], and costs the U.S. ~$60 billion annually[4]. The clinical standard for monitoring severe TBI is through intracranial pressure (ICP) sensing; however, significant limitations in the ICP response have motivated investigation into more multi-modal monitoring approaches[1].

Identifying the underlying etiology of elevated ICP is essential for patient care of severe TBI, yet is currently limited to serial CT scans. The presence of a focal injury (e.g. large vessel occlusion) or global injury (e.g. edema) may be managed differently (e.g. immediate surgical intervention vs hyperosmolar therapy), yet both present as elevated ICP. Differentiating 1) the etiology of the injury (e.g. ischemic or haemorrhagic), 2) if it is focal or global and 3) localization intracranially would overcome current limitations and provide critical improved management. This study explored the use of a bioimpedance monitoring (BIM) system for assessing secondary injury in a large animal model.

2 Methods

Nine pigs were instrumented with three intracranial catheters positioned using AxiEM Stealth navigation: 1) a compliance catheter in the left lateral ventricle, 2) a mass effect (ME) and hematoma simulating fogarty catheter in the left parietal lobe and 3) a coupled ICP monitor and intracranial electrode in the right frontal lobe. Scalp Ag/AgCl tab electrodes were placed circumferentially around the cranium of the pig in eight pairs (16 total) (fig. 1). The ME balloon was inflated in steps of 100uL every five minutes up to 1.2mL to induce a focal ME. Following deflation, autologous blood was injected in steps of 200uL up to 1.2mL to model focal hematoma. Mannitol was then administered to model global diffusion, followed by euthanasia to capture global brain death. CT scans were acquired at each intracranial state every five minutes (fig 1). Bioimpedance data were collected continuously using our custom BIM system and analog hardware. Tetrapolar bioimpedance measurements were sequentially recorded using two current drive electrodes and two voltage pickup electrodes at 2.3mApp and 50 kHz.

Figure 1: Instrumentation, surgical planning and example injuries in the pig model.

3 Conclusions

The BIM successfully differentiated ischemic from haemorrhagic models (p=0.0019), detected a minimum volume of 0.39 mL and found significant unequal variance between focal and global injuries (p<0.001). Future work can build upon this study to explore additional tomography and intracranial imaging approaches. This research presents strong initial results of the potential for impedance to be used to monitor patients with severe TBI.

4 Acknowledgements

References

[1] Le Roux, P., TR in TBI, 2016
[2] Faul, M., CDC NCIPC, 2010
[3] "Accidents or unintentional injuries", CDC, 2017
[4] Finkelstein, E., Oxford Press, 2006

Combined hdEEG and EIT for Stroke Applications

Ethan K. Murphy[1], Alicia Everitt[1], Yinchen Song[2,3], Erik J. Kobylarz[1,2,3], Ryan. J. Halter[1,2]

[1]Thayer School of Engineering, Dartmouth College, Hanover, NH, USA, ethan.k.murphy_@dartmouth.edu
[2]Geisel School of Medicine, Dartmouth College, Hanover, NH, USA
[3]Dartmouth Hitchcock Medical Center, Lebanon, NH, USA

Abstract: This paper summarizes phantom work that was an important step in beginning a combined high-density Electroencephalogram (hdEEG) and Electrical Impedance Tomography (EIT) pilot study on stroke patients. Difference reconstructions yielded an average error of 2.2 cm on 15 tests of insulative and conductivity inclusions.

1 Introduction

There are nearly 800,000 people in the United States that have a stroke each year, with approximately 140,000 deaths[1]. The most vital step in treatment is fast diagnosis of ischemic or haemorrhagic stroke. Additionally, there are needs for prolonged monitoring after an acute stroke and in predicting outcomes. The technique under study is a system that combines hdEEG and EIT to potentially improve speed of diagnosis, yield an automatic monitoring system, and/or provide an improved metric for predicting patient outcomes. The novel combination of hdEEG and EIT technologies is exciting because these complementary technologies are: 1) inexpensive, portable, and use nonionizing radiation, 2) sensitive to stroke-related changes (e.g. quantitative EEG is sensitive to ischemic changes and there are significant differences between the electrical properties of blood, normal tissue, and ischemic tissue[2]), and 3) measure fundamentally different entities (brain function vs. material properties).

2 Methods

A custom plug was developed to allow for 140 channels of the 256 electrodes from an hdEEG (Magstim EGI) (see Fig. 1A) cap to be used for EIT recording. Our 20-channel EIT system is manually multi-plexed to the full 140 electrodes in sets of 20. The hdEEG/EIT is thus setup for sequential hdEEG and EIT recordings. The phantom experiments involved 1) making a gelatine head with a 'brain' cavity (Fig. 1), 2) placing the hdEEG cap on the head, inverting and filling the cavity with matching saline (to the gelatine), and 3) electrode-magnetically (EM) tracking inclusions placed within the cavity. EM-tracking was done using an Aurora V2 EM system (Northern Digital Inc., Ontario, Canada). The gelatine head was made from 10% gelatine to saline mixture (saline ~0.03 S/m) that was placed within a head mould. The head mould was constructed via a mannequin head and Smooth-On silicone. The 'brain' cavity was formed by a Styrofoam form that was held fixed via a wooden stage during the gel setting. The inclusions were plastic or metal spheres of 3.4 and 9.9 cm diameters. The inclusions were affixed to a tracked pointer with approximate positional error of ~1 mm. A total of 15 tests were performed that varied the inclusion position from left to right, top (dorsal) to bottom (ventral), and anterior to posterior. A data set included impedance data from the 140 electrodes, and the qualitative and EM-tracked location of the inclusion.

Only EIT difference reconstructions are considered. The 3D finite element method (FEM) mesh used was from [3]. The 256 hdEEG locations were based on nominal electrode locations from Brainstorm (https://neuroimage.usc.edu/brainstorm/), and were subsequently best-fit to the FEM mesh. The inclusion locations were registered to the phantom by EM-tracking the position of 15 electrode locations. Two views of a difference reconstruction (Fig. 2) show good correspondence (~1.8 cm error) between the true inclusion (red sphere) and thresholded point (yellow dots).
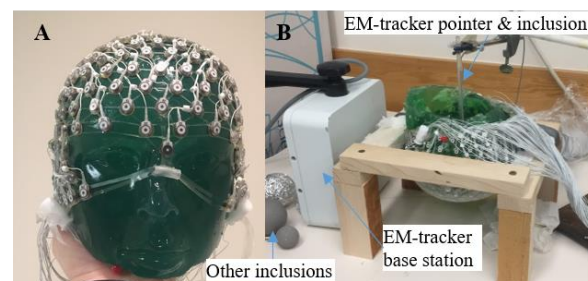
Figure 1: A. Gelatine head with 256 hdEEG cap and B. the head and cap inverted, filled with saline, and an inclusion placed within the cavity. Note the EM-tracking system and inclusions.
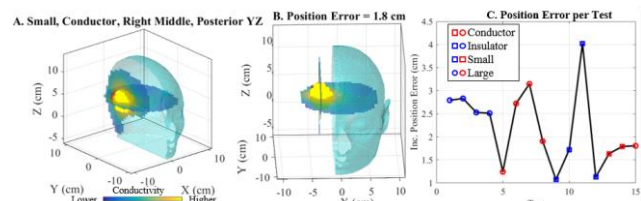
Figure 2: Two views of an EIT difference reconstruction with position error of 1.8 cm. The red sphere represents the true location and yellow dots are thresholded values. C. shows the position error for all 15 tests.

3 Conclusions

EIT difference imaging successfully localized both insulative and conductive inclusions within a realistic phantom utilizing the 256 electrode hdEEG cap. Analysis of accuracy versus depth/distance to electrodes is ongoing.

4 Acknowledgements

References

[1] Yang, Q. et al, 2000 – 2015. Mmwr 66, 1–7, 2017.
[2] Dowrick, T., et al. Physiol. Meas. 36, 1273–1282, 2015.
[3] Avery, J. et al. Nat. Sci. Data, 5, 1–10, 2018.

# Feasibility of Imaging Fast Neural Activity Using Magnetic Detection Electrical Impedance Tomography

Kai Mason `kai.mason@ucl.ac.uk`[1], Kirill Aristovich[1], David Holder[1]

[1]Department of Medical Physics and Biomedical Engineering, University College London

Abstract: The feasibility of imaging fast neural activity in the human brain using magnetic detection electrical impedance tomography (MD-EIT) with scalp electrodes and optically pumped magnetometers (OPMs) has been evaluated with computational modelling using an anatomically realistic finite element mesh (FEM) of a human head.

1 Introduction

Imaging fast electrical activity in the brain with EIT and scalp electrodes requires impractically long averaging times because the relatively resistive skull causes low SNR. We propose this could be achieved by in humans by injection of a constant current or voltage through scalp electrodes and measurement of the resultant magnetic field change during cerebral activity as the skull does not attenuate magnetic fields. We undertook a computer simulation study to determine: (1) Does constant current or voltage injection produce a greater SNR? (2) Will MD-EIT give a larger SNR than EIT with scalp electrodes?
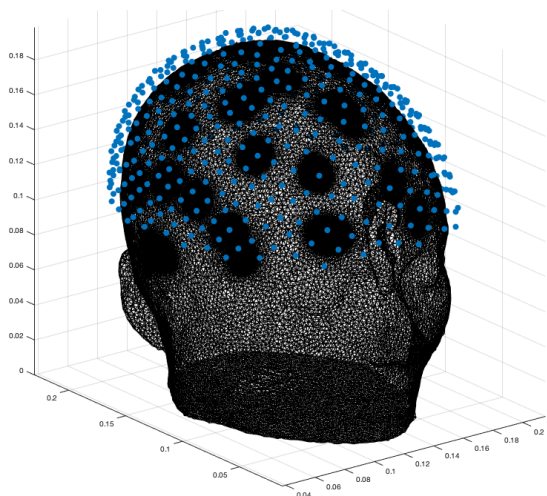
Figure 1: Human head mesh with OPMs displayed as blue spheres

2 Methods

MD-EIT simulations were carried out on an anatomically realistic 3.5 million element FEM of a human head with 32 scalp electrodes and 500 magnetic field sensors (Figure 1). 1mA at 1.5kHz was applied and neural activity was modelled as a spherical 1% local impedance decrease with a 2cm diameter. Four perturbations were considered with centres 1,3,5 and 7cm inwards from the skull. The SNR was taken from the peak magnetic or electric field changes arising with constant current/voltage injection (Table 1). The magnetic noise floor was taken as the OPM sensitivity of $\sim$10fTHz$^{-1/2}$ = 245fT for a 600Hz bandwidth [1] since MEG noise at $\sim$1.5kHz is $\sim$1fT [2]. The electric noise floor was 3.87µV [3].

3 Results

MD-EIT with constant voltage injection gives the greatest SNR of 5.5 which is 6% and 150% larger than the greatest SNR for constant current injection MD-EIT or EIT respectively. A larger SNR occurred for the most superficial perturbation with MD-EIT, but with EIT for deeper perturbations (Table 1).

4 Discussion

In theory, constant voltage would be expected to produce a greater magnetic field change as the total current density, to which the magnetic field is proportional, would change. In practice, field changes with constant current were only slightly smaller. The difference is not large enough to warrant use of a constant voltage system since most EIT systems use constant current injection [4]. It is predicted that MD-EIT will produce a 150% increase in SNR over EIT for the most superficial perturbation considered. However, OPM sensitivity is predicted to have a fundamental limit that is 1000 times greater than that of current commercial OPMS [1, 5], indicating that there is scope for large increases in SNR for MD-EIT. Future work includes imaging of impedance changes in saline-filled tanks, formulation of an efficient method for the calculation of the Jacobian for MD-EIT and impedance measurements of EPs in rats.

References

[1] Quspin. QZFM Gen-2 – QuSpin.

[2] T. Fedele, H. J. Scheer, M. Burghoff, G. Curio, and R. Körber. *Physiological Measurement*, 36(2):357–368, 2015.

[3] Kirill Y. Aristovich, Brett C. Packham, Hwan Koo, Gustavo Sato dos Santos, Andy McEvoy, and David S. Holder. *NeuroImage*, 124:204–213, 2016.

[4] David S Holder. *Electrical impedance tomography: methods, history and applications*. CRC Press, 2004.

[5] I. K. Kominis, T. W. Kornack, J. C. Allred, and M. V. Romalis. *Nature*, 422(6932):596–599, 2003.

Table 1: Optimal SNRs after 225 averages for MD-EIT with constant current/voltage injection and EIT with constant current injection.

Perturbation Centre Distance From Skull (cm)	Magnetic Constant Current SNR	Magnetic Constant Voltage SNR	Electric Constant Current SNR
7	0.44	0.45	1.3
5	0.5	0.53	1.5
3	1.4	1.4	2.1
1	5.1	5.5	2.2

The impact of 2D assumptions in 3D brain imaging

James Avery[1] and Kirill Aristovich[2]

[1]The Hamlyn Centre, Imperial College London, UK, james.avery@imperial.ac.uk
[2]Medical Physics and Biomedical Engineering, University College London, UK

Abstract: Reduction of the computation required for imaging offers many benefits in real time brain monitoring applications. However, the assumption of consistent tissue properties required to utilise 2D imaging do not hold due to tissue heterogeneity. This results in significantly increased imaging artefacts and shape errors in reconstructions.

1 Introduction

The complex morphology and heterogeneity and of the brain and component tissues pose particular challenges in neurophysiological simulations, necessitating 3D volume conductor models with a large number of elements [1]. Typically, sensors are equally distributed across the entire surface of the head in standard EEG placements, to capture activity throughout the brain. Thus, a full 3D forward and inverse model are required for accurate reconstructions.

In some applications where the location of the pathology is known *a priori* electrodes can be placed in a plane, level with the target location [2]. In this configuration either 2D or "2.5D" (3D forward, 2D inverse) simplifications are used to reduce computation. However, the impact and limitations of these assumptions, and the resultant imaging artefacts are not well understood in the literature. In this work the errors arising from these approximations are investigated in numerical simulations of time difference imaging of haemorrhagic stroke.
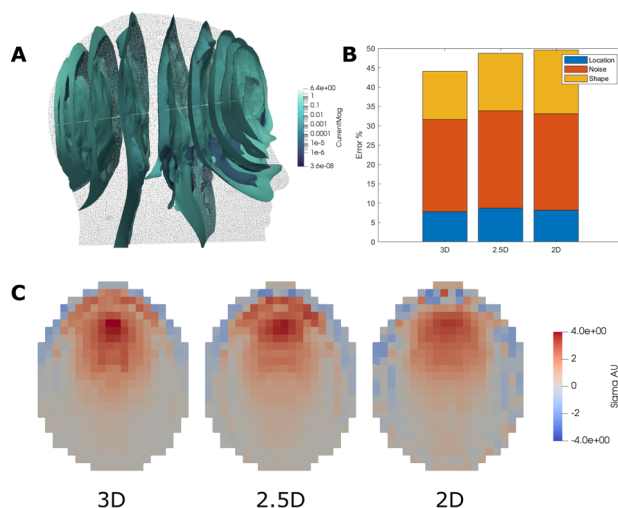
Figure 1: A) Current magnitude and isopotential surfaces for single anterior-posterior current injection, electrode plane shown in white B) Averaged image quality metrics for all nine perturbation locations C) Comparison of reconstructed haemorrhage in anterior location with 3D, 2.5D and 2D imaging.

2 Methods

First " ground truth" 3D meshes of ~4 million elements were created using EIT-MESHER (https://github.com/EIT-team/Mesher) based on joint CT and MRI segmentations with seven tissue layers (Grey and White matter, CSF, Skull, Diploë/Sagital Sinus, Air and Scalp [3]. A ring of 16 10mm electrodes were placed on the circumference of the head in a plane offset from the inion-nasion line by 10mm. Haemorrhages of 7.5 mm radius (1.7 mL) were simulated in anterior, posterior, and lateral positions in the electrode plane and on planes offset by 10 and 20 mm. 2D meshes of ~ 40k elements were created by slicing through the tetrahedral meshes at the electrode plane. Elements of the 3D Jacobian within 5 mm of the plane were combined to create the coarse-to-fine mapping for 2.5D imaging. In all cases the forward models were calculated using EIDORS, and images were reconstructed in hexahedral subdomains, using cross-validated Zeroth Order Tikhonov regularisation [4]. The voltage differences simulated in the 3D meshes were used to reconstruct images in each of the three cases: Full 3D, 2.5D and Full 2D. Image quantification was used to assess the impact of these simplifications.

3 Results

The current density in the 2D cases broadly represent those in the 3D meshes, as previously observed in the literature [5]. However, the complexity of the isopotential surfaces could not be approximated as planar, even within the thickness of the electrodes. The greatest discrepancy between the 3D and 2D current fields were at boundaries of high conductivity contrasts, in particular scalp/skull and the ventricles. This resulted in greater artefactual changes in these locations in the reconstructed images. Whilst the haemorrhages could still be located using the 2.5D and 2D methods, the reconstructed perturbations showed increased spread and were consistently drawn into the centre of brain. This is reflected in the image quantification results, where there was no significant increase in centre of mass error using either simplification, but noise and shape errors did significantly increase in both cases ($P<0.05$).

4 Conclusions

2D approximations in brain imaging can result in significantly increased imaging artefacts, even in idealised simulations, and their use should be carefully considered depending upon the application. Future work should focus on investigating the effects of noise, electrode movement and more realistic bleed shapes.

5 Acknowledgments

References

[1] C. M. Michel and D. Brunet, *Front. Neurol.*, vol. 10, 2019.
[2] M. Dai *et al.*, *PLoS One*, 8(1) e55020, 2013.
[3] M. Jehl, K. Aristovich, M. Faulkner, and D. Holder, *Physiol. Meas.*, 37:879–892, 2016
[4] K. Y. Aristovich, G. S. dos Santos, B. C. Packham, and D. S. Holder, *Physiol. Meas.*, 35:1095–109, 2014
[5] H. Li *et al.*, *Physiol. Meas.*, 38:1776–1790, 2017

Electromagnetic field distribution imaging during deep brain stimulation (DBS) using MRI: a biological tissue phantom study

Munish Chauhan[1], Saurav Z K Sajib[1], Sulagna Sahu[1], Willard S Kasoff[2] and Rosalind J Sadleir[1]

[1] School of Biological and Health Systems Engineering, Arizona State University, Rosalind.Sadleir@asu.edu
[2]Department of Surgery, University of Arizona

Abstract: Computational methods have been widely used to estimate field distributions produced by conventional or recently introduced directional DBS electrodes. However, until now there has been no experimental method that can measure these field parameters. In this work, we demonstrate that it is possible to quantify electromagnetic field distribution during DBS therapy using magnetic resonance electrical impedance tomography (MREIT).

1 Introduction

Magnetic resonance current density imaging (MRCDI) [1] and MREIT [2] are two emerging techniques that can produce low-frequency current density and conductivity distributions, respectively using MR phase data induced due to external current injection.

MRCDI has already been used to demonstrate current pathways during deep brain stimulation (DBS) therapy [3,4]. However, it is not possible to find the corresponding electric field distributions due to the lack of a stable conductivity reconstruction method. Recently, Song et al. [5] developed an iterative single-current algorithm that can stably reconstruct the 'apparent' conductivity distribution from data obtained using a single current. The aim of this study is to demonstrate the capability of the new algorithm to characterize electromagnetic field distributions produced by DBS electrodes.

2 Methods

A head-shaped phantom formed of agarose-gel was used in this study4. A DBS electrode (Abbott Infinity 6172, Abbott, Abbott Park, IL, USA) was inserted near the phantom centre. A 50 x 50 mm^2 carbon return electrode (HUREV Co Ltd, South Korea) was also attached at the occipital (Oz) location. We placed a piece of chicken muscle between DBS lead and Oz electrode to form a conductivity contrast. An MR safe electrical stimulator (neuroConn, Germany) was used to deliver a 1.0 mA current between the DBS (omni- directional (DBS-1) or unidirectional (DBS-2B)) electrode contact and the return Oz electrode.

All MR data were measured using a 32-channel RF coil in a 3.0T Phillips scanner (Phillips, Ingenia, Netherlands). Current induced magnetic flux density (B_z) data was measured at three axial slice positions using the Phillips mFFE pulse sequence. Imaging parameters were matrix size = 128×128, FOV = 224x224 mm^2, TR/TE = 50/7 ms, Echoes =10, Echo spacing = 3 ms, and NSA = 24.

We first used the stray-field-corrected B_z data to reconstruct the current density distribution, $\mathbf{J}^{(P,R)}$ within the local region, R using the regional projected current density algorithm8. From the $\mathbf{J}^{(P,R)}$, and the known conductivity, (σ_b), at the tissue boundary ∂R, the first-update of the internal conductivity distribution, σ^1 was reconstructed as [5]:

$$\begin{cases} \nabla_{xy}^2 \ln \sigma^1 = \frac{1}{\mu_0} \nabla_{xy} \cdot \left(-\frac{J_y^{P,R}}{\left(J_x^{P,R}\right)^2 + \left(J_y^{P,R}\right)^2} \nabla_{xy}^2 B_z, \frac{J_x^{P,R}}{\left(J_x^{P,R}\right)^2 + \left(J_y^{P,R}\right)^2} \nabla_{xy}^2 B_z \right) & \text{in } \mathcal{R} \\ \ln \sigma^1 = \ln \sigma_b & \text{on } \partial \mathcal{R} \end{cases} \quad (1)$$

where μ_0 denotes the permeability in free space. We set σ_b=0.75 S/m. The corresponding electric field distribution was then found using Ohm's law

$$\mathbf{E} = \mathbf{J}^{P,\mathcal{R}}/\sigma \quad (2)$$

2.1 Figures and tables

Figs. 1a (i) and (iv) show the reconstructed $|\mathbf{J}^{(P,R)}|$ distribution due to the 1.0 mA current injected using the DBS-1-Oz and DBS-2B-Oz electrode configurations, respectively. Reconstructed σ^1 distributions measured using the DBS-1-Oz and DBS-2B-Oz configurations are displayed in figs. 1b (ii) and (v), respectively. The corresponding electric field magnitudes found using Eq. 2 are shown in fig. 1c (iii) and (vi).
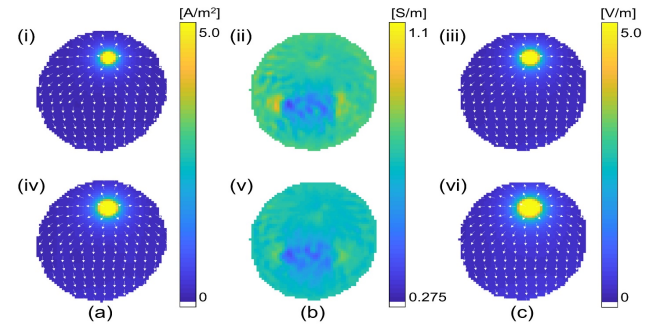
Figure 1: Reconstructed regional projected current density (a), conductivity (b) and electric field map (c). Upper panel (i), (ii), and (iii) display the results from DBS-1-Oz and bottom panel (iv), (v), and (vi) shows the results from DBS-2B-Oz electrode configuration. The overlaid normalized arrow in (a) and (c) shows the direction of current and electric field.

3 Discussion and Conclusions

We have demonstrated that it is possible to characterize electromagnetic properties and fields deep within the brain using DBS electrode illumination using a biological tissue phantom. It was found that electromagnetic fields between a single energized directional electrode and a ground electrode on the phantom surface were larger than those found for a conventional DBS lead.

Acknowledgements

References

[1] Scott G C et al. *IEEE Trans. Med. Imaging.* 10(3): 362-7, 1991
[2] Seo J K and Woo E J *SIAM Rev.* 53(1):40-68, 2011
[3] Sajib S Z K et al. *AIP Adv.* 7(1):015004, 2017
[4] Chauhan M et al. *Proc. Intl. Soc. Mag. Reson. Med.* 28,0740, 2021
[5] Song Y et al. *Phys. Med. Biol.* 65(22):225016, 2020

Stroke Diagnosis Using Multi-Frequency Symmetry Difference EIT (MFSD-EIT) with SVM Classification

Barry McDermott[1], Adnan Elahi[1], Adam Santorelli[4], Martin O Halloran[1], James Avery[2] and Emily Porter[3]

[1]Translational Medical Device Lab, National University of Ireland Galway, barryjames.mcdermott@nuigalway.ie
[2]The Hamlyn Centre, Imperial College London, London, UK
[3]The Department of Electrical and Computer Engineering at The University of Texas at Austin, TX, USA
[4]The Department of Biomedical Engineering at The University of Texas at Austin, TX, USA

Abstract: MFSD-EIT can detect unilateral perturbations in symmetric scenes such as bleed or clot lesions in stroke patients. Differences in conductivity spectra can then be used for identification of lesion type. We assess the potential of using MFSD-EIT data as an input to SVM classification algorithms for stroke diagnosis.

1 Introduction

Important medical conditions, such as stroke, feature static lesions that can be difficult to image using EIT [1]. Identification of the cause of stroke as either bleed or clot is a crucial part of the diagnostic pathway. The novel algorithm presented in [2] compares EIT frames from two mirror image orientations across the sagittal plane of the head. Deviations in symmetry across this plane due to the presence of a lesion were detectable using this algorithm. The differing conductivity spectra of bleed and clot, and in particular the change in contrast between these lesions and brain over the 5 Hz – 100 Hz band [3] can then be used to identify the lesion type. The Global Left Hand Side (LHS) & Right Hand Side (RHS) Mean Intensity (GMI) metric can be computed from a symmetry difference image and quantifies the deviation in symmetry on each side of the plane at that frequency point. GMI values collected at different frequency points can hence be used to identify lesions. Further, these collected GMI values can be used as input features to machine learning classification algorithms such as Support Vector Machines (SVM) and used to classify lesion type in stroke patients. This idea is explored in this work where the binary classification problem of bleed versus clot is considered using data recorded from simulated and human stroke patients.

2 Methods

Four-layer finite element method (FEM) models based on neuroimaging studies of 18 patients provided in the UCLH stroke EIT dataset [4] were used to create 1,458 anatomies (varying in scaling of each of the four layers) each with 8 unique bleed or clot lesions. EIT frames were generated, and GMI metrics collected for each of the 11,664 bleed and 11,664 clot cases. These GMI values were used as inputs into a radial basis function kernel SVM classifier with 10-fold nested cross-validation performed to robustly train and test the classifier. This procedure was also performed using frames recorded from human stroke patients provided in [4], with 180 bleed and 252 clot cases generated by reconstruction of the frames onto each of the n = 18 FEM models. The performance of the classifier is reported in Fig.

1 as the mean ± standard deviation of sensitivity, specificity, accuracy, positive predictive value (PPV), and negative predictive value (NPV), across the 10-iterations. A mean accuracy of 85% is achieved for the human data, with clots strongly detected (mean PPV 85% and sensitivity 90%). Bleeds are slightly less well detected (mean NPV 86% and specificity). For simulated data, all metrics results in a mean above 99%.
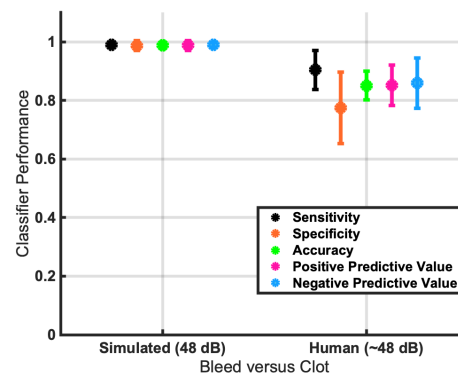
Figure 1: Classifier performance for bleed (negative class) versus clot (positive class) for simulated and human data sets.

3 Conclusions

This paper applied the MFSD-EIT algorithm to both human and simulated stroke data. The important GMI metric summarises differences in symmetry across the sagittal plane and can be used as an input to classification algorithms. An average accuracy of 85% is achieved when MFSD-EIT with SVM classification is used to identify and differentiate bleed from clot in human data. Hence, the approach gives promising results especially considering the small number of patients.

4 Acknowledgements

References

[1] A Adler, A Boyle, *IEEE Transactions on Biomedical Engineering* 64(11):2494-2504,2017
[2] B McDermott, M O Halloran, E Porter, *Physiological Measurement* 39(4):044007,2018
[3] A Romsauerova, A McEwan, L Horesh, *Physiological Measurement* 27(5):S147-S161,2006
[4] N Goren, J Avery, T Dowrick *et al.*, *Scientific Data* 5:180112, 20

Session 4: Thorax II

Feasibility of EIT for Hemodynamic Monitoring: Animal Study

Geuk Young Jang,[1] Ryoung Eun Ko,[2] Chi Ryang Chung,[2] Jin Young Lee,[2] Tong In Oh,[1]
Gee Young Suh,[2] Yongmin Kim,[3] and Eung Je Woo[1]

[1]Department of Biomedical Engineering, College of Medicine, Kyung Hee University, Seoul, Korea, tioh@khu.ac.kr
[2]Department of Critical Care Medicine, Samsung Medical Center, Sungkyunkwan University School of Medicine, Seoul, Korea
[3]Department of Creative IT Engineering, POSTECH, Pohang, Korea

Abstract: An EIT device was used as a hemodynamic monitor during repeated mini-fluid challenges on six pigs. A lately-developed source separation algorithm was applied to measure beat-to-beat stroke volume (SV). The results suggested that the EIT device could be used in personalized fluid management to determine fluid responsiveness.

1 Introduction

Stroke volume and cardiac output are important parameters in hemodynamic monitoring, especially for fluid management decisions in treating hemodynamically unstable patients. Although chest EIT data provide information about both lung ventilation and cardiac blood flow, EIT has been clinically used in most cases for regional lung ventilation imaging during mechanical ventilation. Clinical application of EIT in hemodynamic monitoring is rare since cardiogenic components of the EIT data are much weaker than those of lung ventilation.

2 Methods

Six pigs (weights of 29 to 31 kg) were premedicated with intramuscular injection of ketamine (20 mg/kg) and xylazine (2.5 mg/kg). Each animal was mechanically ventilated in the volume mode (Hamilton-G5, Hamilton Medical, Switzerland). Anesthesia was maintained by inhalation of 2% isoflurane mixed with 25% oxygen. For each animal, 500 or 600 ml of blood was manually removed to simulate a hypovolemic state. Ten 100-ml injections of a crystalloid fluid (Plasma Solution-A Injection, CJ Healthcare, Korea) were made manually using a syringe. The duration of each fluid injection was about 1 min, followed by a 2-min rest, making the interval between two consecutive fluid injections to be 3 min.

For beat-to-beat SV measurements, we used a 16-channel EIT device (AirTom-R, BiLab, Korea) with 100 frames/s temporal resolution. Applying a lately-developed source separation method [1], the cardiac volume signal (CVS) was extracted from reconstructed blood flow and ventilation images, respectively. An invasive hemodynamic monitor (EV1000, Edwards Lifesciences, U.S.) was also used to simultaneously measure SV through a catheter inserted into the femoral artery. While the EV1000 provided SV data every 20 seconds, the EIT device measured SV in every cardiac cycle.

3 Results and Conclusions

Fig. 1 shows an example of reconstructed blood flow images from which the CVS was extracted. Fig. 2 shows an example of acquired SV data using the EIT device (SV_{EIT}) and the EV1000 in the PCA mode (SV_{PCA}). The EIT device measured SV regardless of blood pressure,

while SV using the EV1000 was unavailable at low blood pressure. The EIT device not only measured SV reliably in animals under different intravascular volume states but also easily computed a percentage change in SV in response to each fluid injection to be able to determine fluid responsiveness.

The relative difference in the acquired 343 pairs of SV data during the mini-fluid challenge using the EIT device and the EV1000 was ±3.6 ml or 11%, which was within a clinically acceptable range [2]. The results from all 6 animals are available in [3]. This new SV measurement method using EIT could be used in passive leg raising (PLR) and end-expiratory occlusion (EEO) tests as well. Future clinical studies are needed to validate the efficacy of the EIT device as an accurate and reliable tool for fluid management and hemodynamic monitoring in general.
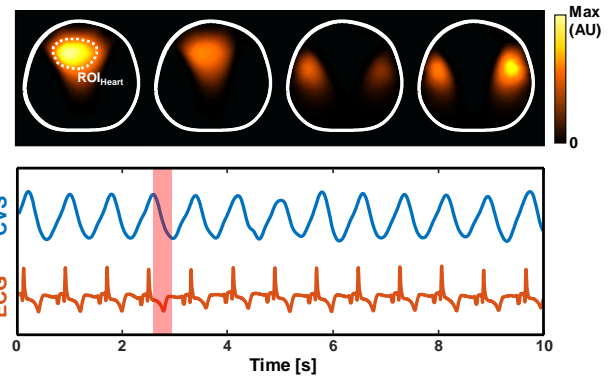
Figure 1: Reconstructed blood flow images and extracted CVS. The simultaneously-measured ECG indicates that the CVS decays during ventricular ejection. SV was obtained as the valley-to-peak value of the CVS.
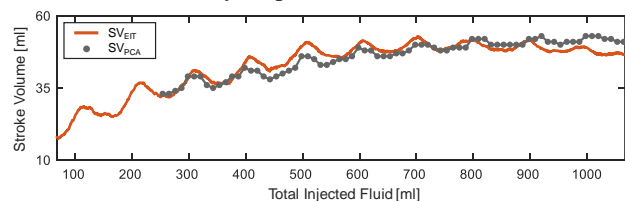
Figure 2: Measured SV data during ten 100-ml mini-fluid challenges using the EIT device (SV_{EIT}) and the EV1000 in the PCA mode (SV_{PCA}).

4 Acknowledgements

References

[1] GY Jang, *et al.*, *Sci Rep*, 10:11242, 2020
[2] A Joosten, *et al.*, *Br J Anaesth*, 118:298–310, 2017
[3] RE Ko, *et al.*, *Shock*, in press, 2021

A New Method for Simultaneous EIT/ECG Data Acquisition*

Ahmed Abdelwahab, Omid Rajabi Shishvan, Gary J. Saulnier

Electrical and Computer Engineering Department, University at Albany - State University of New York, Albany, NY, USA
aabdelwahab@albany.edu

Abstract: A new method for simultaneous EIT/ECG signals acquisition is proposed. In this method, an integrate & dump filter followed by a 2nd order low-pass filter separates the ECG signals from the EIT signals. The preliminary experimental results showed a good reception of a model ECG signal combined with an active EIT signal.

1 Introduction

Collecting ECG waveforms during EIT measurments is useful for providing additional clinical information as well as aligning EIT images with their location in the cardiac cycle. In earlier work on wearable sensors [1], ECG data were obtained by filtering the measured voltage with a 1st order high-pass filter at 0.05 Hz followed by 2nd order low-pass filter at 150 Hz.

In this work, we propose a different approach for simultaneous EIT/ECG data collection when using the adaptive current source described in [2], though the approach has wider applicability. The current source in [2] was designed, implemented, and tested for obtaining high-quality EIT images by compensating for all the current loss through any shunt impedance to the ground, i.e., delivering the desired current to the load. The proposed approach uses an integrate & dump filter designed to pass the low-frequency ECG signal and reject high-frequency EIT. The approach has low processing cost and makes it possible to simultaneously collect ECG data from all electrodes in a multi-source EIT system.

2 ECG Filter

Although the large frequency difference between the EIT and ECG signals should make the separation easy, several factors affect the filter implementation. The high sampling rate of 1.2 MHz used in [2] compared to the desired bandwidth of 150 Hz for the ECG signal requires the use of high precision coefficients for a digital LPF filter in a fixed-point format. Since the target EIT system is multi-frequency, using EIT excitations from 30 kHz to 1 MHz, downsampling is complicated by the associated aliasing of the EIT signals. Another critical factor is the large magnitude difference between the EIT and ECG signals. The system described in [2] designed to allow a maximum swing of $1V_{pp}$ for the measured EIT voltage, which is three orders of magnitude higher than the ECG signal. So high attenuation is needed to allow a high ECG/EIT signal-to-interference ratio.

The approach to recovering the ECG signal takes advantage of the EIT signal design. As in most EIT systems, the approach in [2] samples the electrode voltages at a high rate and implements a matched filter operating over an integral number of cycles of the EIT excitation signal to perform the voltage measurements. In the test system, the matched filters utilize 1024 samples and excitation frequencies are chosen such that 1024 samples represents an integral number of cycles. A consequence of this approach is that integrating (summing) the EIT signal over 1024 samples pro-

duces zero, i.e. an integrate and dump filter utilizing 1024 samples completely rejects the EIT signal for all excitation frequencies used in the system.

Following the medical standards for the ECG bandwidth, a 2nd order LPF with a cutoff frequency at 150Hz was used as a final stage of filtering the received ECG signal [3]. The lower cutoff frequency is determined by the analog design of the Howland source and passive components values in [2].

3 Experiments & Results

Figure 1: Generated ECG sample
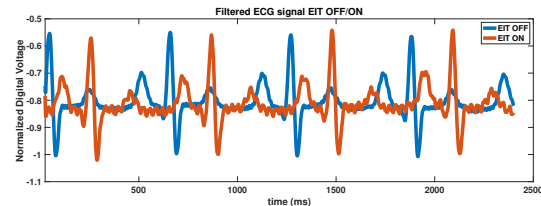
Figure 2: Received ECG Signal

Experimental results were obtained to validate the proposed approach. The lab-generated ECG signal sample is shown in fig.1 and has a repetition rate of 1.5 Hz. A resistor network is used to apply a $1\,\mathrm{mV}_{p-p}$ ECG signal to a 1 kΩ resistive load that can also be driven with an EIT current of 0.2mA and 93.75kHz excitation frequency. The results in fig.2 show the reconstructed ECG signal from the first 2400 measurements taken at a roughly 1 kHz rate both with and without the EIT signal present. It is important to clarify that the time delay shown between the two signals is not a result of the addition of the EIT signal. The time offset results from running both experiments independently where the first sample can be any point on the input ECG signal. The results are very promising, showing a good reconstructed ECG signal with a relatively small amount of degradation with the addition of the EIT signal.

References

[1] M. Rapin and F. Braun and A. Adler and J. Wacker and I. Frerichs and B. Vogt and O. Chételat *IEEE Trans. Biomed. Eng.*, 66:810-820, 2019

[2] Gary J Saulnier and Ahmed Abdelwahab and Omid Rajabi Shishvan *Physiol Meas*, 41:064002, 2020

[3] International Standard :*Medical Electrical Equipment-part 2-25* IEC 60601-2-25, 2nd ed., 2011

Detection of Motion Artifacts for Robust Cardiopulmonary Monitoring using EIT

Thi Hang Dang,[1] Kyounghun Lee,[1] Geuk Young Jang,[1] and Eung Je Woo[1]

[1]Department of Biomedical Engineering, College of Medicine, Kyung Hee University, Seoul, Korea

Abstract: Electrical impedance tomography (EIT) has been reported as an effective method for simultaneous, non-invasive monitoring the tidal volume (TV) and stroke volume (SV). For patients who received no sedation such as during haemodialysis, motion artifacts (MAs) appear commonly during prolonged TV and SV monitoring. These MAs disrupt respiratory volume signal (RVS) and cardiac volume signal (CVS) distorting the tidal and stroke volumes estimated using RVS and CVS. We propose methods to detect MAs cycle by cycle for RVS and CVS, respectively. For RVS, we classify respiratory cycles where RVS variates largely within cycle as abnormal and exclude from the estimation of TV. For CVS, we classify cardiac cycles where its statistical characteristics change abruptly as abnormal and exclude from the estimation of SV. The proposed methods were validated using a clinical data set.

1 Introduction

It is desirable to improve accuracy of non-invasive methods assessing cardiovascular statuses [1]. Jang *et al* has proposed a non-invasive method to estimate TV and SV using EIT data and showed its feasibility by conducting animal experiments [2]. However, the influence by motion was not taken account when estimating of TV and SV from RVS and CVS. We propose MA detection methods for RVS and CVS, respectively. For RVS, we classify respiration cycles as influenced by motion when the impedance change from end-expiration to end-expiration or the maximum respiratory flow are too large. For CVS, at each cardiac cycle we estimate sstandard deviation, kurtosis and skewness of CVS and classify as influenced motion when those statistical parameters changes abruptly.

2 Methods

EIT data were obtained from patients who are receiving haemodialysis by a portable 16-channel EIT device (AirTom-R, Bilab, Korea). RVS was extracted from EIT data by using PCA. CVS was extracted by using PCA, ICA [2]. MAs detection in RVS was proceed as following:

(1) Segment RVS into individual respiration cycle.
(2) Calculate impedance difference at the first and end point of respiration cycle (Z_{diff}) and maximum values of flow during respiration cycles (F_{max}).
(3) Calculate median values of Z_{diff} and F_{max} using two minutes high quality signal and set as reference values: Z_{diff}^{ref} and F_{max}^{ref}.
(4) A respiration cycle is defined as MA when either of the relative changes are higher than predetermined threshold values λ_{diff} and λ_{max}, namely,

$$\frac{Z_{diff}}{Z_{diff}^{ref}} > \lambda_{diff} \quad \text{or} \quad \frac{F_{max}}{F_{max}^{ref}} > \lambda_{max}$$

Here, λ_{diff} and λ_{max} are determined based on receiver operating curve analysis. We first heuristically annotated MAs for 3987 respiration cycles by an experienced person.

And then, the MAs detection algorithm was applied with a given λ_{diff} and λ_{max}. Then, the performance of the proposed method can be evaluated by calculating of the true positive rate (Sensitivity) and the true negative rate (Specificity). We estimated the optimal values of λ_{diff} and λ_{max} by maximizing the sum of sensitivity and specificity under the constraint that sensitivity is no less than 90%. The resulting optimal values of λ_{diff} and λ_{max} were 0.75 and 3.39, respectively. Figure 1 showed the detected MA in RVS by the proposed method. MAs detection in CVS was proceed as following:

(1) Segment CVS into individual cardiac cycles.
(2) Calculate values of standard deviation φ_{std}, kurtosis φ_{kur} and skewness φ_{skew} at each cardiac cycle.
(3) Calculate median values of φ_{std}, φ_{kur}, and φ_{skew} using two minutes high quality signal and set as reference values, φ_{std}^{ref}, φ_{kur}^{ref}, and φ_{skew}^{ref}.
(4) A cardiac cycle is defined as MA if the following criteria are not met: $0.8 \leq \frac{\varphi_{std}}{\varphi_{std}^{ref}} \leq 1.1$, $0.9 \leq \frac{\varphi_{kur}}{\varphi_{kur}^{ref}} \leq 1.1$, and $5.5 \leq \frac{\varphi_{skew}}{\varphi_{skew}^{ref}} \leq 16.2$. The upper and lower bound values were estimated in the similar way for RVS using 40000 cardiac cycles.
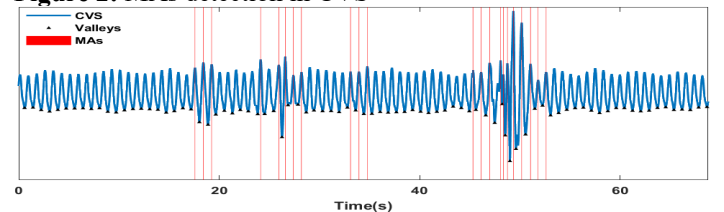
3 Conclusions

The proposed methods showed good performance to detect MAs in RVS and CVS in a clinical data set.

Figure 1: MAs detection in RVS.
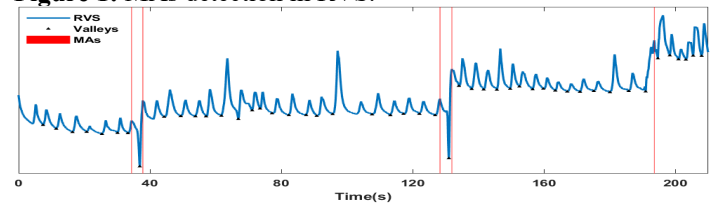
Figure 2: MAs detection in CVS

4 Acknowledgements

References

[1] A Joosten, *et al.*, *Br J Anaesth*, 118:298–310, 2017
[2] GY Jang, *et al.*, *Sci Rep*, 10:11242, 2020

Signal separation in raw EIT measurements

Henryk Richter[1], Lisa Krukewitt[2], Fabian Müller-Graf[2], Jonas Merz[2], Amelie Zitzmann[2], Volker Kühn[1]

[1]Institute of Communications Engineering, University of Rostock, Germany, `henryk.richter@uni-rostock.de`
[2]Department of Anesthesiology and Intensive Care Medicine, University Medical Center Rostock, Rostock, Germany

Abstract: This work is aimed at the separation of EIT signal parts attributed to ventilation and cardiovascular activity prior to reconstruction without reliance on side information like ECG. Our step-wise extraction of signals from raw EIT voltage measurements combines spatial and temporal features and can provide good resilience towards noise.

1 Introduction

EIT has been studied extensively for medical applications in the area of ventilation monitoring and, more recently, monitoring of the perfusion process. The main challenge in this regard is the dominance of the ventilation signal. As a consequence, most approaches towards perfusion monitoring either rely on paused ventilation cycles or side information like ECG gated EIT. Other previous attempts used lowpass/highpass filters or PCA [1, 2]. Our proposal is based on a blind source separation scheme that implicitly builds templates for ventilation cycles.

2 Methods

The analyzed data were part of a larger study on anesthetized ventilated landrace pigs. The data were acquired with the EIT Pioneer Set (Sentec AG, Landquart, Switzerland) using 32 electrodes.

Our approach towards separation between ventilation and other signal parts relies on the relative prominence of ventilation amplitude changes and the periodicity of breath cycles within the EIT measurements. We assume spontaneous breathing with a potentially variable interval between the respective breath cycles.

The first stage of our source separation is based on the estimation of a global template for breath cycles. This template is estimated by a combination of spatial and temporal signal properties. The first step is DC removal $\mathbf{X} = \mathbf{X_m} - \overline{\mathbf{X_m}}$ from the EIT measurements, where the N rows in $\mathbf{X}$ correspond to the individual EIT frames across time and the M columns contain the electrode combination measurements within a single frame. For the ventilation cycle estimation, subset $\mathbf{X_S}$ of size $N \times S$ is extracted from $\mathbf{X}$, where the S columns correspond to the S time series with the largest variances. A 2 Hz Gaussian Lowpass filter $h(t)$ is applied along the columns in $\mathbf{X_S}$, followed by the first order derivative $\mathbf{X_T} = \mathrm{d}/\mathrm{d}t \, \mathbf{X_S} * h(t)$. The positive to negative zero-crossings in $\mathbf{X_T}$ coinciding with amplitudes larger than $1/4$ of the maximum amplitude in the respective time series are marked as candidate positions for the ventilation signal peaks. The estimate of the ventilation peaks is concluded by histogram based majority voting over the count of peaks and their positions, which effectively removes outliers from consideration. In a following step, patches from all time series in $\mathbf{X}$ are extracted at the determined locations whose average forms the breath cycle template vector $\underline{T}$. This template is then LMS fitted to the individual time

series $\hat{\mathbf{X}}_\mathbf{V} = \mathrm{LMS}(\mathbf{X}, \underline{T})$ and subtracted to obtain an estimate of cardiac signals $\hat{\mathbf{X}}_\mathbf{C} = \mathbf{X} - \hat{\mathbf{X}}_\mathbf{V}$ [1].
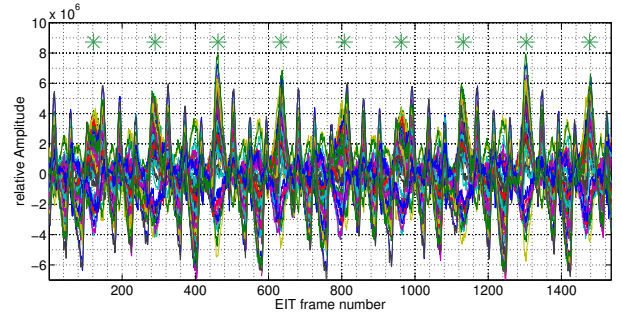
Figure 1: Ventilation cycle detection: selected input signals and estimated ventilation peaks (green markers)

The only major spectral component to be expected in $\hat{\mathbf{X}}_\mathbf{C}$ is the heart rate. We estimate the average heart rate over the observation length by the MUSIC algorithm, followed by peak detection to determine the heart cycle length R. In a follow-up step, ensemble averaging from $\hat{\mathbf{X}}_\mathbf{C}$ yields the cardiac template waveforms $\hat{\mathbf{X}}_\mathbf{R}$ of size $R \times M$. Despite the blind approach of our work, individual sources at the heart rate can be distinguished by their phase information.
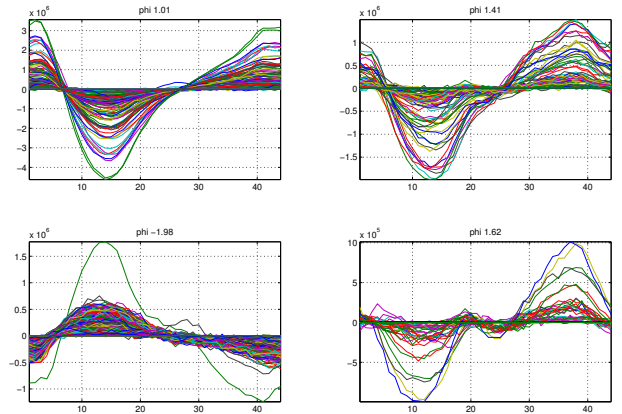
Figure 2: Signals at heart rate after ensemble averaging, grouped by common phase

3 Conclusions

In this paper, we proposed a signal separation approach between ventilation and perfusion operating directly on raw EIT measurements which is robust against ventilation rate changes and varying strength of perfusion signals due to belt placement and test subjects.

References

[1] J M Deibele, H Luepschen, S Leonhardt *Physiol Meas*, 29:1–14, 2008
[2] G Y Jang, Y J Jeong, T Zhang, T I Oh, R-E Ko, C R Chung, G Y Suh, E J Woo *Scientific Reports*, 10:11242 , 2020

Information and measurement system of electrical impedance tomography of laboratory mice's lungs

Grayr K. Aleksanyan and Nadezhda V. Shurygina

Department of information and measurement systems and technologies, Platov South-Russian State Polytechnic University (NPI),
graer@yandex.ru

Abstract: An information and measurement system of electrical impedance tomography was developed to assess the respiratory function of laboratory mice. An electrode system is proposed that does not require sewing the electrodes to the skin of a laboratory animal. The possibility of monitoring the respiratory activity of mice by electrical impedance tomography was confirmed.

1   Introduction

The distribution of ventilation in rats (Wistar) was studied using electrical impedance tomography. Göttingen GoeMF II EIT tomograph (Sensormedics / VIASYS Healthcare, Netherlands) was used [1-3]. Sixteen epicardial pacemakers (Medtronic Inc, Minneapolis, MN, USA) were sewn through the skin and subcutaneous tissue at an equal distance (directly under the animal's front legs which correspond to the middle lung). The use of EIT to assess the ventilation function of the lungs of these animals has not been previously used due to the very small size of laboratory mice.

2   Methods

2.1   Development of an information and measurement system

The constructed electrode system is a ring which made of a dielectric material with an outer diameter of 80 mm and an inner diameter of 60 mm. The ring is perforated with a fixed pitch, there are 16 guide holes into which stainless steel electrodes are inserted. A metal spring is installed on each electrode to ensure its fit to the object of study (laboratory mouse) to ensure skin-electrode contact. Electrode system was made using additive technologies as shown in Fig. 1.
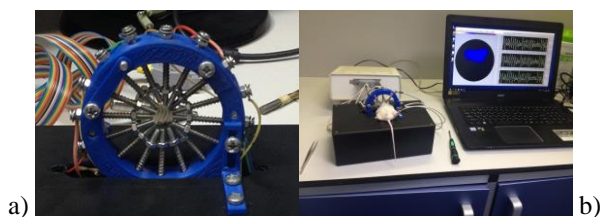
Figure 1: Electrode system (a) and electrical impedance tomography device for laboratory animals (b)

2.2   Assessment of mouse respiratory function

The studies were conducted on laboratory mice (Mus musculus laboratories, BALB/C strain). The measurements were carried out by the EIT at a current (50 kHz, 5 mA) with a frequency of 24 images per second. Fig. 2 shows the change in the conductivity of the chest expressed in terms of the average value of the potential difference between the pairs of electrodes during a single measurement cycle [4], which reflects the integral ventilation function of the lungs. The main harmonics of the signal (Fig. 3) reflect the effect of changes in the conductivity of the lungs and heart of laboratory mice during respiration.
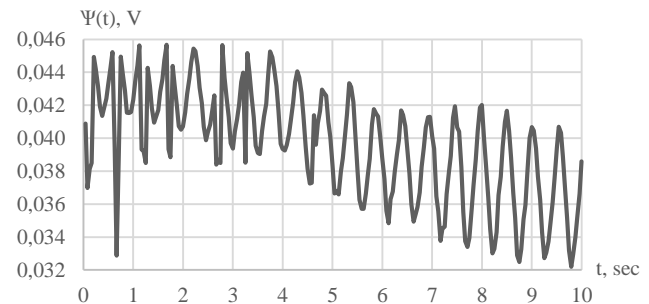
Figure 2: Average value of the potential difference
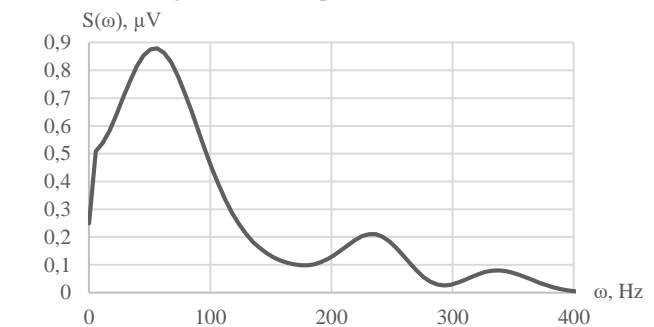
Figure 3: Signal spectrum

3   Conclusions

The values of the respiratory movement frequency of laboratory mice under anesthesia were experimentally obtained by the developed information and measurement system which are in good agreement with the reference data (80-160 breaths per minute). The possibility of monitoring the respiratory activity of a laboratory mouse during surgery was confirmed.

4   Acknowledgements

References

[1] D Rooney, M Friese, JF Fraser, KR Dunster, A Schibler *PhysiolMeas*, 30(10):1075-1085, 2009
[2] KR Dunster, M Friese, JF Fraser, GJ Cowin, A Schibler *BioMedical Engineering OnLine*, 11:64, 2012
[3] KR Dunster, M Friese, JF Fraser, GJ Galloway, GJ Cowin, A Schibler *BioMedical Engineering OnLine*, 11:68, 2012
[4] G Aleksanyan, I Shcherbakov, A Kucher, A Sulyz *AIP Conference Proceedings,* 1952(1):020105, 2018

Separation of respiration and cardiac activity in EIT through harmonic analysis

Alberto Battistel[1], Rongqing Chen[1], Noël Hallemans[2], Rik Pintelon[2], John Lataire[2], Knut Möller[1]

[1]Institute of Technical Medicine (ITeM), Furtwangen University (HFU), Germany, `alberto.battistel@hs-furtwangen.de`
[2]Department ELEC, Vrije Universiteit Brussel, Belgium

Abstract: The separation of the respiration and of the cardiac activity in electrical impedance tomograpy (EIT) is a longstanding problem. In this contribution we show how harmonic analysis can be used to effectively decouple the two contributions.

1 Introduction

EIT is routinely used in the medical field to observe the respiratory cycle of a patient as the dilation of the lungs induce a large variation in the impedance of the thorax. However, cardiac-related changes are also present. These are likely coming from volume changes in the heart and from deformation and shifting of structures within the cardiac cyle [2]. Unfortunately their signal intensity is much lower than that of the respiration.

Given the large difference in the period of the cardiac and respiratory cycle we propose their separation by harmonic analysis through a linear least square fit in the frequency domain. To take into account the dynamicity and time variability of both cycles, the respiration and cardiac-related signals are modeled as amplitude modulated periodic functions according to:

$$y(t) = \sum_{f \in \mathbb{H}} g_f(t) \cos(2\pi f t) - h_f(t) \sin(2\pi f t), \quad (1)$$

where $\mathbb{H}$ is the set of the frequencies consisting of the respiratory f_{r}, the cardiac signal f_{p}, and their harmonics and their intermodulation distortions. The functions $g_f(t)$ and $h_f(t)$ represent, respectively, the in-phase and out-of-phase modulations at the frequency f and can be expressed through suitable polynomials [1].

This idea is demonstrated on a series of EIT images taken on a deeply sedated, intubated, and ventilated patient which guarantees a stable respiration cycle.

2 Methods

A 5 minutes long EIT dataset reconstructed with the GREIT algorithm with a frame rate of 20 Hz was employed. The harmonic analysis was applied in the frequency domain using Hermite functions as envelopes of the amplitude modulation for the frequencies of both the respiration and cardiac cycle. In the time domain the reconstructed global impedance was produced using Hermite polynomials.

3 Results

We used 15 harmonics for the respiration cycle, 3 for the cardiac one, and 2 for the intermodulations. The order of the modulation polynomials were 2 for both respiratory and cardiac signals and 5 for the baseline (zero frequency). Fig. 1 shows the results of the proposed method on the global impedance with the fitting function (reconstructed global impedance a) and the isolated respiratory (b) and cardiac signal (c).

4 Conclusion

The results of this study show that harmonic analysis can be used to separate the contribution of the respiration and cardiac signal in the EIT.
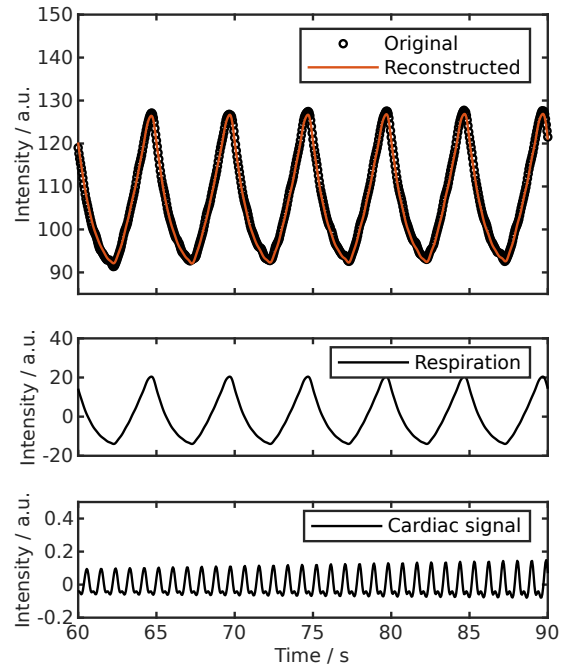
Figure 1: Experimental global impedance (a) and fitted respiration (b) and cardiac cycle (c).

5 Acknowledgements

References

[1] N Hallemans, R Pintelon, X Zhu, T Collet, R Claessens, B Wouters, A Hubin, J Lataire *IEEE Trans. Instrum. Meas*, 70: 1–14, 2021
[2] JM Deibele, H Luepschen, S Leonhardt *Physiol. Meas.*, 29: S1–S14, 2008

Prior-Based Unsupervised Separation of Cardiac-Related Signals

Diogo Silva[1], Utku Özmü[1], Steffen Leonhardt[1], Chuong Ngo[1]

[1]Chair of Medical Information Technology, RWTH Aachen University, Aachen, `silva@hia.rwth-aachen.de`

Abstract: A reinforcement learning (RL) algorithm was employed in source-separation of perfusion and ventilation. For this, an EIDORS-Simulink framework was built, with the implementation of two agents, custom reward functions and actions. Results show accurate reconstructions in time, frequency and space.

1 Introduction

While accurate regional ventilation monitoring is possible in Electrical Impedance Tomography (EIT), current methods for non-invasive, real-time perfusion estimation are sub-optimal. To this end, Machine learning algorithms would be a good solution, but they require large amounts of training data. Therefore, this paper presents some results of the ongoing endeavour to accurately isolate perfusion from ventilation in real-time through a lightly tackled approach: unsupervised, prior-guided reconstruction via Deep Deterministic Policy Gradient (DDPG) RL.

2 Methods

A joint framework bridging EIDORS and MATLAB®'s RL Toolbox in Simulink® was set up with the following components: forward solver, inverse solver and agents. Here, we will only focus on the latter. An extruded finite element model was built with contours from real human computer tomography scans. The heart and lungs were represented as a static collection of elements (x, y), whose conductivities oscillate sinusoidally over time:

$$\sigma(t) = \begin{cases} \alpha_{(x,y)} \cdot \sigma_{\text{CRS}}(t), & \text{if}(x,y) \in \text{heart}, \\ \alpha_{(x,y)} \cdot \sigma_{\text{CRS}}(t - \phi_{(x,y)}) \\ + \beta_{(x,y)} \cdot \sigma_{\text{VRS}}(t), & \text{if}(x,y) \in \text{lung}, \end{cases} \quad (1)$$

where cardiac- (CRS) and ventilation-related source signals (VRS) are σ_{CRS} and σ_{VRS}, respectively, the α and β terms are scalars, with $\beta > 10 \cdot \alpha, (x, y) \in \text{lung}$, and ϕ terms are time delays.

The simulated measurements were then reconstructed using GREIT[1] and two agents were developed to post-process the resulting images. Each agent follows a DDPG actor-critic architecture. Two frequency reward functions $R_{f,\text{VRS}}(|\Sigma(f)|)$ and $R_{f,\text{CRS}}(|\Sigma(f)|)$, where $\mathcal{F}\{\sigma(t)\} = \Sigma(f)$, were defined as normally distributed positive values around 0.2 Hz and 1 Hz, respectively, and negative values in the surrounding regions. A phase reward function $R_{\phi,\text{CRS}}(\angle\Sigma(f), x, y)$ was defined as the expected phase distribution, assuming the CRS signal delay in the lungs increases radially with respect to the heart, and an intensity reward function $R_{I,\text{CRS}}(x, y)$ as the expected intensity distribution, assuming the CRS is more intense in the heart and follows a dorsally skewed gamma distribution in the lungs. Agent 1 acts on a pixel's signal $\sigma_{(x_0,y_0)}(t)$, mediated by $R_{f,\text{VRS}}$, finding $\gamma_{(x_0,y_0)}(t)$ such that

$$\hat{\sigma}_{\text{VRS},(x_0,y_0)}(t) = \gamma_{(x_0,y_0)}(t) \cdot \sigma_{(x_0,y_0)}(t), \quad (2)$$

where $\hat{\sigma}_{\text{VRS},(x_0,y_0)}$ is a VRS template. Agent 2 acts on every pixel's signal, mediated by the compound reward $R_{f,\text{CRS}} \cdot R_{I,\text{CRS}} + R_{\phi,\text{CRS}}$, finding $A_{(x,y)}$ such that

$$\hat{\sigma}_{\text{CRS},(x,y)}(t) = \sigma_{(x,y)}(t) - A_{(x,y)} \cdot \hat{\sigma}_{\text{VRS}}, \quad (3)$$

where $\hat{\sigma}_{\text{CRS},(x,y)}$ is the CRS signal estimation. The joint training of the agents tunes their actions towards producing a $\hat{\sigma}_{\text{VRS}}$ that is highly rewarded from $R_{f,\text{VRS}}$, and a $\hat{\sigma}_{\text{CRS}}$ that is highly rewarded from $R_{f,\text{CRS}} \cdot R_{I,\text{CRS}} + R_{\phi,\text{CRS}}$.

3 Results & Discussion

The learning process is depicted in time and frequency domain in Figure 1, and in the image domain in Figure 2. After convergence around episode 80 (number of times the reconstructed data was processed), both the CRS and VRS sinusoidal waveforms were well estimated, leading to a good rejection of the VRS frequency band. Furthermore, the CRS is reasonably accurate in space and faithfully depicts the simulated delayed expansion from the heart to the lungs.
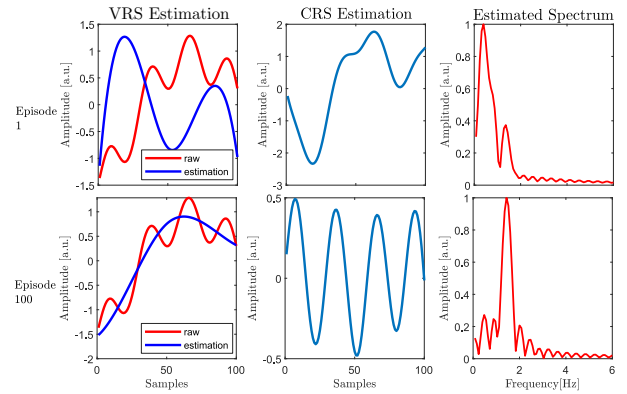
Figure 1: Time and frequency analysis of the estimation.
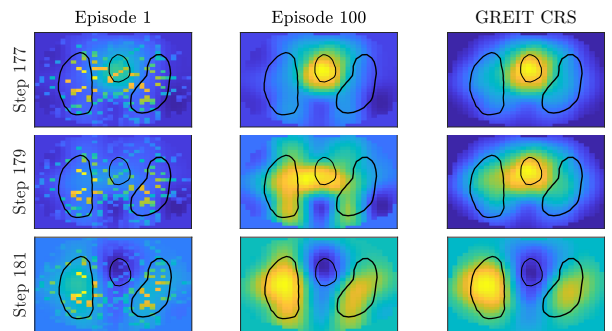

Figure 2: Reconstructed estimated and original EIT images.

4 Conclusions

These preliminary results showcase a way to restrict the solution space of the source-separation problem with prior knowledge in an unsupervised fashion. Thus, our algorithm requires less data and performs in real-time. This RL framework for EIT would also allow different agent implementations with new reward policies accounting for other signal sources at every stage of the EIT pipeline: from pre- to post-processing and/or reconstruction.

References

[1] A Adler, B Grychtol, R Bayford et al. *Physiol Meas*, 30:35–55, 2009

Monitoring of upper airway obstruction using two-plane EIT images

Tingting Zhang[1], Jinwon Mok[1], Sang-Wook Kim[2], Tong In Oh[1]

[1]Department of Biomedical Engineering, College of Medicine, Kyung Hee University, `zttysu@khu.ac.kr`
[2]Department of Otorhinolaryngology, Gyeongsang National University Hospital

Abstract: Identifying the phenotype of obstructive sleep apnea for each patient and determining a patient-specific treatment plan are important to improve the success rate of surgical treatment for sleep apnea. For continuous and non-invasive monitoring of upper airway obstruction, we acquired two-plane EIT images during sleep while performing CT and PSG measurements simultaneously. We presented that multi-layered EIT images combined with PSG could be used to analyze patient-specific occlusion patterns.

1 Introduction

Obstructive sleep apnea (OSA) occurs as a partial or complete obstruction of the upper airway during sleep, which is commonly diagnosed by overnight polysomnography (PSG) [1]. In the preliminary study, conducted simultaneously with overnight PSG, we confirmed the detectability of upper airway obstruction from EIT images measured through 16 electrodes attached to the lower jaw [2]. However, in order to improve the success rate of surgical treatment in OSA patients, we need to identify the phenotype of upper airway obstruction in 3D during natural sleep and make a patient-specific treatment plan. In this study, we compared EIT images from the upper and lower layers of the upper airway with 3D CT images measured simultaneously to verify the feasibility of non-invasive monitoring the degree of occlusion in two planes.

2 Methods

After inducing natural sleep inside a CT scanner for 17 OSA patients, 3D CT images were taken in the sections of normal breathing, hypopnea, and apnea determined from PSG signals while recording PSG and two-plane EIT images simultaneously. Time-series of EIT measurements for upper ($\mathbf{V}_u$) and lower ($\mathbf{V}_l$) layers were fast acquired alternately via a switching system connected to the AirTom-R (Bi-Lab, Korea). Signal components related to upper airway obstruction were extracted and reconstructed conductivity images by applying the source consistency EIT algorithm using PSG signals measured at the same time [2, 3].

The reference EIT image was obtained in the normal breathing section before inducing sleep. Time-difference EIT (tdEIT) images of the upper and lower layers for the upper airway were reconstructed using the EIT voltage data measured at the same time as the CT scan in different OSA events determined from the PSG signal [2, 4]. The following parameters acquired from each medical modality were presented:

- EIT: upper-layer conductivity σU, the lower-layer conductivity σL variations calculated from the corresponding reconstructed tdEIT images measured at the same time with CT images

- CT: upper-layer and lower-layer CT images
- PSG: nasal pressure, thermistor, thorax/abdomen movements, and SpO$_2$

3 Results

Figure 1 shows an example in the apnea section during sleep. When we analyzed all measured images on the different OSA events, the change in the degree of upper airway obstruction in the CT image taken simultaneously with the tdEIT image had a linear relationship.
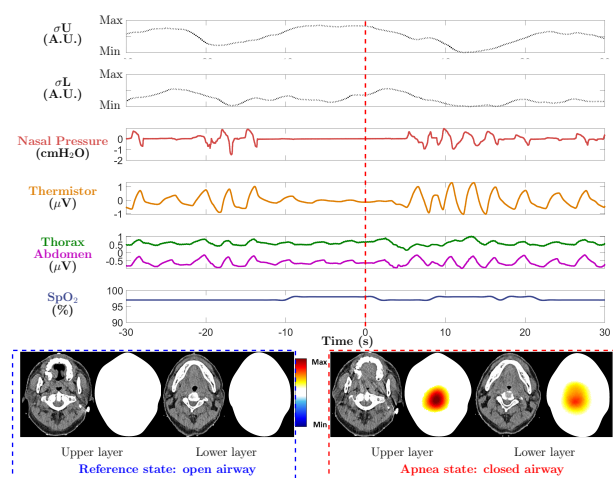
Figure 1: Simultaneous EIT/PSG/CT recordings. The dashed red line indicates the moment when apnea took place and a CT scan was taken.

4 Conclusions

In order to determine the degree of occlusion in the upper and lower levels of the upper airway and to analyze the phenotype for each patient, two-plane EIT images and PSG were simultaneously measured. We verified the measurability of upper airway region change by comparing it with CT images.

5 Acknowledgements

References

[1] RB Berry, L Claude, SM Albertario, RM Harding, DT Lloyd *et. al.* *The AASM manual for the scoring of sleep and associated events: rules, terminology and technical specifications*, 2018
[2] G Ayoub, YE Kim, TI Oh, SW Kim, EJ Woo *Annals of biomedical engineering*, 47: 990-999, 2019
[3] T Zhang, GY Jang, TI Oh, KW Jeung, H Wi, EJ Woo *SIAM Journal on Applied Mathematics*, 80: 499-520, 2020
[4] K Lee, EJ Woo, JK Seo *IEEE transactions on medical imaging*, 37: 1970-1977, 2017

Session 5: Applications I

Multimodal mfEIT for *in vitro* applications

Mari Lehti-Polojärvi[1], Mikko J. Räsänen[2], Aku Seppänen[2] and Jari Hyttinen[1]

[1]Faculty of Medicine and Health Technology, Tampere University, Finland, mari.lehti-polojarvi@tuni.fi
[2]Department of Applied Physics, University of Eastern Finland, Finland, mikko.rasanen@uef.fi

Abstract: We propose to fuse multifrequency electrical impedance tomography (mfEIT) with optical projection tomography (OPT) to obtain a novel tool for three dimensional (3D) *in vitro* cell culture analysis. Our data fusion methods enable accurate retrieval of both sample morphology and conductivity spectrum.

1 Introduction

Tissue engineered 3D samples are challenging to image noninvasively with conventional microscopy techniques due to samples' thickness. MfEIT provides a spatial conductivity map on a range of applied frequencies and it has been shown to be an effective tool for, e.g., imaging of cells in 3D scaffolds [1]. In OPT, projection images are captured from a rotated object and a morphological 3D image is reconstructed. We use this as *a prior* information in mfEIT reconstruction to obtain an accurate conductivity spectrum of the sample. **We aim** to create a novel OPT-mfEIT technique for live 3D sample imaging *in vitro*.

2 Methods

Here we extend the rotational limited angle mfEIT technique [2,3] to 3D using 16 electrodes on two layers placed on two opposing walls (Fig. 1). This setup allows simultaneous OPT and mfEIT acquisition. The used mfEIT device [4] applies chirp excitation that provides impedance data at 15 frequencies in the range of 1 kHz-349 kHz at each measurement. OPT was acquired every 0.9° over 360° rotation and mfEIT every 4.5° over 180° rotation. We measured 390 tetrapolar impedance values at each rotational position.

From OPT, the 3D volume was reconstructed with a filtered backprojection algorithm and then segmented for data fusion. Segmented tissues were incorporated into mfEIT reconstruction that applied rotational meshing and Bayesian inversion methods.

The feasibility of the OPT-mfEIT technique was evaluated experimentally. We measured fresh and Triton X-100-treated porcine liver tissues embedded in agarose gel (prepared in phosphate buffered saline (PBS)). Each sample contained two pieces of tissue: one fresh and one treated. The samples were rotated in PBS solution during imaging.
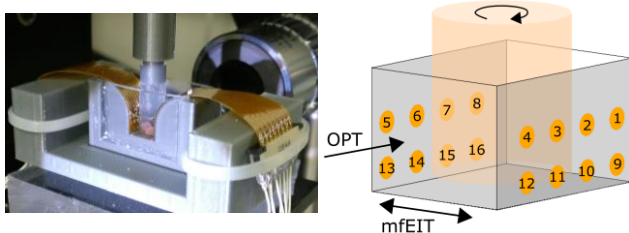
Figure 1: Photograph of the OPT-mfEIT setup (left). Model of the imaging chamber with rotated sample and 16 electrodes (right).

Figure 2: (a) Conductivity spectra of porcine liver tissues and backgrounds obtained from the OPT-mfEIT reconstructions. (b) 3D visualization of the OPT-mfEIT reconstruction of the liver 1 sample at 7 kHz. Tissue colours are matched with the graph in (a). Background represents the whole volume inside the box, except the tissues.
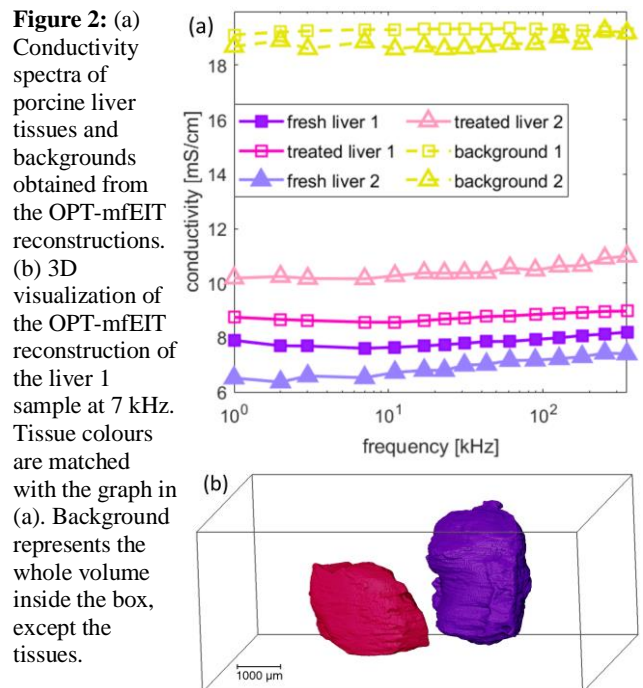
3 Results and conclusions

The conductivity spectra in Fig. 2 (a) show the difference in fresh and treated porcine liver tissues. All treated inclusions show higher conductivity than the fresh inclusions - even when the tissues were very close to each other, as shown in Fig. 2 (b). This difference is caused by the breakage of the cell membranes in treatment: when membranes break, the electric current passes straight through the well conducting cytoplasm. All background conductivity values are approximately 19 mS/cm, which is close to PBS conductivity.

The results show the power of multimodal tomography and data fusion. The proposed technique provides a new avenue to study tissue engineered samples *in vitro* that is of interest, e.g., in drug development and disease modeling.

4 Acknowledgements

References

[1] H Wu et al. *Materials*, 11:930, 2018
[2] M Lehti-Polojärvi, O Koskela et al. *Meas Sci Technol*, 29:025401, 2018
[3] M Lehti-Polojärvi et al., *Conf 20th EIT*, p.44, London, UK, Jul 2019
[4] M Min et al. *IJBEM*, 209:76-79, 2018

MR-based low-frequency electrical conductivity tensor imaging using DTMREIT and CTI: a comparison study

Saurav Z K Sajib[1], Munish Chauhan[1], Sulagna Sahu[1], Enock Boakye[1], Rosalind J Sadleir[1]

[1]School of Biological and Health Systems Engineering, Arizona State University, Rosalind.Sadleir@asu.edu

Abstract: Diffusion tensor magnetic resonance electrical impedance tomography (DT-MREIT) and electrodeless conductivity tensor imaging (CTI) are two emerging modalities that can quantify low-frequency tissue anisotropic conductivity properties by considering the relationship between ion mobility and water diffusion. While both methods have potential applications to estimating neuro-modulation fields or formulating forward models used for electrical source imaging, a direct comparison of these two modalities has not yet been performed. Therefore, the aim of this study to test the equivalence of these two modalities.

1 Introduction

Standard MREIT methods cannot be used for anisotropic imaging because of noise in measured data. Kwon et al.[1] developed the DT-MREIT technique to reconstruct conductivity distributions using external-current-induced magnetic flux density (B_z) and a priori anisotropic information contained in diffusion tensor (D) data. However, DT-MREIT methods require external current application, which may involve risk of injury or peripheral neural stimulation. Sajib et al. [2] later developed the electrodeless CTI method, which can provide both isotropic and anisotropic conductivity distributions, by decomposing the high-frequency conductivity σH measured using MR Electrical Properties Tomography [3] (MREPT) into its extra- and intra-cellular parts and incorporating the tissue microstructure parameters estimated from multi-b-value diffusion-weighted images. In the literature, both DT-MREIT and CTI methods have been used to determine the anisotropic conductivity distribution of in-vivo canine [4] and human brains [5]. However, the equivalence of these two modalities has not yet been investigated. Therefore, this study aims to determine if low-frequency electrical tissue conductivity determined using MREIT, DT-MREIT, and CTI methods in a single biological tissue phantom are the same.

2 Methods

A cylindrical acrylic container with a diameter of 150 mm and a height of 140 mm was used to build the biological tissue phantom. Two opposing pairs of 50 x 50 mm^2 carbon electrodes (HUREV, South Korea) were attached to the container perimeter. Three sections of bovine muscle, oriented in x (left), y (right), and z-directions (top) were then placed inside the chamber to provide anisotropic tissue properties along with TX-151 anomaly. The phantom background was then filled with a 0.75 S/m (10 Hz) agarose gel. All MR data were acquired using a 32-channel RF head coil in a 3.0T Phillips scanner (Phillips, Ingenia, Netherlands). Imaging parameters used in this study are described in [6]. A transcranial electrical stimulator (neuroConn,Germany) was used to deliver a 4.0 mA current through the two pairs of opposing electrodes (E=1,2).

In CTI-theory[10], the low-frequency equivalent isotropic conductivity, $\sigma_L^{\text{CTI}} = \eta^{\text{CTI}} d_e^w$ and anisotropic conductivity tensor, $\mathbf{C}^{\text{CTI}} = \eta^{\text{CTI}} \mathbf{D}_e^w$ is estimated from the extra-cellular water self-diffusivity, d_e^w and diffusion tensor $\mathbf{D}_e^w$. The scale-factor η is expressed as[10]

$$\eta^{\text{CTI}} = \frac{\alpha \sigma_H}{\alpha d_e^w + \beta(1-\alpha)d_i^w}$$

where, $1-\alpha, d_i^w$ denotes the intra-cellular space volume fraction and water diffusivity, respectively and β is the intra-to-extra-cellular ion concentration ratio.

For DTMREIT, using the estimated projected current density [7] $\mathbf{J}^{P,\mathcal{E}}, \mathcal{E} = 1,2$ from current applications we determined the effective isotropic conductivity [8] (σ_L^{EIT}) and conductivity tensor [1] ($\mathbf{C}^{\text{EIT}} = \eta^{\text{EIT}} \mathbf{D}_e^w$).

2.1 Figures

For CTI image reconstruction we set the unknown β-value at 1.0. The reconstructed scale-factor η obtained using CTI (β=1) or DT-MREIT data are displayed in Fig. 1(a) and (e) respectively.
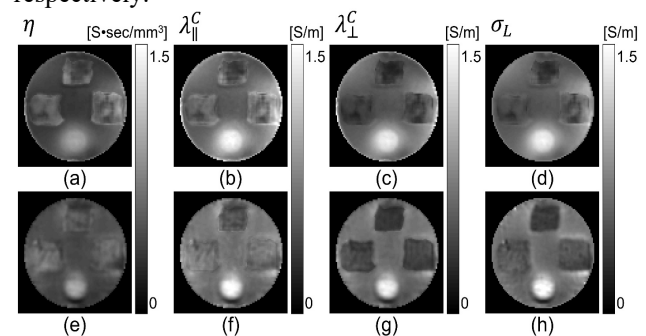
Figure 1: (a) Reconstructed scale factor images obtained from CTI with β=1 (b) Scale factors found using DT-MREIT method. The longitudinal and transversal components of the conductivity tensors are displayed in (b)-(c) for CTI and (f)-(g) for the DT-MREIT method. The low-frequency equivalent isotropic conductivity obtained from the CTI and MREIT method are shown in (d) and (h), respectively.

3 Conclusions

Using a biological tissue phantom data, we have demonstrated that the CTI and DT-MREIT method may provide equivalent tissue conductivity.

4 Acknowledgements

References

[1] Kwon O I, et al. Phys. Med. Biol. 59 (12): 2955-74,2014
[2] Sajib S Z K et al. Biomed. Eng. Lett. 8(3): 273-82,2018
[3] Seo J K at al. Inverse Problems. 28(8):084002, 2012.
[4] Jeong W C et al. IEEE Trans. Med. Imag. 36(1):124-31, 2017.
[5] Chauhan M. et al. IEEE Trans. Med. Imag. 37(4):966-76, 2018
[6] Sajib S Z K et al. *Proc. Intl. Soc. Mag. Reson. Med.* 2021,3786, 2021
[7] Park C et al. Phys. Med. Biol. 52(11):3001-13, 2007.
[8] Nam H S et al. Phys. Med. Biol.;53(23):6947-61 2008.

Simulation Study of a New EIT-based Surgical Margin Probe

Shannon Kossmann[1], Ethan K. Murphy[1], Allaire Doussan[1], and Ryan. J. Halter[1,2]

[1]Thayer School of Engineering, Dartmouth College, Hanover, NH, USA, shannon.e.kossmann.th@dartmouth.edu
[2]Geisel School of Medicine, Dartmouth College, Hanover, NH, USA

Abstract: In conjunction with new hardware development of an upgraded EIT-based surgical margin probe for use during prostatectomy we have modelled, simulated, and analysed several electrode arrays that aim to reduce the number of current injecting electrodes and their contact impedance while maintaining imaging capabilities.

1   Introduction

Currently there is no efficient and reliable technique to routinely assess surgical margins during robot-assisted laparoscopic prostatectomy (RALP). Our group has been developing a surgical robot compatible EIT probe for the specific purpose of performing intraoperative surgical margin assessment . In our prior work [1] we found good predictive power discriminating cancerous from benign tissue (area-under the curve (AUC) values of 0.85) in an ex vivo study of 19 prostates. In ongoing work, we are redesigning the hardware and electrode-array to improve signal-to-noise (SNR) while maintaining similar EIT imaging capabilities. Active hardware is being moved to the probe tip, which requires reducing the number of current-drive electrodes to make the probe compatible with the limited space available during RALP. This abstract summarizes updates to the electrode array design evaluated via 3D Finite Element Method (FEM) modelling and simulation.

2   Methods

The FEM mesh developed encodes the electrode boundaries into the mesh via a 2-step process. In the first step, a coarse 2D boundary mesh is constructed using distmesh, which in the 2nd step is input to gmsh where the full 3D mesh is generated. Following this, an iterative adaptive mesh refinement is performed that improves mesh quality based on *a posteriori* error estimate. The open-domain aspect of the problem is modelled by sufficiently extending the modelled tissue volume to effectively minimize the impact of domain boundaries on voltage measurements. Specifically, the electrode array spans an ~8 mm diameter across the top of the domain while the full FEM mesh extends +/-40 mm in the x/y-direction (horizontal) and 40 mm in depth (below the electrodes). The electrode arrays are comprised of a central 5x5 square grid of voltage sensing electrodes (0.8 mm diameter with 1 mm centre-to-centre spacing), and 4 (Fig. 1A) or 8 (Fig. 1B) outer current-source/sink electrodes. The outer electrodes are large to reduce the contact impedance effect. The optimized meshes are ~250k nodes and ~1.45M elements.

The inverse mesh is based on the dual mesh method and relies on determining an imaging region of interest based on a sensitivity-threshold approach [2]. The forward mesh uses a tuned fine mesh that minimizes computational cost while providing sufficient accuracy [2]. To account for discrete electrodes, the boundary conditions at the electrodes are defined using the complete electrode model (CEM) [2]. Simulated tissue conductivity and permittivity values came from our prior work [3].

2.1   Figures
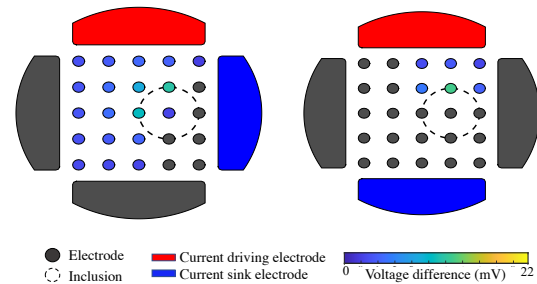
Figure 1: Simulated absolute voltage differences measured at electrodes with and without a tumor inclusion (2mm diameter with benign-to-tumor contrast of ~20%); non-gray electrodes denote voltage differences above a noise threshold of 0.1% of the maximum simulated voltage (i.e. assumes 60dB precision).
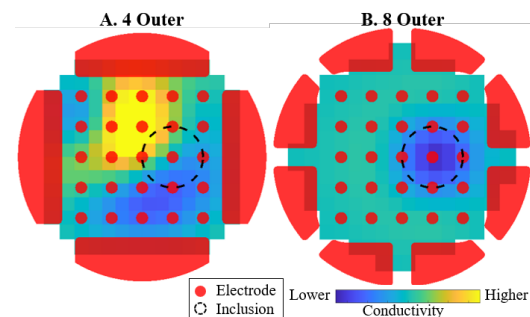
Figure 2: EIT difference reconstructions of a 2mm diameter tumor (~10% contrast) with A. 4- and B. 8-outer current injecting electrodes and interior voltage sensing electrodes.

3   Conclusions

Simulation-based hardware design is becoming more ubiquitous in the design of medical devices. The simulations present here are helping to guide the optimal design of our next surgical margin probe. Large current driving electrodes were selected to help to minimize contact impedance in this small form-factor probe. While four current driving electrodes are sufficient to detect the presence of tumors at least 2 mm in diameter (Fig 1), 4 current driving electrodes are insufficient to localize inclusions (Fig 2A). Thus, an 8 current-source/sink electrode design is suggested for this application (Fig 2B).

4   Acknowledgements

References

[1] Murphy E, et al., Physiol. Meas., Vol. 38, pp.12-41-1261, 2017
[2] Murphy, Mahara, Halter, IEEE Trans. Med Imag, vol. 35, 2016.
[3] Halter, R. et al., J. Urology, vol. 182, pp. 1600-1607, 2009.

Electrical Impedance Tomography Nanoparticle Localisation

Richard H Bayford[1], Rui Damaso[1,2], Nazanin Neshatvar[2], Yevhen Ivanenko[3], Thomas W Rademacher[1], Yu Wu[2], Nima Seifnaraghi[1], Lucy Ghali[1], Nakul Patel[1], Ivan Roitt[1], Sven Nordebo[4], and Andreas Demosthenous[2]

[1]Middlesex University, UK, r.bayford@mdx.ac.uk, [2]University College London, UK,[3] Blekinge Institute of Technology, Karlskrona, Sweden, [4] Linnaeus University, Växjö, Sweden

Abstract: An imaging device to locate functionalised nanoparticles remains a challenge for pharmaceutical research. Here, we show a new method based on electrical impedance tomography (EIT) to provide images of the location of gold nanoparticles (GNPs) when they are excited with radio frequencies (RF). The RF excitation causes a change in impedance permitting an estimation of their location in cells. A quantification was carried out using the internalisation of GNPs into the colorectal cancer cells. When the cells were incubated with functionalised GNPs, the change was more apparent, approximately 40±2%.

1. Introduction

Targeted drug delivery, whereby therapeutic agents are transported from the site of administration specifically to diseased tissues, remains a key issue of pharmaceutical research. Nanomedicine, which employs nanoparticle-mediated drug delivery can be used to overcome this problem in conventional drug delivery [1]. Ultra-small nanoparticles that can permeate vessels and move by convection in tissues and cross tissue barriers, can be loaded with drugs and retained in specific diseased tissue locations in the body limiting interaction with healthy tissue. The goal is to localise and prolong drug delivery in order to focus drug interaction with the diseased tissue. The advantages of this approach are reduction in the frequency of the dosages taken by the patient and obtainment of a uniform effect of the drug, resulting in minimisation of drug side effects [1], systemic toxicity and improved treatment outcomes. New tools are required to facilitate customisation of therapy based on the specific needs of individual patients. In the drug delivery paradigm, imaging may be used to identify the target and non-target anatomy or for screening, planning, monitoring, and postprocedural assessment of treatment outcome [2]. A novel EIT method to locate nanoparticles below 5 nm diameter in human tissue is presented.

2. Methods

The system used for EIT imaging is the SenTec Pioneer Set. All experiments were recorded at 1 fps; the injected current was 7 mA at 250 kHz. The raw data extracted was analyzed in MATLAB and EIDORS software to reconstruct the images. The reconstruction algorithm was based on difference imaging with respect to the reference image using the GREIT algorithm [3]. All measurements were recorded for 7 minutes; during the first 2 minutes the power amplifier was off. The images from this period were used as the reference. Then the power amplifier was turned on for 5 minutes while continuous live monitoring of the samples was obtained.

A cell model was created consisting of colon epithelial and colorectal cancer cells with GNPs in cancer cells. This cell model was placed in a custom-made ring of 32 gold-plated electrodes of size 1 mm × 1.5 mm designed to be interfaced with the EIT system. A well of 2.9 cm diameter, 1 cm height and 1 mm thickness was designed and placed onto the PCB-unit to contain the samples within the electrode ring during the experiments. Each electrode was connected to the EIT system by a ribbon cable.

3. Results

Coverslips containing colorectal cancer and normal colon epithelia cells were incubated with culture media, GNP-CS, or GNP-FA. Once the reference was taken, all sets were exposed to an RF field for 5 minutes and the resultant EIT images are shown in Figs. 1(a)-(c). The case, when a coverslip contained normal colon epithelium cells, was also considered; see Fig. 1(d).
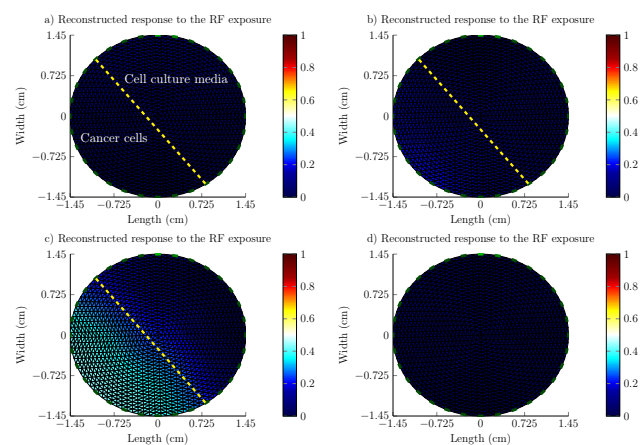
Figure 1: Human colorectal cancer cells grown in cell culture media, were incubated with (a) no GNPs, (b) GNP-CS solution, (c) GNP-FA solution. After RF exposure for 5 minutes, EIT reconstruction was obtained. Dashed line represents the area covered by CRL2159 cells, occupying ~40 % of well area. (d) CRL1790 after RF exposure. The color bar represents the normalized values as percentage change from dark blue (0%) to red (100%).

3. Conclusions

A method for location of functionalized GNPs using EIT has been presented. It has demonstrated that functionalized GNPs in colorectal cell line can be located and validated with sufficient contrast change in the EIT images with RF excitation. It has also been demonstrated that colorectal cancer cells incubated with culture media, with internalisation of GNPs into the colorectal cancer cells, resulted in an impedance change of approximately 40±2%.

4. Acknowledgements

References

[1] K. Patra, et. al., J Nanobiotechnology, vol 16 pp1-33, 2018.
[2] J. Patra, et. al., Journal of Nanobiotechnology, no. https://doi.org/10.1186/s12951-018-0392-8, 2018.
[3] A. Adler, et. al., "Physiological Measurement, Volume 30, Number 6, pp. Volume 30, Number 6, 2009.

Rotational mfEIT constrained by optical image segmentation

Mikko J. Räsänen[1], Mari Lehti-Polojärvi[2], Aku Seppänen[1], Jari Hyttinen[2]

[1]Department of Applied Physics, University of Eastern Finland, Finland, `mikko.rasanen@uef.fi`
[2]Faculty of Medicine and Health Technology, Tampere University, Finland, `mari.lehti-polojarvi@tuni.fi`

Abstract: In this study, methods for the data fusion of rotational multifrequency electrical impedance tomography (R-mfEIT) with optical projection tomography (OPT) were developed. The approach was tested with experimental data from a 3D *in vitro* imaging setup.

1 Introduction

In rotational EIT, the number of independent measurements is increased by rotating the imaging target in steps and repeating the measurements after each step. Rotational multifrequency EIT (R-mfEIT) has been previously presented in [1] using a limited electrode coverage, which allows for hybrid optical and mfEIT imaging. This study extends the approach to 3D, and integrates R-mfEIT with OPT by constraining the R-mfEIT reconstruction based on segmented OPT reconstruction.

2 Methods

The computational framework for modelling rotational EIT measurements [2] was extended to a 3D imaging setup. Rotational modelling was used in combination with R-mfEIT data to estimate the conductivity spectrum of the target. In our approach, the R-mfEIT data was used by computing rotational EIT reconstructions separately at each frequency. The information provided by OPT was incorporated into R-mfEIT reconstruction by segmenting the OPT image into separate electrically relevant volumes, and requiring the conductivity within each segment to be constant. This stabilized the inverse problem and provided a straightforward method to estimate the conductivity spectrum of the target.
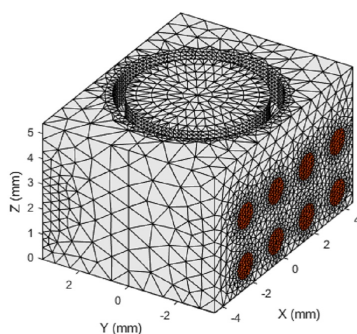
Figure 1: Surface of the 3D finite element mesh used to model the R-mfEIT measurements. Eight electrodes are colored in red. The remaining eight electrodes are located on the opposite side. Zero flux boundary condition was applied on the boundary of the plastic tube at the top of the chamber.

To validate the computational methods developed in this study, experimental data from a 3D imaging setup was used. The target consisted of a tetrahedral piece of potato embedded in a hydrogel cylinder, which was held by a plastic tube. A previously presented mfEIT device [3] was used. The experiment was performed in a saline-filled imaging chamber with 16 electrodes on two planes on opposing walls. The remaining opposing walls were transparent for OPT imaging. The sample was rotated in 4.5° steps for 180°, and EIT measurements were taken at frequencies ranging from 1 to 349 kHz. The electrically relevant regions segmented from OPT images were the potato volume, plastic tube, and background segment consisting of saline and hydrogel. The plastic tube was modelled as an insulator (Fig. 1), and the conductivities of the potato sample and background segment were estimated at each frequency.

3 Results and conclusions

By using the OPT segmentation to constrain the R-mfEIT reconstruction, the conductivity spectrum of the potato sample is readily obtained (Fig. 2). The conductivity of the potato increases with frequency, while the background remains constant. The estimated conductivity spectrum of the potato behaves similarly to results in previous studies [4].

The results demonstrate the feasibility of fusing OPT with R-mfEIT in a 3D setup. In future, this technique will provide a tool for monitoring the growth and viability of 3D tissue engineering constructs *in vitro*. The methods are also applicable to characterizing different types of biological samples.
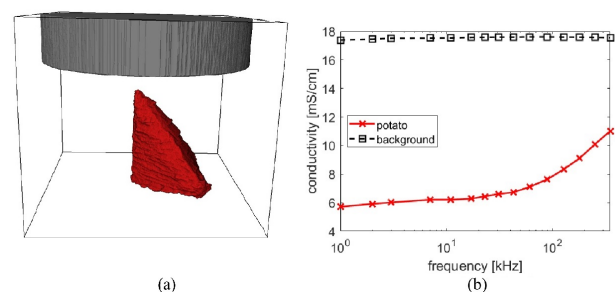
Figure 2: (a) Segmentation of OPT reconstruction into potato (red) and plastic tube (gray) segments. The rest of the imaging volume forms the background segment. (b) EIT reconstructions at all frequencies constrained by the OPT segmentation, resulting in the estimated conductivity spectra of the background and the potato sample.

4 Acknowledgements

References

[1] M Lehti-Polojärvi, O Koskela et al. *Meas Sci Technol*, 29:025401, 2018
[2] O Koskela, M Lehti-Polojärvi et al. *World Cong Med Phys and Biomed Eng*, 2:901-904, 2018
[3] M Min et al. *IJBEM*, 209:76-79, 2018
[4] S Ahn et al. *J. Phys.: Conf. Ser.*, 224:012152, 2010

Deep learning based EIT image reconstruction for tissue engineering

Xipeng Yin[1], Jiazheng Wang[1], Zhou Chen[2], Wei Zhou[1] and Yunjie Yang[2]

[1]School of Electronics and Information, Northwestern Polytechnical University, Xi'an, China
[2]Agile Tomography Group, School of Engineering, The University of Edinburgh, Edinburgh, UK, y.yang@ed.ac.uk

Abstract: We report a learning based EIT image reconstruction method to monitor the cancer tissue invasion process. Electrical Impedance Map (EIM) and Deep Convolution Neural Network (DCNN) are applied to reconstruct the simulated tissue phantoms with multi-level and overlapping conductivity distributions.

1   Introduction

We investigate the application of EIT in non-destructive and label-free monitoring of cancer invasion and metastasis in tissue engineering [1]. To this end, we conduct a proof-of-concept study of imaging simulated cancer invasion phantoms based on learning approaches. To address the more challenging task to reconstruct the shape and conductivity of the multi-level and overlapping conductivity distributions, we leverage the recently proposed concept of Electrical Impedance Map (EIM) to extract geometric features of the measurement and benefit the image reconstruction process [2]. We then propose an image reconstruction method by combining EIM and DCNN to tackle this problem.

2   Methods

2.1   Dataset

As shown in Fig. 1, we establish an EIT dataset based on simulation to mimic cancer invasion in tissue engineering. We adopt a circular 16-electrode EIT sensor structure and simulate four types of phantoms: A) circular phantoms; B) square phantoms; C) circular inclusions; D) square combinations. In total, 29,581 samples are obtained by using COMSOL and the measurements are rearranged following the format of EIM [2]. Additive noise with SNR of 50dB, 40dB and 30dB is added to EIM.
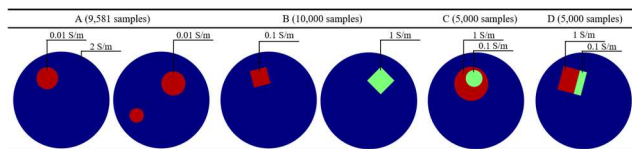
Figure 1: Typical samples of the simulated EIT dataset.

2.2   Network Architecture and Training

Fig. 2 shows the architecture of DCNN, which consists a feature extraction and an image reconstruction module.
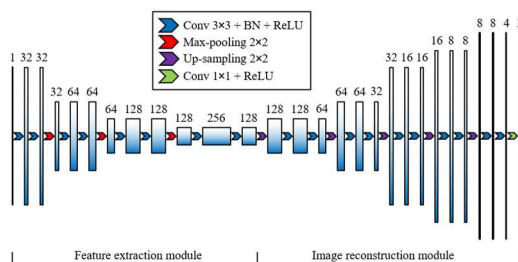
Figure 2: The architecture of DCNN

The loss function L is defined as:

$$L = L_{MSE} + \lambda R_{L1} \qquad (1)$$

where L_{MSE} is the mean-square error loss and R_{L1} is the l_1 norm regularization term; λ (i.e. 0.1) is the trade-off parameter among different loss terms. Adam is employed to optimize the DCNN using a batch size of 128 for 200 epochs and the learning rate is 0.0001. The final model is selected according to the minimum validation loss.

3   Results

Fig. 3 shows the reconstructed images of DCNN of six selected phantoms in the testing set when Gaussian noise of various levels (i.e. noise free, 50dB, 40dB and 30dB) is added to the EIM. The average Root Mean Square Error (RMSE) and Structural Similarity Index Measure (SSIM) of DCNN on the whole testing set are 0.0700 and 0.9472, respectively.
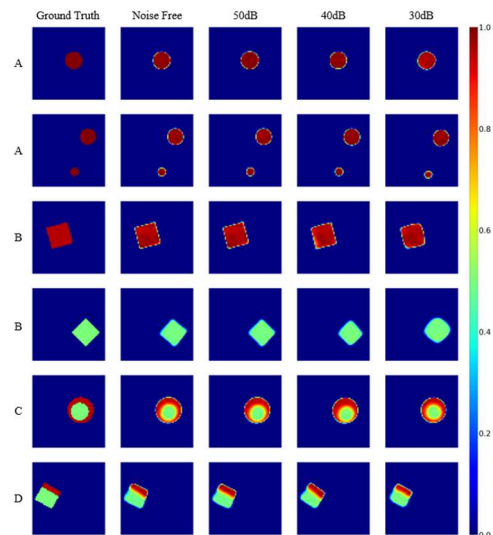
Figure 3: Selected reconstructed images from the testing set with different noise levels.

4   Conclusions

The results show that the proposed learning-based EIT image reconstruction method (DCNN with EIM) can reconstruct the simulated cancer invasion phantoms with high quality, and exhibits good anti-noise ability.

5   Acknowledgements

References

[1] TA Martin et al. *Metastatic Cancer Clinical Biological Perspectives*, p.135-168 Publishing: Landes Bioscience, 2013
[2] D Hu, K Lu, Y Yang *IEEE Int Conf Imag Sys Tech*, p.1-6, Abu Dhabi, United Arab Emirates, Dec 2019

Imaging Revision Total Hip Replacements by Electrical Impedance Tomography and Deep Learning based Reconstruction

Sascha Spors[1], Lisa Krukewitt[1,2], Simon Adrian[3], Daniel Klüß[4]

[1]Institute of Communications Engineering, University of Rostock, Germany. `Sascha.Spors@uni-rostock.de`
[2]Departement of Anestesiology and Intensive Care Medicine, University Medical Center Rostock, Germany.
[3]Institute of General Electrical Engineering, University of Rostock, Germany.
[4]Biomechanics and Implant Technology Research Laboratory, University Medical Center Rostock, Germany.

Abstract: Aseptic loosening is a frequent late complication in total hip arthoplasty. The standard diagnosis methods do not guarantee accurate detection of loosening. As the physiological and mechanical properties of bone are related to its impedance, recent progress in data-driven electrical impedance tomography may offer new diagnostic possibilities. This in-silico study examines this potential.

1 Introduction

A major reason for the revision of total hip replacements is the loosening of the hip-stem. However, the loosening is often detected too late due to the low sensitivity and specificity of current diagnostic methods [1]. The osseointegration of the hip-stem, as well as the health of the periprostetic bone are clinically relevant for the structural health of the implant system. Different tissues and also bone in different states show specific impedances that can be used to gain diagnostic insight. So far, electrical impedance tomography (EIT) has not been used extensively for imaging of bones. In part this is due to the challenges when aiming at absolute EIT (a-EIT) and the limited spatial resolution. However, recent progress in a-EIT facilitating deep learning techniques may offer new possibilities [2]. In this in-silico study we elaborate on the potential of a-EIT for the in-situ imaging of total hip replacements.

2 Method

Besides directly solving the inverse problem with deep neural networks, these are also used as pre- or post-processors in conjunction with traditional model-based algorithms. We focus on the latter approach as it already has shown good results [2]. More specifically, we post-processed the results from model-based reconstruction using a Gauss-Newton (GN) algorithm by a neural network. Deep convolutional autoencoders have shown good performance in inverse problems of medical imaging [3]. The structure of an autoencoder network features two major parts: (i) an encoder which learns an abstract representation (latent space) of the GN reconstruction and (ii) a decoder which generates a reconstruction from the abstract representation. The implemented autoencoder consists in total of four layers with skip connections. Each layer in the encoding/decoding branch contains a convolutional layer and a subsequent strided/transposed strided convolutional layer for downsampling/upsampling. The resulting latent space is 32 dimensional. In order to train the network, the 16-electrode GN reconstruction of a simplified upper tight, with femur and implant was simulated using the Python package `pyeit` [4]. For this purpose the femur was randomly placed within the upper tight and the conductivity of the femur/implant was varied around base values. Ad-

ditionally, normal distributed noise at four different signal-to-noise levels SNR $= \{30, 40, 50, \infty\}$ dB was added to the electrode signals. This resulted in a database of 10.000 representative samples, where 90% of these where used for training of the network and 10% for validation. Hyperparameter optimization was performed by the Random Search technique, resulting in a mean-squared error (MSE) of $1.8 \cdot 10^{-3}$ for the final model.

3 Results and Conclusions

Figure 1 shows the reconstruction results for two exemplary samples which have not been used for training/validation. The traditional GN reconstruction is shown on the left, the proposed post-processing by the implemented deep autoencoder on the right. The upper/lower row show results for a SNR of 40 and 20 dB, respectively. The low spatial resolution of the GN reconstruction is a consequence of the regularization coping for the ill-conditioning of the inverse problem. The proposed post-processing improves the resolution and robustness of the reconstruction considerably.
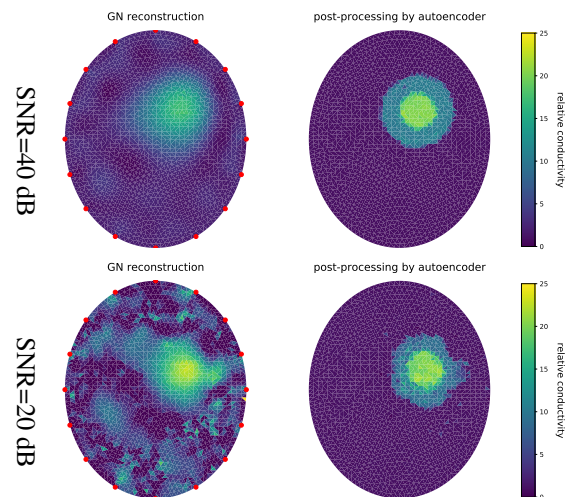
Figure 1: Exemplary reconstruction results for unseen samples.

References

[1] C. Ruther, C. Schulze, A. Böhme, H. Nierath, H. Ewald, W. Mittelmeier, R. Bader, and D. Kluess, "Investigation of a passive sensor array for diagnosis of loosening of endoprosthetic implants," *Sensors*, vol. 13, pp. 1–20, 12 2012.

[2] S. J. Hamilton and A. Hauptmann, "Deep d-bar: Real-time electrical impedance tomography imaging with deep neural networks," *IEEE Trans. on Medical Imaging*, vol. 37, no. 10, pp. 2367–2377, 2018.

[3] A. Lucas, M. Iliadis, R. Molina, and A. K. Katsaggelos, "Using deep neural networks for inverse problems in imaging," *IEEE Signal Processing Magazine*, vol. 35, no. 1, pp. 20–36, 2018.

[4] B. Liu, B. Yang, C. Xu, J. Xia, M. Dai, Z. Ji, F. You, X. Dong, X. Shi, and F. Fu, "pyeit: A python based framework for electrical impedance tomography," *SoftwareX*, vol. 7, pp. 304–308, 2018.

Session 6: Hardware

Reducing the hardware requirements for fast neural EIT

Enrico Ravagli[1,*], Svetlana Mastitskaya[1], Kirill Aristovich[1], and David Holder[1]

[1]Dept. of Medical Physics and Biomedical Engineering, University College London

*e.ravagli@ucl.ac.uk

Abstract: The ScouseTom system enables fast neural EIT but includes bulky and expensive equipment. We aim to make this technique more accessible by replacing commercial devices with ad-hoc circuitry. Preliminary results indicate new circuitry grants a large reduction in size and cost without a drop in image quality.

1 Introduction

Fast neural EIT can be used to image functional activity in brain or nerve. In peripheral nerves, evoked action potentials propagating along nerve fibre bundles are imaged with a cuff-like array of electrodes placed around the nerve [1-3]. The state-of-the-art solution for fast neural EIT is the ScouseTom system [4] due to its high resolution (24 bit, 100 kHz). However, the presence of bulky and expensive commercial benchtop instruments (EEG amplifier, current sources) in this system limits the adoption of EIT by the neurophysiology community. With this work, we aim to simplify hardware requirements for fast neural EIT by replacing the commercial benchtop current sources with two compact and low-cost custom circuits of equal performance.

2 Methods

2.1 Circuit Design

Fast neural EIT requires one sinusoidal current source for EIT measurements and one current pulse generator for evoking neural activity. Custom circuits (Figure 1) were designed to replace the ScouseTom current sources (Keithley-6221, Tektronix, UK). Both devices are powered by generic Lithium-Polymer 3.7V batteries and use Arduino-based microcontrollers for digital control.
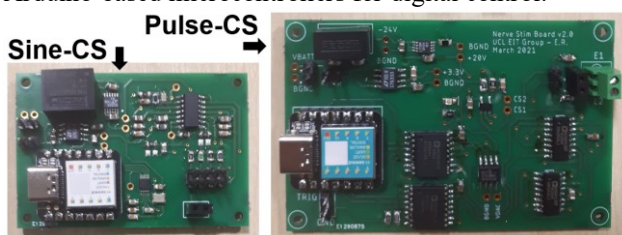
Figure 1: New current sources for EIT carrier generation and neural tissue stimulation.

The EIT sine wave current source (Sine-CS) was implemented by coupling a Discrete Digital Synthesis chip to a buffered Enhanced Howland Current Source. The current pulse generator (Pulse-CS) was implemented by coupling a Digital-to-Analog Converter to a non-inverting amplifier, similarly to [5]. Keithley-6221 current sources used in the ScouseTom setup are 104×238×370mm in size, with a price of ≈£8000 each, and fast neural EIT requires two of them. Dimensions of the developed boards are respectively ≈40×60mm for Sine-CS and ≈50×78mm for Pulse-CS. Both boards can be manufactured at a price of approximately £100 in total.

2.2 Preliminary and *In Vivo* Testing

Testing in this phase was focused toward nerve EIT parameters. Sine-CS was tested by delivering typical nerve EIT current amplitudes (30-240µA) to realistic resistor loads of 470Ω, 1.5KΩ, and 2.2KΩ. Noise in the nerve EIT bandwidth of 6±1KHz was compared between the Keithley and Sine-CS source in a tank experiment with realistic conductivity of 0.3S/m. Pulse-CS was assessed by delivering pulses with different amplitudes (250µA-5mA) and pulse widths (50µs-2ms) over the same resistive loads. A nerve EIT experiment was performed as in [1-3], in which EIT was performed with both Keithley and Sine-CS devices, keeping the rest of the system unchanged.

3 Results

Sine-CS current amplitude showed a correlation of $R^2>0.99$ and an error of -2.0±1.4µA compared to nominal values. Average noise levels were found to be 1.68±0.02µV and 1.61±0.01µV respectively for the Keithley and Sine-CS devices. For the Pulse-CS circuit, pulse current amplitude showed a correlation of $R^2>0.99$ and an error of -13.5±35.4µA compared to nominal values. Width of current pulses had an error of -4±12µs compared to nominal values. Impedance changes in response to evoked activity were detected with both commercial and Sine-CS device. Image reconstruction at peak impedance change, shown in Figure 2, is co-localized in the same region of the cross-section of the nerve for both current sources.
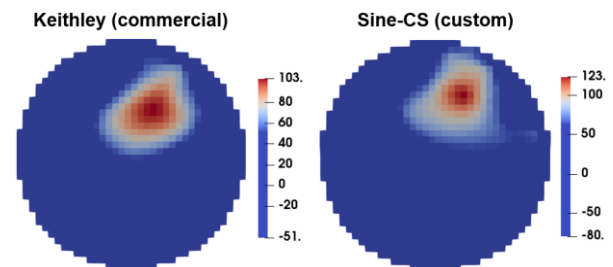
Figure 2: Nerve conductivity changes at peak depolarization for commercial (left) and custom (right) EIT current sources.

4 Conclusions

Preliminary results suggest that the developed circuitry can replace commercial current sources for fast EIT, while being significantly cheaper and more compact. Work in progress: expansion of *in vivo* testing to include assessment of the pulse generation circuit; design and implement an open-source EEG amplifier with matching parameters.

References

[1] K Aristovich et al. *J Neural Eng* 15:056025 (2018).
[2] E Ravagli et al. *Physiol Meas* 4:115007 (2019).
[3] E Ravagli et al. *Nat Commun* 11:6241 (2020).
[4] J Avery et al. *Sensors* 17:280 (2017).
[5] V Sivaji et al. *J Neurosci Methods* 320:26-36 (2019)

Design, Manufacturing and Testing of a Cuff Electrode Array for EIT and Vagus Nerve Stimulation

Florencia Maurino Alperovich[1], Adam Fitchett[1] and Kirill Aristovich[1]

[1]Medical Physics & Biomedical Engineering, University College London, florencia.alperovich.17@ucl.ac.uk

Abstract: Cuff electrode arrays for VNS can often lead to nerve damage. A 'belt-buckle' concept for rat and pig cuffs using PDMS and stainless-steel foil was manufactured and tested to ensure no unsafe forces on the nerve. The cuffs have potential for scalability to human VN due to its resemblance in size to pig VN.

1   Introduction

Cuff electrode arrays currently used for peripheral nerve stimulation (PNS) and recording have several limitations. Some of the most commonly used designs are known to lead to nerve damage in long-term use [1], either due to a mechanical mismatch between the nerve and the cuff, or due to the cuff not allowing for any expansion of the nerve with post-implantation swelling [2]. Additionally, some designs do not allow for selective stimulation, key for avoiding side-effects of treatment with PNS [3].

The aim of this project was to develop a cuff electrode array suitable for EIT and selective VNS, which must be easily manufacturable, conform to the nerve shape, and not cause nerve damage.

2   Methods

2.1   Cuff design and manufacturing

The project used an iterative approach via which several designs were manufactured and tested, inspiring the following iteration of designs.

The design studied consists of a 'belt-buckle' concept (fig. 1), in which the cuff contains a narrow strip of material at the top which fits through a slit in the main body of the cuff, and locks in place via one of various locking mechanisms. The cuffs were manufactured following previously described methods [4].

Figure 1: 3D model of 'belt-buckle' cuff wrapped around nerve.

2.2   Rat cuffs

The rat cuffs were used as a proof-of-concept of the belt-buckle design. Multiple iterations were manufactured in order to optimise the designs as well as the manufacturing method. The cuffs were tested to determine the efficacy of the different locking mechanisms by attaching a weight to the cuff until it opened.

2.3   Pig cuffs

The pig cuffs were designed based on the most successful rat cuff designs, and modified based on the larger size of the pig vagus nerve (VN).

A simplified model of these cuffs (containing only PDMS with no reinforcement materials) was then tested via FEA in order to ensure the cuffs do not subject the nerve to forces above a predetermined safe threshold.

Some preliminary in vivo testing was also carried out to determine the efficiency of the locking mechanism during stimulation.

3   Results

The most effective locking mechanism (fig. 2) was found throughout the iterative process and proven to stay locked in place up to safe threshold forces.
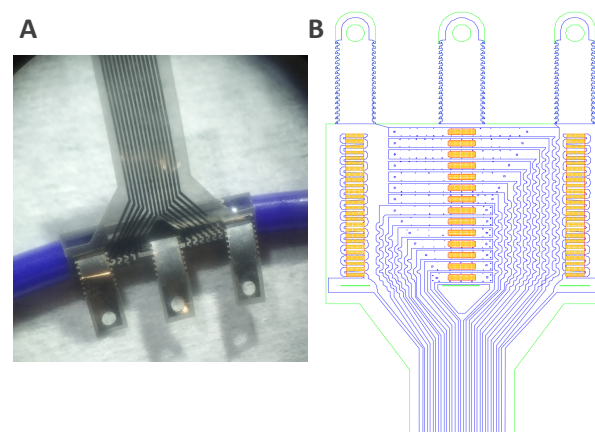
Figure 2: A) EIT pig cuff design wrapped around a 3mm diameter wire. B) Schematic drawing of the cuff; PDMS in green, stainless-steel in blue, and electrode contacts in yellow.

4   Conclusions

These cuffs have great potential to enable VNS and EIT while ensuring the nerve is not subjected to unsafe forces. The size of the pig VN (diameter ~ 3 mm) makes this cuff easily scalable to human VN (diameter ~ 4.5 mm) with some optimisation. Further work is necessary to optimise the designs and to obtain more representative data of the forces withstood by the cuffs.

References

[1] G.C. McConnell *et al*., *J Neural Eng*., 6(5):56003, 2009.
[2] F.A. Cuoco and D. M. Durand, *IEEE Trans Rehabil Eng*, 8(1):35-41, 2000.
[3] C. M. Noller *et al*., *Front Neurosci*, 13:911, 2019.
[4] C. A. Chapman *et al*., *J Neural Eng*., 16(1):016001, 2019.

A Miniaturized Active Electrode Analog Front End for Impedance-Based Surgical Margin Assessment in Minimally Invasive Surgeries

Allaire Doussan[1] and Ryan Halter[1,2]

[1]Thayer School of Engineering, Dartmouth College, Hanover, NH, USA, allaire.f.doussan.th@dartmouth.edu
[2]Geisel School of Medicine, Dartmouth College, Hanover, NH, USA

Abstract: This work describes a miniaturized 29-channel (4 current source/sink & 25 voltage pick-up) electrical impedance tomography (EIT) system analog front end (AFE) for use in laparoscopic surgical margin assessment. Frequency response analysis show a flat bandwidth out to 100 kHz for loads up to 5kΩ.

1 Introduction

Positive surgical margins (PSM) are a significant negative outcome following cancer surgeries as they often require patients to undergo additional noxious therapies to eradicate the remaining cancer cells [1]. The current standard of care for detecting PSMs is post-operative microscopic assessment of the tissue. Assessing surgical margin status in real-time with EIT has the potential to reduce the occurrence of PSMs and the associated noxious therapies. We propose a novel miniaturized active electrode EIT AFE with electrodes specialized for current injection and voltage pick-up. The AFE and electrodes will be located at the end of a flexible endoscopic instrument and serve to minimize effects of long cable lengths.

2 Methods

2.1 Hardware Design

The AFE receives a sinusoidal voltage waveform from an off-board digital-to-analog converter (DAC) that is input into a Howland-based voltage-controlled current source (VCCS) to produce a constant current. The injected current is measured across a sense resistor (R_{sense}) with an instrumentation amplifier and multiplexed to 1 of 4 current injection electrodes. Each of the 25 voltage measurement channels have a unity-gain amplifier close to (<4cm) the electrodes to reduce the effect of noise as the signal travels (~1m) from the endoscopic probe to the data acquisition hardware. Figure 1 shows a block diagram of a single channel with Z_{load13} representing the load between electrodes I1 and I3 and V# representing one of the 25 single-ended voltage pick-up electrodes. All AFE circuitry fit onto 2 printed circuit boards measuring 7.25mm by 40mm (Figure 2). Previous versions of this work did not include an active electrode design [2].
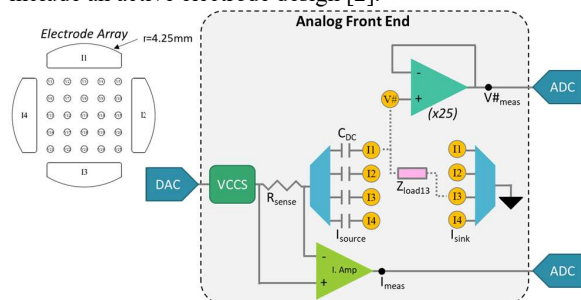
Figure 1: Electrode array and block diagram of AFE circuitry.
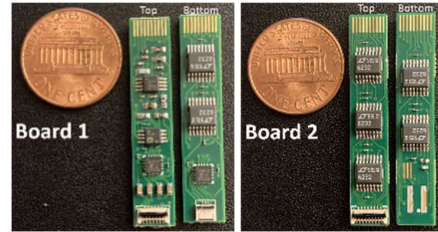
Figure 2: AFE printed circuit boards (7.25 mm x 40 mm).

2.2 Performance Evaluation and Validation

The frequency response for the AFE was evaluated from 100 Hz to 10 MHz using a combination of NI Hardware (NI USB-6259) and an oscilloscope (DSOX1204G) for resistive loads ranging from 100 Ω to 5k Ω along with 2 parallel RC loads (100 Ω ‖ 1 nF & 1k Ω ‖ 100 pF).

3 Conclusions
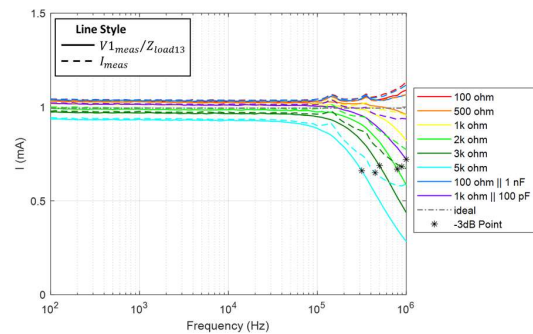
Figure 3: Frequency response analysis of injected current measured from the instrumentation amplifier (I_{meas}) and the current through the load (V_{meas} / Z_{load}) using I1 and I3 as the current source and sink electrodes, respectively, and V1 as a single-ended voltage electrode.

Discrete load testing shows a flat frequency bandwidth up to 100 kHz (Figure 3). Since the injected current is measured for each case, there is potential to extend the bandwidth up to 1 MHz. This can be done by calculating the calibration factors and adjusting the amplitude of the input voltage waveform to account for the known drop in the injected current, similar to our previous work [3].

4 Acknowledgements

References

[1] Orosco R, et al. *Sci. Rep.*, 8:5686, 2018
[2] Mahara A, Khan S, Murphy E, Schned A, Hyams E, Halter R. *IEEE Trans Med Imaging, 34:150*, 2005
[3] Khan S, Manwaring P, Borsic A, Halter R. *IEEE Trans Med Imaging,* 34:888-901, 2015

ACT5 EIT System

Omid Rajabi Shishvan[1], Ahmed Abdelwahab[1], Gary J. Saulnier[1]

[1]Electrical & Computer Engineering Department, University at Albany, State University of New York
orajabishishvan@albany.edu

Abstract: This paper introduces ACT5, a new multiple-source EIT system for medical applications. ACT5 is able to deploy variable number of electrodes, where each source has an operation frequency range of 30 kHz to 1 MHz, achieving a voltage measurement SNR of 96 dB.

1   Introduction

Adaptive Current Tomograph 5 (ACT5) is a multiple-source applied current EIT system that is designed in a modular fashion that allows it to utilize arbitrary number of electrodes up to a maximum of 48. The target application of ACT5 is thorax imaging where it can take 30 frames of images per second under the 32-electrode configuration. ACT5 utilizes a novel shunt impedance measurement technique that continuously monitors the parallel impedance values so that its adaptive current sources can accurately compensate for the current shunted to ground.

2   Methods

ACT5 hardware consists of a controller board, a calibration board, and multiple current source boards. The controller board is connected to a PC through a serial communication link, where it receives the necessary information from the PC and transmits back the collected data. The controller board is connected to the other boards through a VME backplane where it transfers data back and forth via links using the serial peripherial interface (SPI) protocol.

Each current source board consists of 4 adaptive current sources [1, 2] with 5 cable connectors where 4 of the connectors are used to connect to electrodes via 2 meter double-shielded cables and the fifth connector connects the analog side of the sources to the calibration system. The current sources, paired with voltmeters, can operate in the frequency range of 30 kHz to 1 MHz, applying maximum current of 1 mA peak-to-peak and reading voltages of up to 1 V peak-to-peak. Using Xilinx Artix 7 FPGA as a DDS combined with a 16-bit DAC, an 18-bit ADC, and 0.1% precision resistors, these sources achieve a signal-to-noise ratio of 96 dB under their maximum swing.

The current sources can adaptively adjust their output current based on their voltage measurements so that they negate the effects of the shunt impedance on the electrodes. The adaptive sources need the values of the shunt impedance to work correctly and ACT5 deploys a novel impedance measurement technique [3] that can update the shunt impedance values while collecting image data. This operation requires the use of one additional orthogonal current pattern supplementing those required for imaging. Alternately, ACT5 can measure the shunt impedance by applying a small current to an open-circuit configuration.

The ACT5 sources and voltmeters do not need any analog adjustments. Current source boards can be plugged into the backplane and then calibrated with reference to the calibration board and they can be used immediately after the calibration process. The hardware of ACT5 is shown in fig. 1. Boards are plugged into the backplane which is assembled on a subrack. The subrack in addition to the power supply are enclosed in a box with temperature-sensitive fans. The final piece is the computer that provides the interface for the users to interact with the ACT5 system.
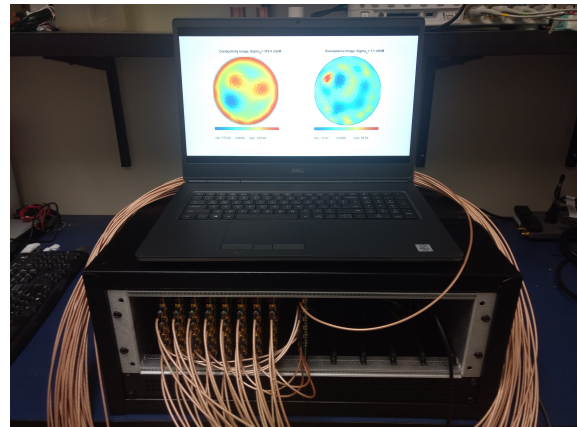
Figure 1: ACT5 Hardware

Other planned features of ACT5 include extraction of ECG signal off the existing electrodes, monitoring the electrode contact impedance, and adaptive change of current patterns that enables using optimal patterns for best quality of images. ACT5 also has safety features implemented both in the hardware and the software, including monitoring of voltages on electrodes to detect shorts and electrode disconnects, and monitoring the current on the extra ground electrode on a broad range of frequencies to detect faults in the system. Depending on the severity of the fault, ACT5 can alert the users, shut down the sources, or completely disconnect the power supply.

3   Conclusions

The ACT5 system, a multiple-source EIT device, is introduced and its features are explained broadly. ACT5 uses multiple novel ideas to accurately apply desired current from all sources and has flexible design that makes it suitable to be used under various configurations.

4   Acknowledgements

References

[1] G J Saulnier, A Abdelwahab, F Maysha *Conf 20th EIT*, p.46, London, UK, Jul 2019

[2] G J Saulnier, A Abdelwahab, O Rajabi Shishvan *Physiol. Meas*, **41** 064002, 2020

[3] O Rajabi Shishvan, A Abdelwahab, G J Saulnier *Conf 42nd EMBC*, p.1452-1456, Montreal, Canada, Jul 2020

Passive sensing of thermal changes using a fabric sensor with EIT

Ahmed Abdulsalam, Georgios Panagi, Kahtan Mezher, Georgios Fotopoulos, Panos Liatsis

Department of Electrical Engineering and Computer Science, Khalifa University, Abu Dhabi, `panayig@gmail.com`

Abstract: EIT has been proposed for touch, position-strain and thermal sensing for robotic applications with the use of stretchable fabric sensors. An EIT system equipped with a fabric sensor was used to detect thermal changes and the results showed that it detected a stimulus of 65.4°C at ambient temperature of 20.2°C.

1 Introduction

Stretchable tactile layers resembling the human skin have been proposed as the means to provide robots the capability to operate in unstructured environments. They are envisioned to serve as a cover for the robot's mechanical and electrical parts and as a sensor for sensing functions such as touch, position-strain and thermal sensing. [1]

A robot's thermal sensing function helps it to recognise an external thermal change when in contact with an object. It can be pathetic, i.e., recognising the thermal state of the object or active, i.e., measuring the heat flow between the robot's skin and the object. The proposed pathetic thermal sensing function techniques involve thermistors or thermocouples embedded in tactile sensors however their implementation can be complex. [2][3]

EIT has been investigated for touch and position-strain with stretchable fabric sensors [4] and for sensing thermal changes for hyperthermia in the clinical setting [5]. In this paper we present an investigation on the use of EIT for passive sensing of thermal changes using a fabric sensor.

2 Methods

A single frequency 16 channel EIT system was developed. The multiplexer section comprised four ADG1606 multiplexers. The analog signal processing comprised an INA828 as a pre-amp followed by three LM7171 for the amplification and bandpass filtering and an LTC2308 ADC for the digitization. An Improved Howland current pump based on the THS4603 FET opamp was used. A Cyclone V FPGA controlled the multiplexers to implement the drive pattern and processed the recordings. The EIDORS toolkit was used for the image reconstruction.

The conductive fabric Silitex P130 (40 cm x 40 cm x 0,65 mm) was used as the sensor and was placed securely between two Perspex sheets (40 cm x 40 cm x 1 cm). The top Perspex sheet had a 30 cm diameter circular opening to allow free access to the fabric sensor. Sixteen copper electrodes (1 cm x 2 cm) were equidistantly placed on the opening's boundary in contact with the conductive fabric and were connected to the EIT system with SMA cables.

An aluminium cup filled with 15 mL of water at a temperature of 20.8°C was placed on the sensor opposite electrode 1 for two minutes and was then removed. The sensor was left empty for 15 minutes and then an aluminium cup filled with 15 mL of water at a temperature of 65.4°C was placed on the fabric opposite electrode 1 for two minutes and was then removed. The average ambient temperature during the measurement was 20.2°C. The EIT system took a recording every 10 seconds without user intervention for the whole period of the experiment and a thermal imaging camera took an image every 30 seconds. The EIT system's operating frequency was 10 kHz and the injected sinusoidal current was 5 mA RMS.
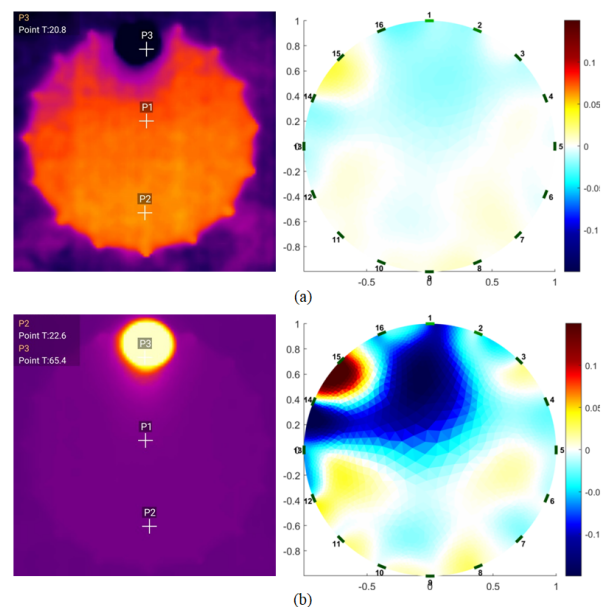
Figure 1: Thermal images and the corresponding EIT reconstructed images when the water temperature in the aluminum cup placed on the fabric was (a) 20.8°C and (b) 65.4°C.

3 Results and Discussion

Figure 1 shows the thermal images of the placed aluminium cup on the sensor and the corresponding EIT reconstructed images when the water temperature was 20.8°C and 65.4°C respectively. The resultant reconstructed EIT images shows that the EIT system detected the thermal change caused by the 65.4°C stimulus however it didn't detect the 20.8°C stimulus.

4 Conclusion and Recommendation

The proposed EIT system-sensor configuration can detect a thermal change caused by a stimulus much hotter than the ambient temperature but it cannot detect a thermal change caused by a stimulus very close to the ambient temperature. Further work is required to increase the capability of the configuration to detect smaller thermal changes.

References

[1] D. Silvera-Tawil, D. Rye, and M. Velonaki, *Rob. Auton. Syst.,* vol. 63, no. P3, pp. 230–243, 2015.

[2] G. J. Monkman and P. M. Taylor, *IEEE Trans. Robot. Autom.,* vol. 9, no. 3, pp. 313–318, 1993.

[3] Q. Li, L. N. Zhang, X. M. Tao, and X. Ding, *Adv. Healthc. Mater.,* vol. 6, no. 12, pp. 1–23, 2017.

[4] D. Silvera-Tawil, D. Rye, M. Soleimani, and M. Velonaki, *IEEE Sens. J., vol. 15,* no. 4, pp. 2001–2016, 2015.

[5] K. D. Paulsen, M. J. Moskowitz, T. P. Ryan, S. E. Mitchell, and P. J. Hoopes, *Int. J. Hyperth., vol. 12,* no. 5, pp. 573–591, 1996.

Evaluation of 3D Thoracic Equivalent Circuit Models using Co-simulation with EIT Hardware

Christos Dimas[1], Vassilis Alimisis[2], Nikolaos Uzunoglu[3], Paul P. Sotiriadis[4]

[1-4]Dept. of Electrical and Computer Engineering, National Technical University of Athens, Greece
[1]chdim@central.ntua.gr
[4]pps@ieee.org

Abstract: An extensive EIT hardware simulation approach, merging parametric EIT circuit setups and 3D thoracic tissue models is described. It can used as an effective tool for EIT-thoracic imaging applications prior to implementation.

1 Introduction

Evaluation of EIT hardware circuitry is usually performed over saline-content phantom tanks or resistor meshes. Furthermore, EIT hardware design and implementation process for specific medical applications, is commonly based on specifications defined by previous literature observations or electric field-nature simulations that do not include hardware. However, it is hard to simulate both EIT hardware and the Subject Under Test (SUT). We propose a fastidious simulation approach combining EIT hardware configuration and thoracic SUT, in an effort to predict certain hardware configuration's performance in relative applications.

2 Methods

The proposed approach makes use of a database which includes the dielectric properties of numerous body tissues over a wide frequency span [1], as well as a recent update in EIDORS [2] which allows the transform of a F.E.M. structure to a N-electrode port RLC circuit.

A fine-meshed $3D$ thoracic F.E.M. structure is firstly created with the NETGEN tool, which can be based on CT images. Then a specific measuring frequency is selected and a Python script exctracts the present tissue's dielectric properties for this frequency, transfering them in MATLAB. The corresponding conductivity σ and permittivity ϵ values are then assigned to the F.E.M. structure, which is then transformed to a N-port RLC. This is merged with the EIT ciruitry in SPICE, where transient simulations take place. The outputs are written on a PWL file and sent to MATLAB for digital processing. The ADC, DAC and demodulation functionality is also simulated. Finally the EIDORS tool takes the demodulated data to produce the EIT images. The whole process is presented in Fig. 1.

It is important to note that following this approach, any hardware noise or error's effect in both the signal and the image can be directly observed by introducing it in the simulated hardware (e.g. white noise, electrode disconnections, VCCS missmatches, channel imbalances combined with low instrumentation CMRR, e.t.c.). Furthermore, the impact of alternative topologies or digital signal processing approaches on the image can also be simulated.

3 Results

Results for 2 selected configurations, for $I = 1.2mA_{p-p}$ when total white noise is $6mV_{p-p}$ are presented in Fig. 1. Direct G-N approach with NOSER prior has been used.
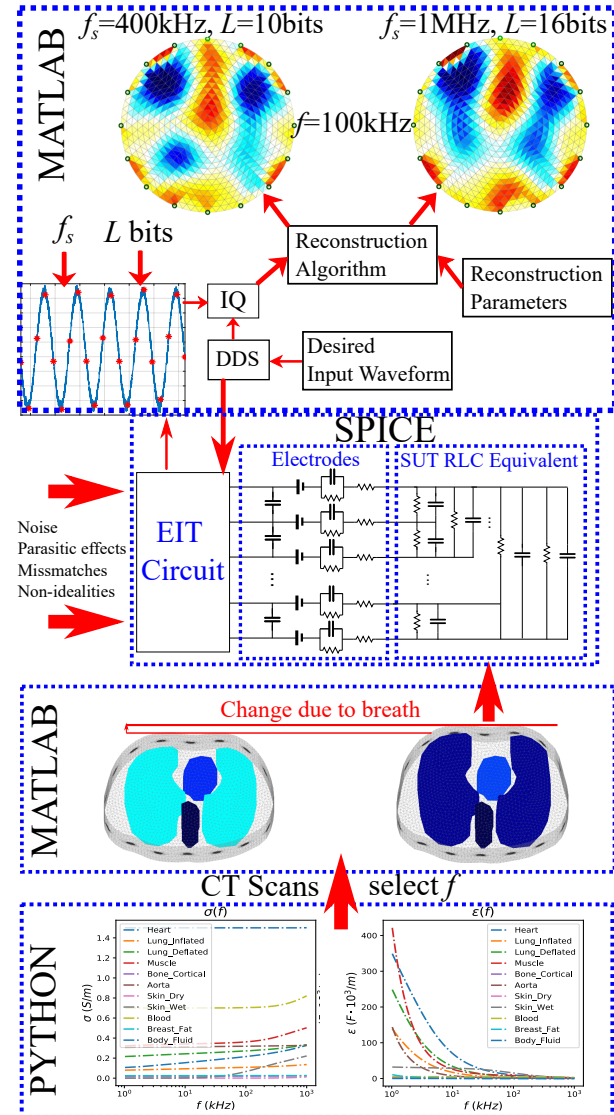
Figure 1: Brief schematic of the proposed simulation approach. Code and models are available online in Github

4 Conclusions

An extensive simulation approach which combines EIT hardware, the SUT, the digital signal processing and the reconstruction has been presented. An application in EIT lung imaging is demonstrated.

References

[1] S Gabriel, R Lau, C Gabriel. The dielectric properties of biological tissues: II. Meas. in the freq. range 10 Hz to 20 GHz. *Physics in medicine & biology* **1996** *41*, 11, 2251

[2] Boyle A, Adler A. Integrating Circuit Simulation with EIT FEM Models. *19th Int. Conf. of Biom. Applications of EIT* **2018**

Flexible and Scalable Multifrequency EIT System

Marcin J. Kraśny[1,2], Katarzyna Polak-Kraśna[3], Cathal Keane[1], Shauna Burke[1], James Blackwell[1,4], Niall Colgan[1]

[1]Advanced Biological Imaging Laboratory, School of Physics, NUIG, m.j.krasny@nuigalway.ie, [2]Smart Sensors Lab, School of Medicine, NUIG, [3]Biomedical Engineering, NUIG, [4]School of Mathematics, Statistics and Applied Mathematics, NUIG

Abstract: The lack of easily accessible, affordable tools for the rapid development and testing of EIT systems, limits the expansion of the technology to new fields and applications. We propose a simple solution for testing, validation, and optimisation of features such as electrode configuration, test signal, and image reconstruction algorithms.

1   Introduction

Electrical Impedance Tomography (EIT) is a non-invasive spectroscopy imaging method employing impedance measurement. It is used e.g. in tumour detection [1], lung function monitoring [2] and urinary incontinence control [3] with potential industrial applications such as liquids or gas flow [4] and structural monitoring [5].

Commercially available EIT devices are either expensive [6,7] or require an advanced electronics skillset and additional equipment to assemble an experimental setup [8]. The only affordable device [9] has multiple limitations including a fixed electrode configuration and signal frequency. There is a need to provide an easy way of testing new algorithms and implementing EIT for optimised and new solutions.

2   Methods

2.1   Hardware setup

Here we present a combination of standard laboratory instrument; LCR meter with open hardware evaluation boards which were implemented on a prototype board controlled by an Arduino Uno board (Fig. 1). We achieved a fully functioning multifrequency EIT device without the need for advanced hardware design and assembly skills.

Figure 1: Fully functioning multifrequency EIT device consisting of LCR meter (top), phantom container (left), hardware evaluation boards and Arduino Uno (right).

Validation of the system was performed using a phantom container, with 16 circularly attached measuring electrodes, filled with 0.4 wt% saline solution. The LCR meter provided accurate impedance measurement. Each of four LCR meter terminals were connected to a separate multiplexer [10]. The multiplexers were controlled via shift registers [10] acting as port expanders to the Arduino. The multiplexers enabled direct connection of the LCR terminals to electrodes (number adjustable between 2 and 16 with a potential for further expansion).

2.2   System Control and Image Reconstruction

A Python script was developed to control the multiplexers via the Arduino board and the LCR meter connected to a PC. The user can control measurement parameters i.e. the electrode count in the experiment and their configuration (adjacent, opposite, etc.), excitation signal amplitude and frequency, and select an algorithm for image reconstruction. By default, reconstruction utilises the pyEIT [11] library but results can also be transferred and processed using the EIDORS (MATLAB) library [12]. Validation parameters; electrode current: opposite, voltage measurement: adjacent, amplitude: 0.5 V_{RMS}, frequency: 100 kHz, pyEIT reconstruction algorithm: Gauss-Newton.

3   Results

To demonstrate the capabilities of the proposed EIT setup, we placed an object inside the phantom container, performed impedance measurements resulting in a map of 192 results and obtained an accurate reconstructed image (Fig. 2). The combined measurement and reconstruction time was below 4 seconds.
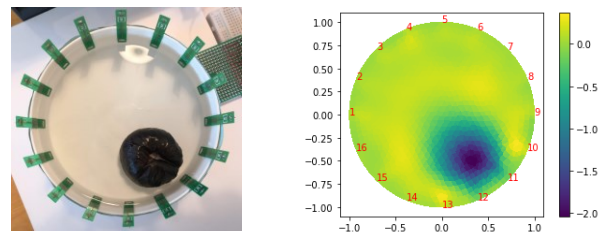
Figure 2: A plum placed in the phantom container (left) and its reconstructed image (right).

4   Conclusions

To overcome the high entry threshold to implementing EIT methods in widespread applications, a simple, yet fully functioning, flexible and scalable multifrequency EIT system was developed. It can be built from standard components without the need for electronics hardware development and assembly. We believe this tool will broaden the applications of EIT, facilitate its optimisation and development of reconstruction algorithms.

References

[1] V. G. Sirtoli, et al., DOI: 10.1109/EMBC.2017.8036786
[2] I. Frerichs, et al., DOI: 10.1136/thoraxjnl-2016-208357
[3] E. Dunne, et al., DOI: 10.1088/1361-6579/aae6ed
[4] M. S. Mat-Shayuti, et al., DOI: 10.18178/ijeetc.8.2.119-126
[5] B. Suryanto, et al., DOI: 10.1007/s12572-017-0190-9
[6] Maltron Sheffield MK 3.5, https://maltronint.com
[7] SenTec EIT Pioneer Set, https://www.sentec.com
[8] J. Avery, et al., DOI: 10.3390/s17020280
[9] Spectra EIT Kit, https://mindseyebiomedical.com
[10] SparkFun, BOB-09056 & BOB-10680
[11] B. Liu et al., DOI: 10.1016/j.softx.2018.09.005
[12] A. Adler, et al., DOI: 10.1088/0967-3334/27/5/S03

Influence of skin surface charge/discharge effects in real EIT systems

Timur Tuykin, Pavel Kobrisev, Alexander Korjenevsky, Sergej Sapetsky[1]

[1]Electromagnetic tomography group, Kotelnikov Institute of Radioengineering and Electronics (IRE) of Russian Academy of Sciences, tt@cplire.ru

Abstract: Human skin has high DC impedance that causes some processes with significant influence on imaging. The influence is non-significant for water phantom. We have studied the processes on skin and methods to reduce their impact. One of them is data set transposition and it can improve imaging.

1 Introduction - motivation

While improving the EIT system with 256 electrodes developed earlier [1] we faced with image artefacts caused by such processes. There are two groups of processes: slow skin charge/discharge and stray capacitance.

2 Slow skin charge/discharge

Electrodes contacted with skin have significant capacitance (units-hundreds nF) and work like array of capacitors with one plate under skin and other on skin surface. Under skin plates have close potentials because of high tissue conductivity in contrast to low skin conductivity. Their can be considered as connected together (see fig. 1). Plates on skin surface have much different potentials, current leakage on neighbour electrodes (on skin surface) and self-discharge (through skin). During work AC current generator charge skin surface by DC voltage. For non-continuous mode, receivers and channel multiplexing AC current generator, this DC voltage changes have durations corresponding to measuring time and can cause sufficient influence on the measuring process. It depends on:

- Condition of contact of electrodes with skin.
- Generator and receiver powering durations, switching order, pauses between pulses train and cycles.

Also, we should pay attention to:

- Multiplexer charge injection during switching
- Difference of electrodes galvanic potentials (up to +-100 mV for the same material plates)

Current generator can have additional reaction on voltage of charged skin after channel switching.

3 Stray capacitances are everywhere

Measurement by real device cannot be as good as modelled one because of stray capacitances: generator shunt, object leakage and generator to receiver cross talks.

Stray capacitance limits generator quality, acts like its internal resistance. 20 pF stray capacitance is very good value and corresponds to impedance 318 kOhms on 50 kHz frequency. Multiplexers add extra 100 pF to generator capacitance. It has impedance 31 kOhms for 50 kHz. Human body impedance is around 10 kOhms in our electrodes systems.

As for the object, then stray capacitances of turned off channels produce leakage and deteriorate 4-points measurement $Z_{leak} = (Z_{stray} + Z_{skin})/N_{channels}$.

Variation of stray capacitances and charge/discharge process gives the same images/values on water phantom and can gives different ones on human body.
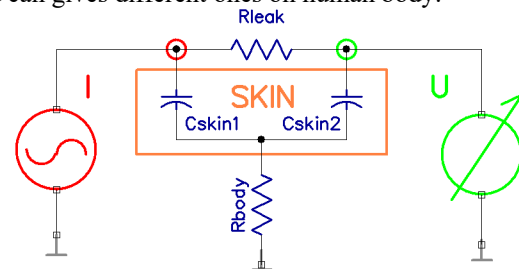
Figure 1: receiver potential variation with skin leakage.

4 Hardware improvement

Decreasing level of DC voltage on skin can decrease slow charge/discharge processes and their influence on measurement. On way of improvement is to change pulse train form add pre- and post-pulse for each generator train pulse to decrease level of skin charge DC after generation. Pre- and post-impulse should be ½ period of ½ amplitude or ½ period pulse 2 times faster. According to practice DC compensation pre-pulse should be bigger because of skin charge during pre-pulse. DC cannot be eliminating after pulse train for all electrodes because it depends from contact conditions with skin for each electrode.

Switching generator after non-stop, continuous work produce more quasi-stable DC distribution over skin and image have no artefacts, but voltage values changes.

For generation-measuring order better to switch all generators for one receiver then all receivers for one generator. It provides more equal DC level over skin surface and less influence.

5 Data set transposition

Transposition of data set (changes row and column in data set matrix) can help to decrease influence of skin and fix other local perturbation like noise, small movement artefacts. Data set should have diagonal symmetry due to Lorentz reciprocity lemma. Investigated data set diagonal symmetry is good for data quality analysis.

6 Acknowledgements

References

[1] V. Cherepenin, A. Karpov, A. Korjenevsky, V. Kornienko, Y. Kultiasov, M. Ochapkin, O. Trochanova and D. Meister, "Three-dimensional EIT imaging of breast tissues: system design and clinical testing", *IEEE Trans. Medical Imaging*, v. 21(6), pp 662-667, 2002

Session 7: Thorax III

Cardiopulmonary Monitoring of Tidal Volume and Stroke Volume using EIT: An Animal Study

Tong In Oh,[1] Geuk Young Jang,[1] Chi Ryang Chung,[2] Ryoung Eun Ko,[2] Jin Young Lee,[2] Gee Young Suh,[2] Yongmin Kim[3] and Eung Je Woo[1]

[1]Department of Biomedical Engineering, College of Medicine, Kyung Hee University, Seoul, Korea, tioh@khu.ac.kr
[2]Department of Critical Care Medicine, Samsung Medical Center, Sungkyunkwan University School of Medicine, Seoul, Korea
[3]Department of Creative IT Engineering, POSTECH, Pohang, Korea

Abstract: Cardiopulmonary monitoring of breath-by-breath tidal volume (TV) and beat-to-beat stroke volume (SV) was performed on six pigs using an EIT device with a high temporal resolution during normal and reduced ventilation to present the feasibility of clinical uses.

1   Introduction

Electrical impedance tomography (EIT) has been used for regional lung ventilation imaging during mechanical ventilation for lung-protective ventilation. In this case, the measured data includes cardiogenic information even though it was weaker than the respiratory-related signal. Using a recently-developed source separation algorithm [1], we extracted real-time breath-by-breath TV and beat-to-beat SV signals continuously from the mechanically ventilated animals in this study. By demonstrating that SV and TV can be simultaneously measured in normal and reduced ventilation, we would present the potential of EIT technology for applying several clinical applications such as respiratory depression due to residual anaesthetics [2] in addition to the management of hemodynamically unstable patients [3].

2   Methods

The animal was connected to a mechanical ventilator (Hamilton-G5, Hamilton Medical, Switzerland) via tracheal intubation. The supplied air volume with a FiO_2 of 100% from the mechanical ventilator for normal ventilation was set to 8 ml/kg with a respiration rate (RR) of 12 bpm. Anaesthesia was maintained by continuous administration of pentobarbital (8.5 mg/kg/h) using an infusion pump. SpO_2 and $EtCO_2$ were measured from the ear and the intubation tube, respectively. Hemodynamic parameters of SV, cardiac output (CO) and mean arterial pressure (MAP) were measured using a hemodynamic monitor (EV1000, Edwards Lifesciences, U.S.) in the transpulmonary thermodilution (TPTD) and pulse contour analysis (PCA) modes with two catheters inserted in the central vein and femoral artery. When reducing the tidal volume to 70% and 30%, we investigated the feasibility of non-invasive simultaneous measurements of breath-by-breath TV and beat-to-beat SV in pigs using an EIT device and compare the measured TV and SV data with those of a mechanical ventilator and an invasive hemodynamic monitor.

The supplied air volume from the mechanical ventilator was reduced to 70% of the normal value for about 20 min. On returning to normal ventilation again for 5~10 min, we repeated the same procedure with 30% of the normal volume to simulate hypoventilation. R_2 and linear regression coefficient showed highly linear relationship between TV_{EIT} and TV_{VENT}, and SV_{EIT} and SV_{TPTD}.

3   Conclusions

The EIT device detected reduced ventilation reliably and accurately in all cases without any time delay. The results suggested that the EIT device could be used for simultaneous monitoring of TV and SV on non-intubated patients.
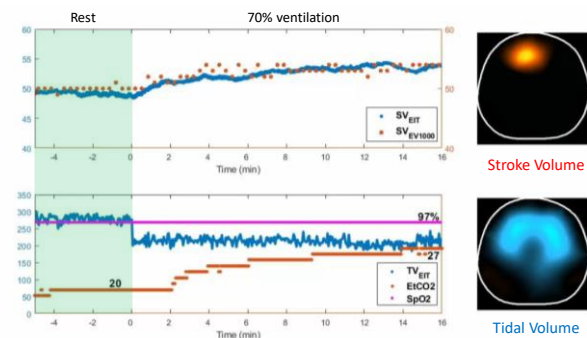
Figure 1: Changes in SV (upper graph) and TV (lower graph) during reduced ventilation at 70% level. SV_{EIT} and SV_{EV1000} are measured SV data using the EIT device and EV1000 in the PCA mode, respectively. $EtCO_2$ and SpO_2 are the end-tidal CO_2 and peripheral oxygen saturation.
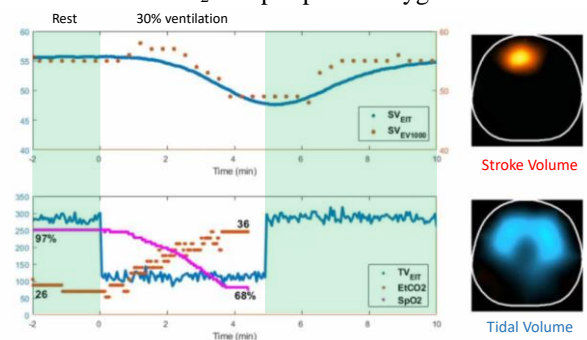
Figure 2: Changes in SV (upper graph) and TV (lower graph) during reduced ventilation at 30% level. SV dropped rapidly by the acute respiratory acidosis, and returned to normal after TV was switched back to normal.

4   Acknowledgements

References

[1] GY Jang, *et al.*, *Sci Rep*, 10:11242, 2020
[2] LA Lee, *et al.*, *anesthesiology*, 122:659-665, 2015
[3] RE Ko, *et al.*, *Shock*, in press, 2021

Quantification of recruitable alveolar collapse and hyperdistension during laparoscopic gynecological surgery and mechanical ventilation

Dargvainis M[1], Ohnesorge H[1], Alkatout I[2], Schädler D[1], Frerichs I[1], Becher T[1]

[1] Department of Anesthesiology and Intensive Care Medicine, University Medical Center Schleswig-Holstein, Campus Kiel, Germany,
[2] Department of Gynecology and Obstetrics, University Medical Center Schleswig-Holstein, Campus Kiel, Germany

Abstract: During laparoscopic gynecological surgery, we used EIT to assess positive end-expiratory pressure (PEEP) values required 1) to counteract atelectasis formation and 2) to balance alveolar collapse and hyperdistension. Both PEEP values were higher in Trendelenburg position with capnoperitoneum than in supine position.

1 Introduction

Laparoscopic surgery in Trendelenburg position may require an adapted strategy of lung-protective ventilation due to high intra-abdominal pressure caused by positioning and capnoperitoneum. Analysing tidal impedance changes with EIT can be useful for identifying regional alveolar collapse and hyperdistension during mechanical ventilation at different PEEP levels [1]. In a randomized clinical trial, ventilation with a PEEP that provided an equal balance between atelectasis formation and hyperdistension ("Best Compromise PEEP") resulted in a reduction of post-operative atelectasis in comparison to ventilation with a fixed PEEP of 4 cm H_2O [2]. The aim of the present study was to assess and compare Best Compromise PEEP and the PEEP level required to prevent atelectasis formation ("Open Lung PEEP") during mechanical ventilation for routine laparoscopic surgery.

2 Methods

We included 30 patients scheduled for laparoscopic gynecological surgery. Relative hyperdistension and alveolar collapse were assessed with EIT during a decremental PEEP trial ranging from 20 to 4 cmH_2O once in supine position after induction of anaesthesia and once in Trendelenburg position after establishment of capnoperitoneum. Open Lung PEEP was defined as the lowest PEEP level with $\leq 3\%$ of alveolar collapse. Best Compromise PEEP was defined as the PEEP level with equally balanced hyperdistension and collapse.

3 Results

Complete EIT data analysis could be accomplished in 27 patients (age: 35.8 ± 12.6 years, height: 168 ± 8 cm, body mass index (BMI): 26.5 ± 5.5 kg/m^2). During mechanical ventilation in supine position, the median Open Lung PEEP was 12 (IQR 8-14) cmH_2O, with 8.7 (IQR 4.7-15.5) % of hyperdistension and 1.7 (IQR 0.4-2.2) % of collapse. Best Compromise PEEP in this position was 8 (IQR 7.5-10) cmH_2O and associated with 4.2 (IQR 2.4-7.2) % of hyperdistension and 5.1 (IQR 3.9-6.5) % of collapse. In Trendelenburg position with capnoperitoneum, Open Lung

PEEP was 18 (IQR 18-20) cmH_2O (p < 0.001 vs supine position) and Best Compromise PEEP was 18 (IQR 16-20) cmH_2O (p < 0.001 vs supine position). Hyperdistension in Trendelenburg position was 1.8 (IQR 0.5-3.9) % for Open Lung PEEP and 1.5 (IQR 0.7-3.0) % for Best Compromise PEEP, whereas collapse amounted to 0 (IQR 0-1.2) % for Open Lung PEEP and 0.2 (IQR 0-2.7) % for Best Compromise PEEP. Both PEEP values were positively correlated with BMI during mechanical ventilation in supine position (r=0.75, p<0.0001 for Open Lung PEEP and r=0.64, p=0.0003 for Best Compromise PEEP) but not in Trendelenburg position with capnoperitoneum.
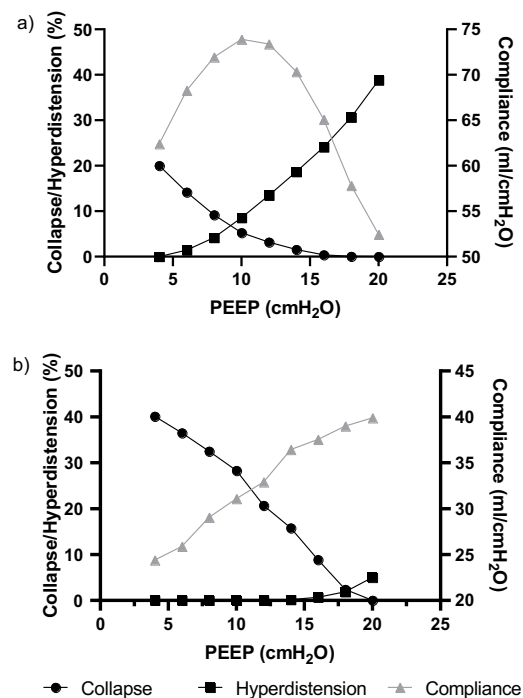
Figure 1: Decremental PEEP trial in supine position (a) and Trendelenburg position with capnoperitoneum (b). Each point represents mean value of 27 patients.

4 Conclusions

The PEEP levels required for preventing alveolar collapse and for balancing collapse and hyperdistension are higher in Trendelenburg position with capnoperitoneum than in supine position without capnoperitoneum. Even with high PEEP, alveolar hyperdistension was negligible during ventilation in Trendelenburg position with capnoperitoneum.

5 References

[1] Costa, ELV et al, Intensive Care Med 2009: 35, 1132-1137
[2] Pereira SM et al, Anesthesiology 2018: 129, 1070-10

Spatial sensitivity of regional EIT perfusion assessment in presence of inhomogeneous pulmonary background conductivity

M. Kircher[1,2], J. Osypka[1], B. Stender[2], T. Bluth[3], M. Gama de Abreu[3,4], O. Dössel[1]

[1]Institute of Biomedical Engineering, KIT, Karlsruhe, Germany, [2]Drägerwerk AG & Co. KGaA, Lübeck, Germany, [3]Pulmonary Engineering Group, University Hospital Carl Gustav Carus, Dresden, Germany, [4]Department of Intensive Care and Resuscitation and Department of Outcomes Research, Cleveland Clinic, Cleveland, OH, USA

Abstract: When measuring pulmonary perfusion with EIT in diseased and non-diseased lungs, the lung background conductivity influences the forward and inverse sensitivity. 3D sensitivity distributions were computed and compared for different simulated indicator concentrations in presence of three realistic lung conductivity backgrounds.

1 Introduction

Besides electrode placement and current injection pattern, the conductivity background has a strong influence on the sensitivity of EIT perfusion measurements. Thus, regional EIT perfusion estimates of an equal amount of blood flow to a collapsed and ventilated lung region might differ strongly. In the present simulation study, the forward and inverse sensitivity of pulsatile and indicator-enhanced EIT perfusion measurements in presence of heterogeneous lung backgrounds were investigated and their similarities assessed.

2 Methods

Data and model creation: Three thorax CT scans (inspiratory breath hold) of one pig from a recent study [1] during sequential experiments with severely different lung conductivity backgrounds were used: unilateral ventilation (E1), normal (bilateral) ventilation (E2) and zero PEEP ventilation after bilateral lung lavage (E3). After tissue segmentation of each CT volume, a triangular mesh was created and electrical conductivities were assigned to the thorax/soft tissue ($\sigma = 0.368\,\mathrm{Sm^{-1}}$), the heart ($\sigma = 0.705\,\mathrm{Sm^{-1}}$) and the bones ($\sigma = 0.021\,\mathrm{Sm^{-1}}$). To account for regionally heterogeneous lung parenchyma, each pulmonary mesh element was assigned a conductivity corresponding to its air filling factor, which was derived from CT Hounsfield units [2, 3] (see Figure 1, bottom row).

Forward/Inverse sensitivity: To assess regional sensitivity of perfusion measurements, spheres with a volume of 10 mL (volume of typical indicator bolus) and the conductivity of blood or a saline indicator (see Table 1, top row) were sequentially distributed within the lungs and the EIT forward problem was solved with EIDORS. Point electrodes and an adjacent stimulation pattern were used. EIT reconstruction was performed by linear reconstruction with Laplace regularization. The forward [2] and inverse sensitivity or amplitude response [4] was computed.

3 Results & Discussion

The distributions of forward sensitivity are depicted in Figure 1. Due to the increased contrast, the deviations of forward sensitivity distribution between experiments were reduced, if spheres with a 5 % NaCl bolus were simulated. The spatial profiles of inverse sensitivity are depicted in Figure 2. Additionally, the maximum of the correlation function R was computed between inverse sensitivity profiles of different experiments to assess similarity (as depicted in Table 1). Similarity increased strongly with increasing indicator concentration.

Table 1: Sphere conductivities σ and similarity measures between different inverse sensitivity profiles; c: indicator concentration in spheres (0 % $\widehat{=}$ blood); $R_{RL,12}$ ($R_{VD,23}$): similarity of right-left (ventro-dorsal) profile between E1 & E2 (E2 & E3)

c (%)	0	0.9	2	3	5	10
σ (Sm^{-1})	0.705	1.44	3.02	4.35	7.01	12.6
$R_{RL,12}$	0.82	0.95	0.98	0.99	0.99	0.99
$R_{VD,23}$	0.91	0.96	0.97	0.98	0.98	0.98

References

[1] T Bluth et al. *British Journal of Anaesthesia*, 123 (2): 246-254, 2019
[2] M Kircher, *PhD Thesis, Karlsruhe Institute of Technology (KIT)*, 2021
[3] P Nopp et al. *Physics in Medicine and Biology*, 38 (6), 699–716, 1993
[4] A Adler et al. *Physiological Measurement*, 30 (6), 35–55, 6 2009
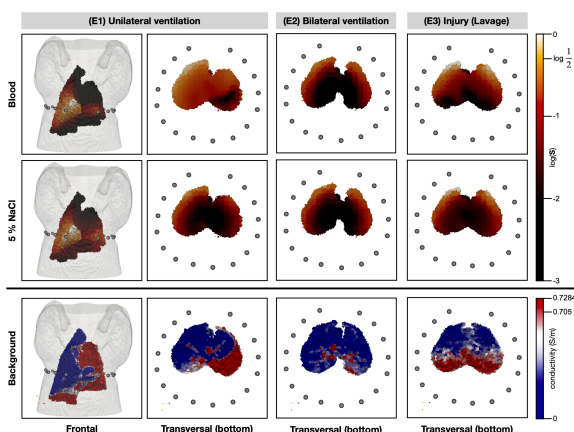
Figure 1: Forward sensitivity of all experiments; (1st/2nd row) sensitivity to spheres of blood or a 5 % saline solution; (3rd) pulmonary background; adapted from [2]
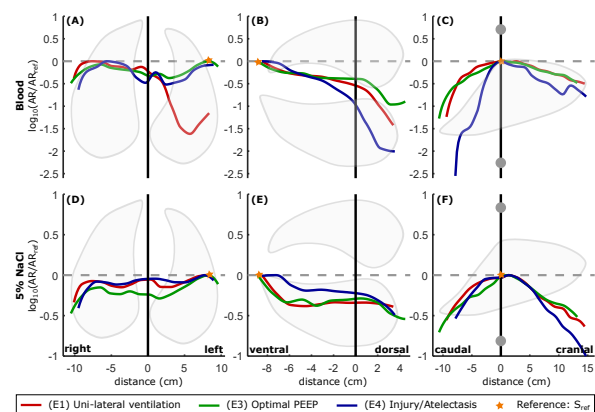
Figure 2: Normalized inverse sensitivity profiles (log scale); (A)-(C) sensitivity profiles for all spatial directions to spheres filled with blood; (D)-(F) sensitivity profiles for all spatial directions to spheres filled with 5 % NaCl; adapted from [2]

EIT for assessing ventilation distribution pre and post airway clearance in SMA–I patients

Andre Viera Pigatto[1], Tzu-Jen Kao[2], Jennifer L. Mueller[1,3], Christopher D. Baker[4], Emily M. DeBoer[4], Oren Kupfer[4]

[1]School of Biomedical Engineering, Colorado State University, Fort Collins, CO
[2]GE Research, Niskayuna, NY
[3]Department of Mathematics, Colorado State University, Fort Collins, CO, `mueller@math.colostate.edu`
[4]Department of Pediatrics, University of Colorado School of Medicine, Aurora, CO

Abstract: EIT data were collected on 6 pediatric patients with SMA–I pre, during, and post mechanical insufflation-exsufflation on two rows of 16 electrodes placed around the chest. Computed lung volumes estimates and images of pulmonary pulsatile perfusion suggest that EIT holds promise for estimating lung volumes and V/Q mismatch.

1 Introduction

Spinal muscular atrophy type I (SMA–I) is the most severe type of a genetic disease in which progressive muscle weakness leads to respiratory complications and eventual failure. Patients cannot perform effective coughing to clear mucus in the lungs that can lead to air trapping, atelectasis, infection, and pneumonia. Such respiratory complications are the leading cause of death in patients with SMA–I. Mechanical insufflation-exsufflation (MIE) is used for airway clearance, but the effect of MIE on the distribution of ventilation in the lung, duration of its beneficial effects, and its optimal use are open questions. Here we present the results of a pilot study of 6 SMA–I patients demonstrating the feasibility of using regional ventilation and perfusion images from EIT data to obtain estimates of lung volumes before, during, and after MIE.

2 Methods

This study was conducted at Children's Hospital Colorado (CHCO) in Aurora, CO in accordance with the amended Declaration of Helsinki under approval of the IRB. Six patients ages 4.0 ± 2.6 years participated. EIT data were collected on two rows of 16 electrodes placed around the chest using the GENESIS prototype EIT system from GE Research. Data were collected during tidal breathing before and after the MIE procedure as well as during the procedure. Trigonometric current patterns with a maximum amplitude of 0.11 mA rms were applied, and the ToDLeR algorithm [1] was used to compute 3-D dynamic reconstructions. The inspired volume of air was estimated for each frame from the reconstructed conductivity values in the EIT image using the method from [2]. Average values pre and post MIE over the six subjects are found in Table 1. Not all patients had large rises in lung volume post MIE. The estimates for Subjects 1 and 2 suggested a small post-MIE decline in lung volume. Figure 1 is a plot of the estimated volume of inspired air per frame for Subject 3 during the MIE procedure. The plot clearly shows when the device insufflates and exsufflates air and the rest periods between induced coughs.
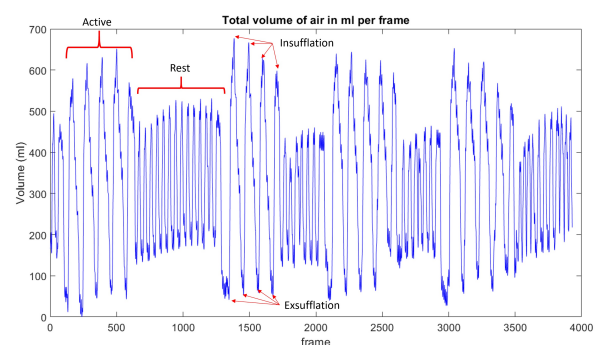
Figure 1: Volume estimates by frame for one subject computed from EIT data collected during the MIE procedure.

3 Conclusions

This study demonstrates that changes in regional ventilation distribution after MIE treatments are visible in the ventilation images, and lung volumes computed from segmented EIT images showed an increase in four of the six patients. The results underscore the need for a method of monitoring whether the application of MIE in a patient has indeed improved lung function and reduced V/Q mismatch.

4 Acknowledgements

References

[1] R S Blue, D Isaacson, J C Newell *Physiol Meas*, 21:1–12, 2000
[2] P A Muller, T Li, D Isaacson, J C Newell, G J Saulnier, T J Kao, J Ashe *Physiol Meas*, 36:1083–1295, 2015
[3] J Ashe, D Shoudy, G Boverman, J Sabatini, T J Kao, B Amm *15th International Conference on Biomedical Applications of EIT*, Gananoque, Ontario, Canada, April 2014

Table 1: Average volume of inspired air at maximum inspiration during tidal breathing (average$\pm$ SD)

	Pre-MIE (ml)	Post-MIE (ml)	Change (ml)	Change (%)
Average	541 ± 175	569 ± 148	58.8 ± 55.1	15.3 ± 10.0

Pulmonary Image Reconstruction in Multifrequencial EIT System for COVID-19

Julia Grasiela Busarello Wolff[1], Pedro Bertemes-Filho[1] and Wellington Pinheiro dos Santos[2]

[1]Electrical Engineering Department, Universidade do Estado de Santa Catarina, wolff1980@gmail.com
[2]Biomedical Engineering Department, Universidade Federal de Pernambuco

Abstract: Clinical acceptance of MfEIT's systems in several areas of medicine is well known in the literature. The D-Bar method was used to generate absolute lung images in patients affected by COVID-19. The results indicate that the method can be a useful tool in detection of pulmonary anomalies in ICU beds.

with COVID-19. For this purpose, use the D-Bar software to reconstruct images at different frequencies. It was found, as a proof of concept, that the numerical method D-Bar can be used in an MfEIT system to safely reconstruct pulmonary and cardiac images. Its use at low frequencies is not indicated.

1 Introduction

Multifrequencial electrical impedance tomography (MfEIT) is an important clinical tool to detect pulmonary pathologies associated with acute respiratory distress syndrome [1] and others diseases, such as, tumors. Recently, some authors have used MfEIT as a bedside adjuvant in patients with severe COVID-19 [2], [3] who cannot be removed from the ICU to perform magnetic resonance imaging, ultrasound and computed tomography. The objective of this work is investigate to use 2D D-Bar algorithm in a MfEIT system for monitoring the pulmonary status of patients with COVID-19.

2 Methods

D-Bar is a direct 2D method that consists of reconstructing images of electrical conductivities of the heart and lungs in the radiofrequency band, with good precision. It works with the low-pass filtering of a nonlinear Fourier transform and with Dirichlet-Neumann and Neumann-Dirichlet maps. Eleven D-Bar codes obtained in [4] were compiled, varying the conductivity values for the inspired lungs, frequencies of 5, 250, 750 and 2,500 kHz were selected in order to show that the software serves the bands from 100 kHz to 10 MHz well, and cannot be used at low frequencies. The mathematical modelling of both lungs and heart was represented by means of ellipses. We consider that the heart is full of blood and the lungs are full of air and back conductivity is 1 [S/m].

3 Results and Discussions

Figure 1 shows the original images on the left with their respective conductivities shown in Table I and the reconstructed images on the right. In some images, conductivity values in the heart were overestimated.

4 Conclusions

An analysis was presented on the use of an MfEIT system as an ICU bed tool for monitoring the pulmonary in patients
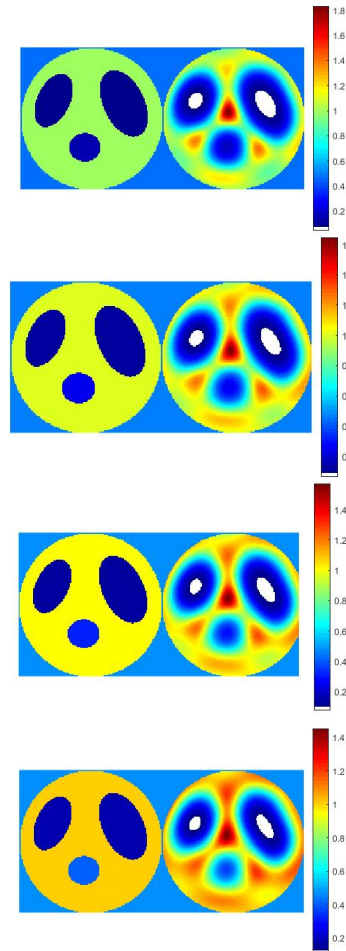
Figure 1: Image reconstruction in 5, 250, 750 and 2,500 kHz, respectively.

References

[1] Shono et al. *The Journal of Critical Care Medicine*, 7(1):62-66, 2021.
[2] Fu et al.*Physiol. Meas.*, 41: 085008, 2020.
[3] Zhao et al. *Critical Care,* 24, Article number: 272, 2020.
[4] Siltanen, S. Available in: https://blog.fips.fi/author/samu/. Access in: 15 may 2021.

Table I. Conductivity values at different frequencies for heart and lungs.

Frequency [kHz]	Heart [S/m]	Lungs [S/m]
5	0.13665	0.08914
250	0.24695	0.11493
750	0.30662	0.12978
2,500	0.39775	0.16737

Shape acquisition of the chest boundary to improve lung monitoring in infants

Serena de Gelidi[1], Andy Bardill[1], Nima Seifnaraghi[1], Yu Wu[2], Andreas Demosthenous[2], Marika Rahtu[3,4], Merja Kallio[3,4], Richard Bayford[1]

[1]Faculty of Science & Technology, Middlesex University, London, United Kingdom s.degelidi@mdx.ac.uk
[2]Department of Electronic and Electrical Engineering, University College London, London, United Kingdom
[3]PEDEGO Research Unit, Medical Research Center Oulu, University of Oulu, Finland
[4]Department of Children and Adolescents, Oulu University Hospital, Oulu, Finland

Abstract: Clinicians are aware of the compliant nature of the neonatal chest wall. Here, a wearable device designed to acquire the geometry of the chest boundary has been applied on newborns to quantify this aspect for the first time. A visible change in the thoracic morphology was captured depending on the lying position of the baby.

1 Introduction

Lung immaturity is critical for the survival of infants and in particular of preterm babies that often require assistance in Neonatal Intensive Care Units (NICU). The Electrical Impedance Tomography (EIT) technology has been introduced as supportive care for infants (http://cradlproject.org/). As the quality of the reconstructed image is higher when the actual anatomical boundary is taken into account, a new method for selecting a patient specific forward model has been presented [1]. Given the resulting potential beneficial impact on the clinical interventions based on EIT examinations and the need to optimize the fitting of the EIT device, there is a need to acquire rapidly and without any radiation the shape of the neonatal torso. The authors have already presented a device featuring accelerometers that could successfully carry out the acquisition of different shape boundaries *in vitro* [2]. The present study aims at applying the same technology *in vivo* for an unprecedented collection of neonatal torso shape measurements performed in real time by means of a wearable electronic belt. Hence, the goal is to quantify the biomechanical changes of the neonatal chest in different lying positions.

2 Methods

The device features an array of 32 high resolution 3-axis accelerometers ADXL313 (Analog Devices, Norwood, MA, USA). Furthermore, a soft custom made encapsulation prevents any possible current transfer to the skin of the baby and it can be easily sanitized for each patient. The electronic measuring belt was used to perform 7 measurements of the torso in 6 different positions. A laptop, being the only power source, was connected to an Arduino microcontroller and a multiplexer, both housed in a box. Such box was wired to the device, as shown in Figure 1. The measuring process is activated from the custom made script in MatLab (Mathworks, Nantick, MA, USA) on the laptop via a serial communication. Firstly, the patient details are entered (e.g. gestational age, weight). Secondly, the morphology of the thoracic boundary in each position is instantaneously recorded, the cross-sectional area is plotted as feedback and the data saved on the laptop.

Figure 1: The electronic measuring belt applied by a clinician on one of the participants lying on the left side [3].

3 Results

After obtaining written informed consent of both parents, 31 newborns and 1 child were included in the present pilot study carried out at the Oulu University Hospital. No restriction of breathing or skin irritation was observed whilst the belt was wrapped around the chest and held in place by the clinician. Distinctive changes of morphology were observed in the chest boundary by comparing the prone or supine positions to the lateral ones.

4 Discussion

The distortion of the chest wall can be explained by its increased compliance compared to the lung, to the incomplete ossification of the ribs and to the respiratory muscles unable to stabilize the chest wall [4]. Such distortion has been captured for the first time in the present study. Once integrated to the EIT system, the present observation could potentially improve the medical diagnosis of the infants admitted to the NICU.

5 Acknowledgements

References

[1] Seifnaraghi N, De Gelidi S, Kallio M, Nordebo S, Suo-palosaari M, Frerichs I, Sorantin E, Van Kaam A, Sophocleous L, Tizzard A, Demosthenous A, Bayford R. *IEEE Transactions on Biomedical Engineering*, 9294:1–1, 2021

[2] De Gelidi S, Seifnaraghi N, Bardill A, Tizzard A, Wu Y, Sorantin E, Nordebo S, Demosthenous A, Bayford R. *Physiological Measurement*, 39, 2018

[3] De Gelidi S, Bardill A, Seifnaraghi N, Wu Y, Demosthenous A, Rahtu M, Kallio M, Bayford R. *Scientific Reports*, 11:4446, 2021

[4] Davis G M, Coates A L, Papageorgiou A, Bureau M A. *Journal of Applied Physiology*, 65:1093–1098, 1988

Three broad classifications of acute respiratory failure etiologies based on regional ventilation and perfusion by EIT

Huaiwu He[1*], Chi Yi[1], Yun Long[1], Siyi Yuan[1], Rui Zhang[1], YingYing Yang[1], Zhanqi Zhao[2,3]

[1]Department of Critical Care Medicine, Peking Union Medical College Hospital, Peking Union Medical College, Chinese Academy of Medical Sciences, Beijing, China, *tjmuhhw@126.com
[2]Department of Biomedical Engineering, Fourth Military Medical University, Xi'an, China
[3]Institute of Technical Medicine, Furtwangen University, Villingen-Schwenningen, Germany

Abstract: The study explored the feasibility to discriminate acute respiratory failure etiologies with EIT. Regional distribution defect scores for ventilation and perfusion were proposed and evaluated in 108 ICU patients. The results indicated that high specificities (>90%) could be achieved to distinguish studied etiologies

1 Introduction

Acute respiratory failure (ARF) does not always present in conditions that are ideal for an immediate etiologic diagnosis [1]. Rapid and accurate identification of ARF etiology plays a critical role in the initial treatment of the affected patients and is related to outcomes [2]. Electrical impedance tomography (EIT) is the only bedside method provides ventilation and perfusion information that may serve this purpose [3].

The aim of study was to validate whether regional ventilation and perfusion data by saline-contrast EIT method could discriminate the three broad ARF etiologies (pulmonary embolism related disease PED, diffuse lung involvement disease DLD and focal lung involvement disease FLD).

2 Methods

The study was approved by the Institutional Research and Ethics Committee of the Peking Union Medical College Hospital. Informed consent was obtained from all patients or next of kin before data were included into the study.

A total of 108 ICU patients were prospectively included: 93 with ARF and 15 without as control (postoperative ICU patients). EIT measurements were performed with PulmoVista 500 (Dräger Medical, Lübeck, Germany). EIT measurements were continuously recorded at 20 Hz when the patients were at relative stable condition after medical treatment. A bolus of 10ml 10% NaCl was injected during a respiratory pause (at least for 8s) through the central venous catheter. The respiratory pause was conducted via an end-expiratory hold manoeuvre with the ventilator in the intubated patients.

Regional ventilation map was calculated by subtracting the end-expiration from the end-inspiration image. Regional perfusion map was generated by the slope of regional impedance-time curves after the saline bolus injection [4]. Both ventilation and perfusion maps were divided into the symmetrical, non-overlapping, four cross-quadrants: lower left, lower right, upper left and upper right. The regional ventilation distribution (%), perfusion distribution (%) and V(%)/Q(%) were calculated in each quadrant. Distribution defect of each quadrant is scored as: 0 (quadrant distribution>15%), 1 (15%>quadrant distribution>10%) and 2 (quadrant distribution<10%). Defect scores were calculated by the sum of four cross-quadrants to denote the corresponding defect scores for ventilation and perfusion, respectively. V+Q defect score was the combined score calculated as sum of both ventilation and perfusion scores.

3 Results

Significant differences of the investigated defect scores were found between the control group and PED, between control and FLD (p<0.05; Fig. 1). With the aim to achieve a high specificity, a cutoff value of perfusion Defect score>2.5 was used for the diagnosis PED (n=14), resulting in a sensitivity of 21.4% and a specificity of 94.9% amount the ARF patients. A cutoff value of combine defect score>0.5 was used for the diagnosis DLD (n=21), resulting in a sensitivity of 66.7% and a specificity of 90.3%. A cutoff value of ventilation defect score>2.5 was used for the diagnosis FLD (n=58), resulting in a sensitivity of 39.7% and a specificity of 97.1%.

4 Conclusion

The combined measurement of ventilation and perfusion by EIT with saline bolus injection could identify probable etiologies of ARF at bedside. Phenotype of EIT ventilation and perfusion image might be helpful for a broad diagnose of ARF etiologies, and further study is required to validate the impact of the described saline-based EIT method the management of the critically ill patients with ARF.

References

[1] DA Lichtenstein, GA Mezière *Chest*, 134:117-125,2008
[2] P Ray, S Birolleau, Y Lefort, et al *Crit Care*, 10:R82, 2005
[3] I Frerichs, MB Amato, AH van Kaam, et al *Thorax*, 72:83-93,2017
[4] H He, Y Long, S Yuan, et al Crit Care, 24:586, 2020
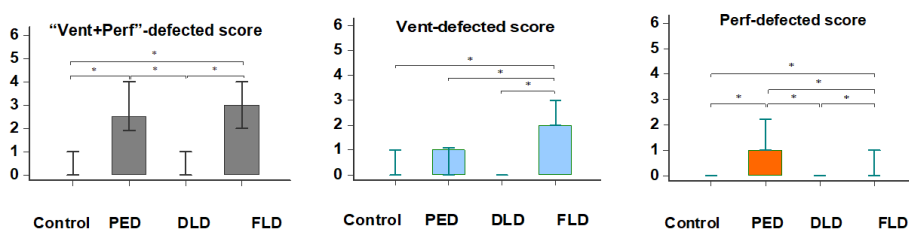
Fig. 1. Comparisons of Defect scores for ventilation (middle), perfusion (right) and combined (left) in the four groups.

Feasibility of Thoracic Impedance Measurements in Seawater

Andy Adler[1], Olivia Brabant[2], Andreas Fahlman[3], Adrian Gleiss[2], Tarek Nasser El Harake[1], Martina Mosing[2]

[1]Carleton University, Ottawa, Canada
[2]Murdoch University, Perth, Australia
[3]Global Diving Research Inc, Ottawa, Canada

Abstract: There is are numerous poorly understood aspects of breathing by aquatic mammals. Impedance measurements and EIT could provide useful information. We conduct simulations and show early results of impedance measurements in seawater.

1   Introduction

Breathing in aquatic mammals is poorly understood; of particular interest are changes in the respiratory mechanics while diving [2]. Improvements in this area may be useful to our understanding of humans diving. The effect of breath-hold diving on pulmonary function humans and marine mammals is poorly understood. Studies have shown that increasing pressure causes alveolar compression and a depth-dependent pulmonary shunt that eventually results in alveolar collapse and cessation of gas exchange. A better understanding of these changes in gas exchange with depth could lead to novel clinical management and perhaps explain stress-associated stranding of marine mammals [1].

Bioimpedance measurements (BioZ) and EIT have seen much use in land mammals as a technique to monitor breathing and the distribution of lung gasses in a non-invasive way. It would be exciting if such measurements were possible in seawater.

2   Methods: Simulations

The key challenge: seawater is much more conductive than body tissues (5.0 S/m compared to 0.7 S/m for blood). This means that current can travel more easily outside the body than inside, and would suggest that the EIT sensitivity to conductivity changes is much lower.
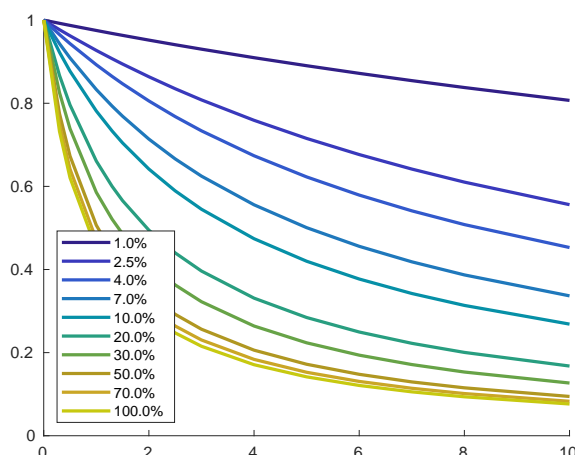
Figure 1: Relative EIT sensitivity to a conductivity change in the centre of a circular body, as a function of the conductivity ratio ($\sigma_{\text{seawater}}/\sigma_{\text{body average}}$) of the liquid into which the body is placed. Lines correspond to the thickness of the liquid layer as a function of the body radius.

In order to understand the impact of this changed sensitivity, we build a finite-element model of a circular body with 16 electrodes with spherical "heart" in the centre which received a bolus of conductive blood. A "seawater" region around the body was created of varying thickness (to simulate either a neoprene-covered body (small thickness) or open water (large thickness). The adjacent protocol EIT signal was simulated and the rms signal normalized to the open air (zero conductivity around the body) case. Results (Fig 1) show that open seawater surrounding a body decreases the signal to less than 10% of it's original value. On the other hand, a non-conductive neoprene layer will expose only a small thickness of seawater around the body, potentially keeping up to 80% of the signal.

3   Methods: Experiment

In order to explore the effect, experiments were made to measure thoracic bioimpedance for a human going from air to salt water. Our volunteer started standing in a salt-water pool with with water at waist height and electrodes placed underneath a neoprene wetsuit. A $t = 20\,\text{s}$ the subject descended into the water. Breathing maneuvers (deep breathing, tidal breathing and breath hold) were performed, and results shown in Fig 2. Results suggest that physiological BioZ changes can be measured in the water.
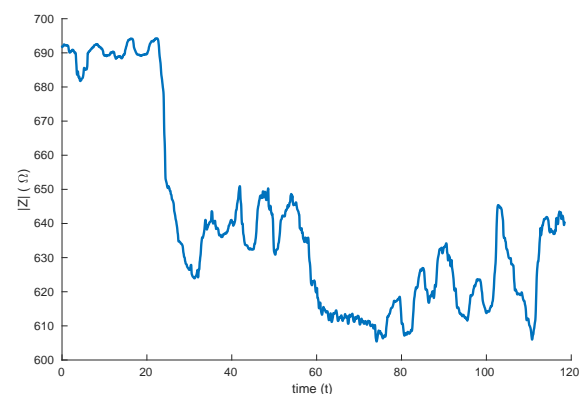
Figure 2: Two-electrodes bioimpedance vs time measured with a MAX30001 bioimpedance demo kit (Maxim Integrated). The subject entered the water at $t = 20\,\text{s}$. Deep breathing maneuvers were done, and breath was held between $60 - 75\,\text{s}$.

4   Conclusions

We present simulations and a pilot experiments which suggest that bioimpedance and EIT measurements in salt water are difficult, but possible.

References

[1] Fahlman et al, *Frontiers in Marine Science*, fmars.2021.598633.
[2] Lemaitre et al *J Sports Sciences* 27:1519-1534, 2009.

Session 8: Algorithms II

D-bar reconstructions of human ventilation EIT data with a statistical prior applied through a Schur complement property

Talles Batista Rattis Santos[1], Rafael Mikio Nakanishi[2], Erick Dario León Bueno de Camargo[3],
Raul Gonzalez Lima[2], Jennifer L. Mueller[1]

[1]Department of Mathematics and School of Biomedical Engineering, Colorado State University,
Talles.Santos@colostate.edu
[2]Mechanical Engineering Department, University of São Paulo
[3]Biomedical Engineering - Engineering, Modeling and Applied Social Sciences Centre, Federal University of ABC

Abstract: In this work, anatomical information based on CT scans, and physiological information from *in vivo* measurements are used to improve the spatial resolution of cross-sectional human thorax D-bar conductivity images. The Schur complement property is used to introduce prior information in a post-processing approach.

1   Introduction

To improve the spatial resolution of D-bar reconstructions [2] from Electrical Impedance Tomography (EIT) data, the use of prior information may be applied. By taking into account the density of the conductivity distribution of a population, and using the Schur complement property, Santos et al.[3] proposed a post-reconstruction correction to improve the spatial resolution of the D-bar images of experimental phantoms.

In this work, the post-reconstruction correction is applied for human data. The density of conductivity distribution of a population is estimated, and statistical information is used to post-process the D-bar images of two patients.

2   Method

EIT data collected in previous experiments as part of a larger study conducted in accordance with the amended Declaration of Helsinki–Ethical Principles for Medical Research Involving Human Subjects were used. These data were collected at Children's Hospital Colorado, Aurora, CO under the approval of the Colorado Multiple Institutional Review Board (COMIRB) (approval number COMIRB 14-0652) with informed written parental consent and children's informed assent. EIT data were collected using the ACE1 EIT System [4]. CT scans collected in previous studies approved by the Research Ethics Committee of the University of São Paulo Medical School (approval numbers 324.563, 1.015.334 and 1076/06) were used.

Healthy adult male CT scans (74) were segmented in bones, lungs, heart and muscles. For each segmentation, 2,500 samples were randomly generated following the mean and variance of the conductivity of the tissues [1]. A refined forward problem solver was used to estimate the EIT voltages of each conductivity distribution. Then, D-bar images were reconstructed based on these computed voltages.

By using the conductivity distributions generated from the segmentations and the D-bar images from the computed voltages, a post-processing correction was applied using the Schur complement property as described in [3, Sec. IIIB].

3   Results

Figure 1 shows the statistical distribution of the conductivity variation in a cross-section of the thorax. Figures 2a and 2c show the cross-section of the CT scans where the EIT belt were placed, and figures 2b and 2d show the post-processed images at full inspiration. Results demonstrate a qualitative improvement in resolution when the post-processing method is applied.

(a) Mean   **(b)** Std.
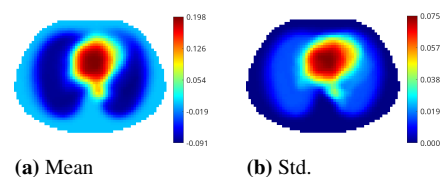
Figure 1: Mean and std. of the cond. variation distribution

(a) P1, CT scan   **(b)** P1, D-bar img

(c) P2, CT scan   **(d)** P2, D-bar img
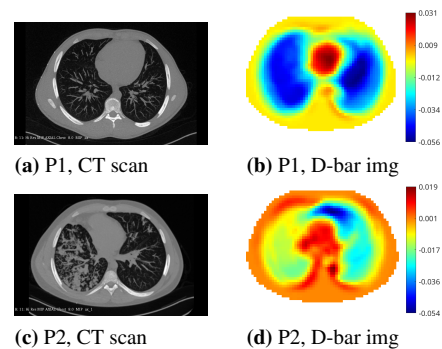
Figure 2: CT scans ((a), (c)) and Post-Proc. images ((b), (d))

4   Conclusions

The use of post-reconstruction correction based on Schur complement property is feasible for human data with significant improvement of the spatial resolution. Further studies are desired to quantify the spatial resolution improvement, and to determine the efficacy of the method for human data.

5   Acknowledgments

References

[1] E D L B Camargo *PhD thesis*, University of São Paulo, 2013
[2] J L Mueller, S Siltanen *SIAM*, Philadelphia, PA, 2012
[3] T B R Santos, R M Nakanishi, J P Kaipio, J L Mueller, R G Lima *IEEETransactions on Medical Imaging*, 39, 2020
[4] M M Mellenthin, J L Mueller, E D L B Camargo, F S Moura, T B R Santos, R G Lima, S J Hamilton, P A Mueller, M Alsaker *IEEE Transactions on Instrumentation and Measurement*, 68, 2019

The SVD of the linearized EIT problem on a disk

Andy Adler[1] and William R.B. Lionheart[2]

[1]Systems and Computer Engineering, Carleton University,
[2]Department of Mathematics, University of Manchester, `bill.lionheart@manchester.ac.uk`

Abstract: In this paper we calculate the right singular functions to the linearized EIT problem on homogeneous disk. We note the similarity to Zernike disk functions and the dependence on the mesh.

1 Introduction

The Singular Value Decomposition (SVD) helps us to understand the ill-conditioning of a linear inverse imaging problem, it characterizes consistent data and gives a basis for images in order of how easy their components are to recover. For some important inverse imaging problems an explicit analytic form of the SVD is known. For example, for the Radon transform on a disk the singular functions on the image side are Zernike disk functions while on the data side they are Fourier basis functions in two angular coordinates [1, Ch7]. Often symmetry conditions and commutation with a partial differential operator are the key to finding these explicitly. In many cases the forward operator is compact and therefore the spectrum is discrete, that is the singular values σ_i are indexed by an integer. Many important operators that appear in inverse imaging problems, such as restricted Hilbert transforms, do not have a discrete spectrum [2]. In that case numerical calculation of the SVD will depend heavily on the discretization used.

In this paper we calculate the singular functions of the linearized EIT forward problem on a uniform disk, discretized using a triangular mesh. We find that the right singular functions (on the image side) appear as two series. One very close to Zernike disk functions and the other highly oscillatory and concentrated near the boundary. The singular functions are sorted by their decreasing singular value and the two series are interspersed in a way that is highly dependent on the mesh.

2 Methods

We use a triangular mesh of the disk, and for maximal symmetry use trigonometric current drive and measurement patterns. In this discrete context the Fréchet derivative of the forward problem is approximated by the Jacobian matrix J (sensitivity), and is calculated using EIDORS v3.10 [4] with a unit background conductivity. The singular values of J are σ_i and right singular vectors v_i where

$$J^T J v_i = \sigma_i^2 v_i$$

and the σ_i are arranged in non decreasing order. The right singular vectors are approximately the average of the right singular functions in each triangle of the mesh and form an orthonormal basis for the discrete image space. The significance of the right singular vectors is that they are components of a conductivity image ordered by how difficult they are to recover from EIT measurement.

3 Results

As shown in fig. 1 we see that the right singular functions appear as two series: the most obvious being very close to the Zernike disk functions, the same as the right singular functions of the Radon transform on the disk. The other series is highly oscillatory and concentrated near the boundary. If the mesh is changed qualitatively the same functions appear but way the second series is interposed in the first varies.
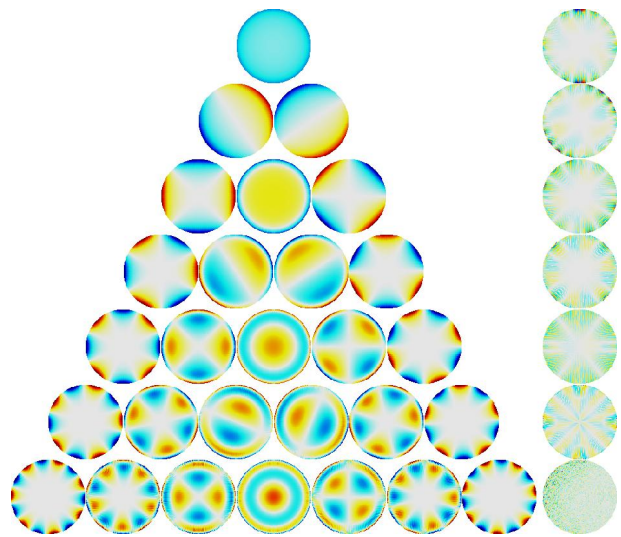
Figure 1: Images of right singular functions of EIT Jacobian of the unit disk, using a 17424-element 2D model with the four low-order sinusoidal drive and measurement patterns. *Left*: Zernike-like singular functions, corresponding to the singular values [1; 2,3; 4,12,5; 6,15,16,7; 8,19,21,20,9; 10,22,26,27,23,11; 17,28,30,32,31,29,18]. *Right*: sample of the mesh dependent singular functions concentrated near the boundary [37,40,46,49,58,105,126].

4 Conclusions

The identification numerically of the right singular functions as close to Zernike disk functions settles a problem raised when the SVD of EIT was first calculated in the second author's PhD [3]. The rotationally symmetric case can be shown to be equivalent to a Hilbert transform on adjacent intervals and has a continuous spectrum[2]. We conjecture that the variability of the singular values of the second series is due to partly continuous spectrum and it sounds a note of caution for the mesh dependence of EIT reconstruction.

References

[1] P.C. Hansen, J. S. Jørgensen, W.R.B. Lionheart, *Computed Tomography: Algorithms, Insight and Just Enough Theory*, SIAM 2021
[2] M. Bertola, E. Blackstone, A. Katsevich, and A. Tovbis. *Anal. Math. Phys*, 10:1–59, 2020.
[3] W.R. Breckon, Image Reconstruction in Electrical Impedance Tomography by , PhD Thesis Oxford Polytechnic, 1990
[4] A Adler and W.R.B Lionheart, Physiol. Meas., 27:S25-S42,2006.

Fast 3D Deep CGO-based Reconstruction for Absolute EIT

S.J. Hamilton[1], A. Hauptmann[2], V. Kolehmainen[3], P.A. Muller[4], J. Toivanen[3], X. Tong[1]

[1]Mathematical and Statistical Sciences, Marquette University, `sarah.hamilton@marquette.edu`
[2]Research Unit of Mathematical Sciences, University of Oulu
[3]Applied Physics, University of Eastern Finland
[4]Mathematics & Statistics, Villanova University

Abstract: The 3D absolute EIT reconstruction problem is notoriously challenging. Here we pair fast 3D CGO-based absolute reconstructions ($\sim$5 sec/image) with a trained U-net CNN to sharpen the blurry CGO images. Results are presented for simulated noisy voltage data and show generalizability to out-of-distribution domain shapes and targets.

1 Introduction

The absolute EIT reconstruction task is a severely ill-posed inverse problem of the mathematical inverse problem that requires carefully designed algorithms robust to noise and modeling errors. In 3D, the computational cost of solving the absolute EIT problem using optimization-based methods is prohibitively high due to the repeated solution of the 3D FEM calculation and associated Jacobian which can take hours for a reliable image. In contrast, CGO-based reconstruction methods ([1], [2]) have recently been extended to 3D electrode data [3] and provide a fast alternative requiring only around 5 seconds per image (not optimized). As in 2D with D-bar CGO methods, the 3D $\mathbf{t}^{\text{exp}}$ and Calderón methods require a low-pass filter of the associated (non)linear Fourier data which results in smooth reconstructions. By viewing these blurred images as convolutions, we can train a Convolutional Neural Network (CNN) to undo the blurring and use the trained network as a postprocessing step to improve the CGO images. This approach showed great promise in 2D for Deep D-bar methods ([4], [5]) and behaves similarly in the 3D Deep CGO setting.

2 Methods

In [3] we developed the first 3D CGO-based absolute EIT reconstruction algorithm from CEM electrode data. Previously all 3D CGO-based reconstruction had been limited to continuum boundary data with the exception of Calderón's method which had been implemented for difference imaging with experimental electrode data. Both $\mathbf{t}^{\text{exp}}$ and Calderón are direct methods which solve a simplified version of the fully nonlinear problem.

The $\mathbf{t}^{\text{exp}}$ method uses a 'Born approximation' to the full nonlinear method [1], using the asymptotic behavior of the CGO solutions in the associated nonlinear Fourier data (called the scattering data) of $q(x) = \Delta\sqrt{\sigma(x)}/\sqrt{\sigma(x)}$. This scattering data $\mathbf{t}^{\text{exp}}(\xi, \zeta(\xi))$, is also computed using the current and voltage electrode measurements, and $q(x)$ is recovered from an inverse Fourier transform of $\mathbf{t}^{\text{exp}}$. The conductivity σ is then recovered by solving $q(x) = \Delta\sqrt{\sigma(x)}/\sqrt{\sigma(x)}$. The algorithm is given by:

$$(\Lambda_\sigma, \Lambda_1) \xrightarrow{1} \mathbf{t}^{\text{exp}}(\xi, \zeta) \xrightarrow{2} \mathbf{q}^{\text{exp}} \xrightarrow{3} \sigma^{\text{exp}}. \qquad (1)$$

For the training we generated conductivities $\sigma_n \in L^\infty(\Omega \subset \mathbb{R}^3)$, solved the forward EIT problem using the CEM boundary conditions and 64 electrodes, added 0.1% relative noise to the voltage data, and computed the corresponding low-pass $\mathbf{t}^{\text{exp}}$ reconstructions σ_n^{exp} using (1). Nineteen elliptical domains were used and distinct 1000 samples created for each. Each sample contained 1-5 elliptical inclusions of varying size and conductivity. A CNN was trained on the noisy reconstructions and used to post-process new samples not seen by the network. Preliminary results are shown in Figure 1 for the indicated axial cross-sections.

3 Conclusions

The speed of CGO-based reconstruction for 3D EIT makes it a viable candidate for pairing with deep learning post-processing methods. The combination results in significant improvements in dynamic range, MSE, SSIM, localization error, and relative volume ratio. The methods developed here work with absolute and time-difference EIT in 3D. Further details will be given in the presentation.
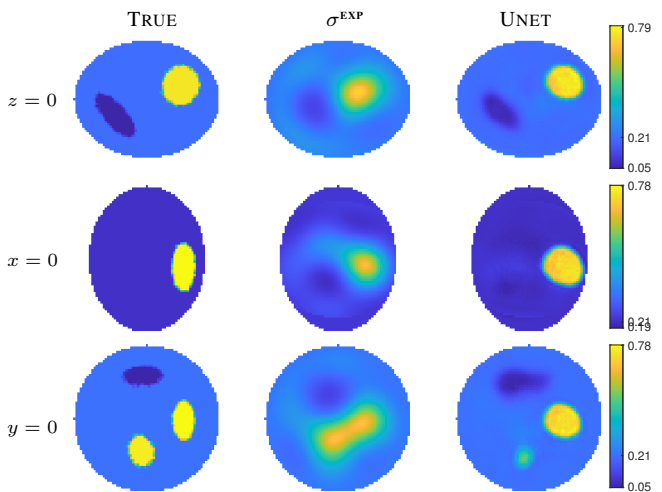
Figure 1: Cross-sections of the $\mathbf{t}^{\text{exp}}$ and UNET reconstructions compared to the truth for 0.1% noisy voltage data and a test sample not used in training for an 3D elliptical domain.

4 Acknowledgements

References

[1] AI Nachman. *Ann Math* **128**:531–576, 1988
[2] AP Calderón. In *Sem Num An and Appl to Cont Phys*, 65–73. Soc. Brasil. Mat., Rio de Janeiro, 1980
[3] SJ Hamilton, D Isaacson, V Kolehmainen, PA Muller, J Toivanen, PF Bray. *Inv Prob and Imag* 2021 (To Appear)
[4] SJ Hamilton, A Hauptmann. *IEEE TMI* 37(10):2367-2377, 2018.
[5] SJ Hamilton, A Hänninen, A Hauptmann, and V Kolehmainen. *Phys. Meas.* 40(7):074002, 2019.

Graph Convolutional Networks for Model-Based EIT Reconstruction

William Herzberg[1], Daniel B. Rowe[1], Andreas Hauptmann[2,3], and Sarah J. Hamilton[1]

[1]Computational, Mathematical, and Statistical Sciences, Marquette University, Milwaukee, WI,
`william.herzberg@marquette.edu`
[2]Research Unit of Mathematical Sciences, University of Oulu, Oulu, Finland
[3]Department of Computer Science, University College London, London, United Kingdom

Abstract: A model-based, iterative, learned reconstruction scheme is presented which leverages the use of flexible graph convolutional layers directly on data defined over an irregular finite element mesh. When considering absolute EIT images, the new method shows strong fitting capability and can easily generalize to new domain shapes.

1 Introduction

Many learned image reconstruction schemes utilize fully connected layers or convolutional layers in neural networks. Fully connected layers provide strong fitting capabilities but are prone to overfitting and require consistent input shapes. Convolutional layers also provide strong fitting capabilities by making use of localized information and sharing weights spatially across the layer. Unlike fully connected layers, convolutional layers can handle inputs of different sizes so long as they are uniform pixel grids.

However, in EIT and other nonlinear inverse problems, data is often defined over irregular finite element meshes as opposed to uniform pixel grids. This prohibits the use of convolutional layers without also using interpolation and embedding to convert to a regular pixel grid. As an alternative, this work introduces the idea of considering the data defined over the irregular mesh as an undirected graph to be used as input to a neural network with graph convolutional layers. The graph convolutional layer provides many of the same benefits as the traditional convolutional layer but is flexible enough to handle irregular inputs [1].

2 Methods

Classical optimization-based methods for solving nonlinear inverse problems, such as the Levenberg-Marquardt (LM) algorithm or regularized Gauss-Newton (GN) methods, have previously been applied to the absolute EIT reconstruction problem. These methods use gradient information of the forward model (the complete electrode model was used here) to compute iterative updates $\delta\sigma_k$ that are added to the current iterate σ_k as

$$\sigma_{k+1} = \sigma_k + \delta\sigma_k \qquad (1)$$

to improve the approximated solution to an objective function. The Graph Convolutional Newton's Method (GCNM) utilizes the same classical methods for computing updates but uses small graph convolutional networks at each iteration of a model-based, learned reconstruction method [2] to combine the current iterate and its update to produce the next iterate. This can be described by

$$\sigma_{k+1} = \Lambda_{\theta_k}\big(H_k^{(0)}, \mathcal{A}\big) \qquad (2)$$

where $H_k^{(0)} = [\sigma_k, \delta\sigma_k] \in \mathbb{R}^{M\times 2}$ is formed by placing the features defined over the mesh in the columns of a feature matrix of a graph with connectivity $\mathcal{A} \in \mathbb{R}^{M\times M}$ derived from the mesh structure. Each block Λ_{θ_k} of the network has the same structure, shown in Figure 1, but is trained individually to have a unique set of learned parameters θ_k.
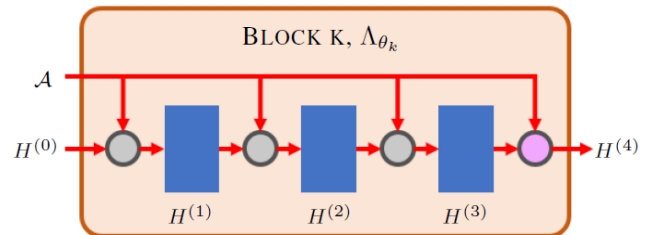
Figure 1: One block of a GCNM network is shown. Blue boxes represent feature matrices at each layer of the network while circles represent graph convolutions with ReLU (grey) and linear (pink) activation functions [3].

3 Conclusions

The GCNM provides a simple, yet highly flexible, network architecture that can leverage model information via the update terms and learn a task-specific prior from training data to solve nonlinear inverse problems such as EIT reconstruction. In addition, trained networks can be applied to samples with new boundary shapes and meshes. Figure 2 provides a simulated sample reconstruction on a chest shaped domain where the GCNM was trained only on samples with circular domains [3]. Note that 0.5% relative Gaussian noise was added to the training measurement data and this sample's measurement data.
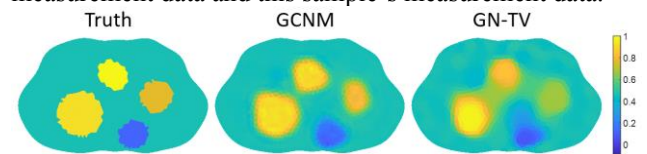
Figure 2: A reconstruction of a simulated sample using the new GCNM is compared to the truth and a reconstruction using Gauss-Newton method with Total Variation regularizatopm.

4 Acknowledgements

References

[1] Kipf T, Welling M *ICLR 2017*, Toulon, France, Apr 2017
[2] A Hauptmann et al. *IEEE-TMI* 37.6: 1382-1393, Jun 2018
[3] W Herzberg et al. arXiv:2103.15138, Mar 2021

Direct Regularized Reconstruction for 3D EIT in Stroke Detection

Kim Knudsen[1] and Aksel Kaastrup Rasmussen[1]

[1]Department of Applied Mathematics and Computer Science, Technical University of Denmark, akara@dtu.dk

Abstract: We present a regularization strategy for the Calderón problem in three dimensions based on large frequency truncation of the information in the Dirichlet-to-Neumann map. The method is tested on simulated data representing a hemorrhagic stroke.

1 Introduction

Electrical Impedance Tomography (EIT) provides a non-invasive method of obtaining information on the electrical conductivity distribution of a conductive domain Ω. The mathematical problem posed by Calderón is to determine stably a parameter γ from electrostatic boundary measurements in the form of the so-called Dirichlet-to-Neumann map. For $n \geq 3$ theoretical reconstruction for $\gamma \in C^2(\overline{\Omega})$ is based on complex geometrical optics (CGO) solutions $\psi_\zeta(x)$ close to a complex exponential $e^{i\zeta \cdot x}$, $\zeta \in \mathbb{C}^3$, of a Schrödinger equation in $\mathbb{R}^3$. Existence and uniqueness of CGO solutions is guaranteed for large complex frequencies $|\zeta|$ and allows recovery of the frequency information $\mathbf{t}$ of $q = \Delta\gamma^{1/2}/\gamma^{1/2}$ from Λ_γ. Reconstruction is usually presented in three steps:

$$\Lambda_\gamma \longrightarrow \mathbf{t} \longrightarrow q \longrightarrow \gamma. \tag{1}$$

The Calderón problem is known to be conditionally logarithmically stable. In the case of perturbed measurements $\Lambda_\gamma^\varepsilon = \Lambda_\gamma + \mathcal{E}$, $\|\mathcal{E}\| \leq \varepsilon$, $\mathbf{t}$ is exponentially perturbed. To mitigate this we propose a reconstruction method $\mathcal{R}$ that utilizes truncation of the large complex frequencies of ψ_ζ and the real frequencies of $\mathbf{t}$. This provides smoothing to the reconstructions and gives a regularization scheme with a regularization parameter based on the truncation radius [1] similar to the related 2D D-bar reconstruction [2].

2 Direct reconstruction method

Given perturbed measurements $\Lambda_\gamma^\varepsilon$ we can reconstruct γ^ε for sufficiently small perturbations $\mathcal{E}$ non-iteratively.
Step 1$^\varepsilon$ Let $M = M(\varepsilon) > 0$ be determined by a sufficiently small ε. For each fixed ξ with $|\xi| < M$, take admissible $\zeta(\xi)$ with $|\zeta(\xi)| = M^p$ for some $p > 3/2$ and recover $\psi_\zeta^\varepsilon|_{\partial\Omega}$. Compute the truncated scattering transform by

$$\mathbf{t}_M^\varepsilon(\xi) = \begin{cases} \int_{\partial\Omega} e^{-ix\cdot(\xi+\zeta)}(\Lambda_\gamma^\varepsilon - \Lambda_1)\psi_\zeta^\varepsilon & |\xi| < M, \\ 0 & |\xi| \geq M, \end{cases} \tag{2}$$

Step 2$^\varepsilon$ Set $\widehat{q^\varepsilon}(\xi) := \mathbf{t}_M^\varepsilon(\xi)$ and compute the inverse Fourier transform to obtain q^ε.
Step 3$^\varepsilon$ Solve the boundary value problem

$$\begin{aligned} (-\Delta + q^\varepsilon)(\gamma^\varepsilon)^{1/2} &= 0 & \text{in } \Omega, \\ (\gamma^\varepsilon)^{1/2} &= 1 & \text{on } \partial\Omega. \end{aligned} \tag{3}$$

and extract γ^ε. Set $\mathcal{R}_{M(\varepsilon)}\Lambda_\gamma := \gamma^\varepsilon$.
Admissible $\zeta(\xi)$ is here meant in the sense of [3, eq. 9]

$$\zeta(\xi) \in \{\zeta \in \mathbb{C}^3 \mid \zeta \cdot \zeta = 0, (\zeta + \xi) \cdot (\zeta + \xi) = 0\}. \tag{4}$$

Note ψ_ζ^ε is recovered from a boundary integral equation [4].

3 Computational methods

We simulate stroke data following a 2D experiment [5] assuming $\Omega = B(0,1)$ with a constant background $\gamma_b = 1$.
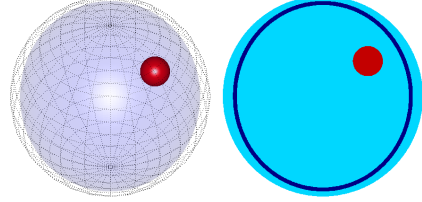
Figure 1: Phantom and cross-section ($z = 0$) of a hemorrhagic stroke modelled by a ball inclusion in $(0.45, 0.35, 0)$ of radius 0.15 and $\gamma = 3$ and a skull ellipsoid of width 0.04 and $\gamma = 0.2$.

We simulate Λ_γ from the phantom in Figure 1 using a boundary element method for piecewise constant inclusions [3]. To test the regularizing behavior of the method we perturb Λ_γ by adding Gaussian noise to each element of its matrix representation. The reconstruction method uses the implementation presented in [3]. Although the reconstruction method suggests we should pick $|\zeta(\xi)|$ fixed to the truncation radius M, in practice we can choose it minimally in the admissible set (4) for each ξ.

4 Results

Figure 2 shows the regularizing behavior of the method in practice. As the noise level decreases the truncation radius increases and the reconstruction improves.
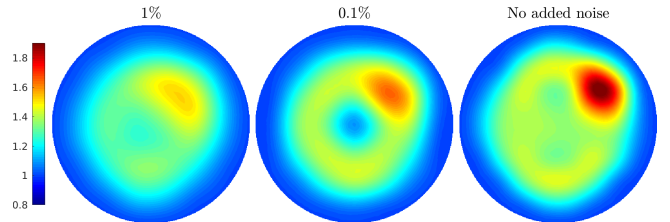
Figure 2: Left-to-right shows cross-sections ($z = 0$) of reconstructions with the method on data with 1%, 0.1% and 0% added noise. $|\zeta(\xi)|$ is minimal in the admissible set and M is chosen optimally by visual inspection resulting in $M = 9, 9.7, 12$.

The method works in simulated practice on piecewise constant inclusions. This experiment concludes feasibility of hemorrahagic stroke detection with the suggested direct reconstruction method.

5 Acknowledgements

References

[1] K Knudsen, A K Rasmussen (In submission), 2021
[2] K Knudsen, M Lassas, J Mueller, S Siltanen *Inverse Probl. Imaging*, 3:599–624, 2009
[3] F Delbary, K Knudsen *Inverse Probl. Imaging*, 8:991–1012, 2014
[4] A Nachman *Ann. of Math. (2)*, 128:531–576, 1988
[5] J Agnelli, A Çöl, M Lassas, R Murthy, M Santacesaria, S Siltanen *Inverse Problems*, 36:115008 (26pp), 2020

Modelling instrument admittances with EIDORS

Andy Adler[1]

[1]Systems and Computer Engineering, Carleton University, Ottawa, Canada

Abstract: Modelling of EIT instruments is important for accurate image reconstruction. This abstract explains how this can be done with EIDORS.

1 Introduction

Modelling of hardware imperfections in EIT has seen relatively little work. Systems have offsets, mismatched gains and crosstalk between channels. Many of these can be expressed as a linear correction to the sensitivity, **J**. When a good model of the specific hardware is available the corrected **J** can be used to improve reconstructing images [2].

2 Methods

Since the finite-element method's (FEM) system matrix represents the admittivity between nodes, additional admittances can be added directy to the system matrix (Fig 1). A new EIDORS[1] function `system_mat_instrument` is available to help form such a system matrix, and used as follows:

```
fmdl = fem_model( ... );
fmdl.system_mat = @system_mat_instrument;
fmdl.system_mat_instrument.connect_list = c_list;
```

where `c_list` describes additional admittances and nodes. It is hoped that this decription and new function helps users build improved models of EIT systems.

References

[1] A Adler, WRB Lionheart, *Physiol Meas*, 27:S25–S42, 2006
[2] AE Hartinger *et al* IEEE T Biomed Eng 56:369–377, 2008
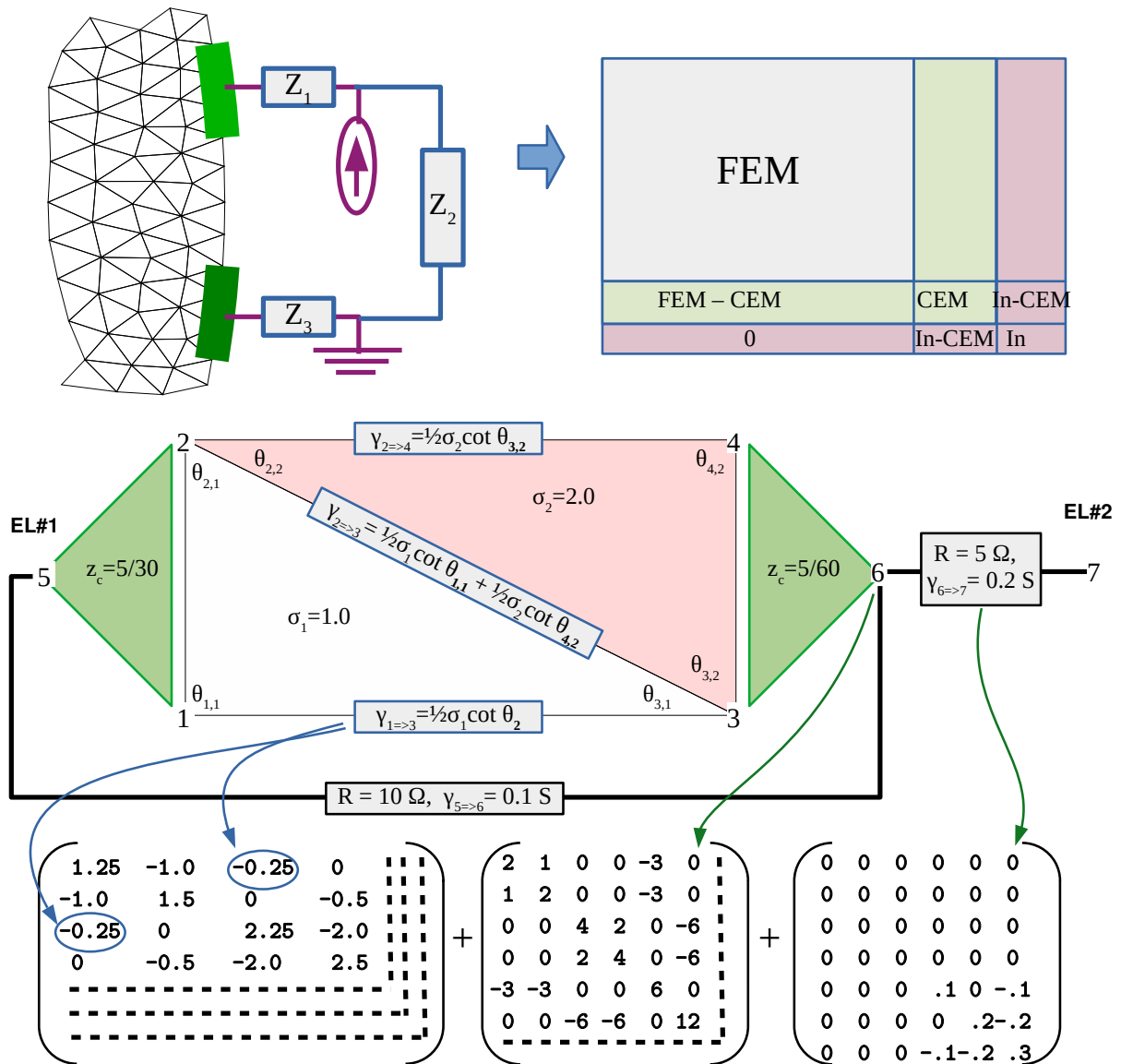
Figure 1: Incorporation of instrument models into a FEM, where the stiffness matrix (upper right) has additional nodes for complete electrode models (CEM) and instrument admittances. The lower figure shows a two-element FEM with two CEM electrodes and two additional admittances, and the formulation of the system matrix as a function of each component.

EIT Electrode Quality Assessment and Data Rejection

Mark Campbell[1] and Andy Adler[1]

[1]Department of Systems and Computer Engineering, Carleton University, Ottawa, Canada, `markacampbell@sce.carleton.ca`

Abstract: EIT images are often impaired by low-quality data due to poor electrode connections. We present an electrode quality assessment and data rejection (EQADR) algorithm to allow automatic detection and removal of the contribution of noisy measurements based on user-specified parameters.

1 Introduction

Sophisticated methods for removing the contribution of noisy measurements to the image reconstruction matrix have been developed [1] and optimized [2], which are effective at artifact removal. However, identifying which electrodes or measurements need to be removed remains a manual and time-consuming process. This paper presents an automated approach for electrode quality assessment, followed by the data rejection method developed by Adler and Mamatjan. This algorithm is designed to be used with data acquired by Sentec EIT systems.

Measurement quality is judged using the in-phase (I) and quadrature (Q) components of the EIT voltage measurements. A measurement is deemed erroneous if it exceeds the measuring capacity of the EIT hardware (falling on the boundary of the IQ plot), or if it has a negative I component (figure 1). Each electrode and measurement pair is given a score based on the proportion of total measurements that were erroneous, ranging from 0 - 1. The reciprocity of EIT measurements can lead to a single faulty electrode causing the other two electrodes with which it pairs (its "partners") to also appear faulty. The contribution of electrode reciprocity to the scores is resolved to yield the final data quality scores by the method shown in this pseudocode:

```
for each of the i electrodes:
    find the electrodes p₁ and p₂ that pair with electrode i.
    for each of the pᵢ partners of i:
        find the partner pᵢₚ of pᵢ that is not i.
        if the score of i >= to the combined scores of pᵢ and pᵢₚ,
            pᵢ is not noisy. Set the score of pᵢ to that of pᵢₚ.
```

The user may specify whether rejection is performed on a per-electrode or per-measurement basis, what the maximum acceptable number of rejected electrodes or measurement is, and the maximum acceptable score an accepted electrode or measurement may have. Rejection starts with the worst measurement or electrode, then proceeds until no more data groupings are higher than threshold, or until the maximum number of rejections occurs. The threshold parameter allows the user to tune the true positive and false positive rates for data rejection. The EQADR source code ia available here: `sf.net/p/eidors3d/code/HEAD/tree/trunk/dev/eqadr`.

2 Methods

3D EIT data was collected from a human subject with 2 rings of 16 electrodes separated by 6 cm with a skip-4 measurement and stimulation pattern. Tidal images were reconstructed with EIDORS[3] using the GREIT algorithm[4] for the plane at 3 cm with and without EQADR, and a noise factor of 2. EQADR was set to the electrode rejection mode, with a maximum number of 6 rejected electrodes, and a rejection score of 0.2 or higher.

3 Results and Discussion

EQADR identified and rejected 5 electrodes, whose measurements are shown by the red markers in figure 1.
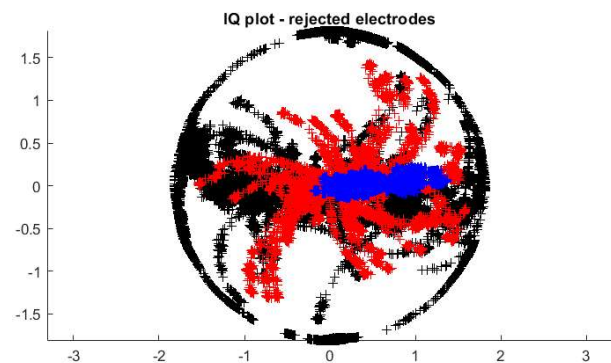
Figure 1: IQ plot of EIT measurements for the sample recording. All data was plotted in black. Noisy measurements identified by EQADR was plotted in red. Measurements from electrodes more than 2 positions away from the simulating electrodes were then plotted in blue.

The reconstructed images in figure 2 show that EQADR was effetive at reducing the appearance of artifacts in the center and boundary of the image and produced lung boundaries that were more defined than without compensation.
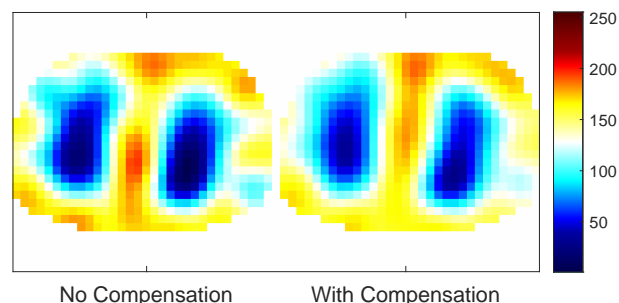
Figure 2: Reconstructed images without EQADR (left) and with EQADR (right)

References

[1] A Adler *Physiol Meas*, 25:227–238, 2004
[2] Y Mamatjan, P Gaggero, B Müller, B Grychtol, A Adler *Conf 36th CMBES*, 2013
[3] A Adler, WRB Lionheart *Physiol Meas*, 27:S25–S42, 2006
[4] B Grychtol, B Müller, A Adler *Physiol Meas*, 37:785–800, 2016

3D Direct CGO-based EIT Reconstructions on Ellipsoidal Domains

Peter A. Muller[1], Sarah J. Hamilton[2], David Isaacson[3], Ville Kolehmainen[4], Jussi Toivanen[4]

[1]Mathematics & Statistics, Villanova University, peter.muller@villanova.edu
[2]Mathematical and Statistical Sciences, Marquette University
[3]Mathematical Sciences, Rensselaer Polytechnic Institute
[4]Applied Physics, University of Eastern Finland

Abstract: This works extends 3D CGO-based absolute image reconstruction beyond boundary continuum data. Here, electrode voltage data is simulated using FEM with CEM boundary conditions and noise is introduced. The 3D CGO reconstruction algorithms provide an avenue for fast ($\sim$5 sec/image) absolute 3D EIT image reconstruction.

1 Introduction

Electrical impedance tomography (EIT) is a viable candidate for many biomedical imaging applications. As such, the ability to reconstruct images from 3D domains is ideal. Direct reconstruction methods based on complex geometrical optics (CGO) solutions offer a fast method for reconstructing internal conductivities, but have mostly been studied and implemented in 2D. Advances of CGO-based reconstruction methods to 3D have relied on continuum data from the entire boundary [1, 2] or time-difference imaging with experimental data. This work presents both the $\mathbf{t^{exp}}$ method, [3], and Calderón's method, [4], adapted to reconstruct absolute images from complete electrode model (CEM) data to better match the reality of biomedical applications. The methods presented here were first described in [5] for spherical domains and are now extended to ellipsoidal domains.

2 Methods

2.1 Electrode Data Simulation

Electrode data was simulated on ellipsoidal domains with randomly assigned axis lengths with 64 electrodes around the boundary and pairwise adjacent current patterns were applied. Each domain had 1-5 ellipsoidal targets and with randomly assigned sizes and conductivities. A FEM forward solver for the CEM boundary conditions was used to simulate the electrode data from each. After the simulated voltages were collected, 0.1% relative noise was added to them. The Dirichlet-to-Neumann (DN) maps, Λ_σ and Λ_1, from target $\sigma(x)$ and a noiseless constant background of 1, are then formed for use in each reconstruction method.

2.2 Calderón's method

Calderón's method, [4], linearizes the problem by assuming a constant background conductivity plus a small perturbation, $\sigma(x) = \sigma_b + \delta\sigma(x)$. The perturbation is reconstructed by an inverse Fourier transform of a function, $\hat{F}(z)$, that depends on the DN maps. The method is summarized by

$$(\Lambda_\sigma, \Lambda_1) \xrightarrow{1} \hat{F}(z) \xrightarrow{2} \delta\sigma^{\text{CAL}} \xrightarrow{3} \sigma^{\text{CAL}}, \qquad (1)$$

and more details and the numerical implementation are described in [5]. The middle column of Figure 1 shows cross-sections of a sample Calderón reconstruction.

2.3 $\mathbf{t^{exp}}$ method

The $\mathbf{t^{exp}}$ method also uses the DN maps Λ_σ and Λ_1 to form an approximation to the non-physical scattering transform

$\mathbf{t^{exp}}$, which is a nonlinear Fourier transform of $q(x) = \Delta\sqrt{\sigma(x)}/\sqrt{\sigma(x)}$. Recovering $\sigma(x)$ from $q(x)$ then requires solving that PDE. The method is summarized by

$$(\Lambda_\sigma, \Lambda_1) \xrightarrow{1} \mathbf{t^{exp}}(\xi, \zeta) \xrightarrow{2} \mathbf{q^{exp}} \xrightarrow{3} \sigma^{\text{exp}}, \qquad (2)$$

and again more details and the numerical implementation are described in [5]. The right column of Figure 1 shows cross-sections of a sample $\mathbf{t^{exp}}$ reconstruction.

3 Conclusions

Before optimizing the algorithms for speed, they are able to reconstruct absolute images at roughly 5 seconds per image. In addition, both methods are seen to handle simulated noisy electrode data with relatively low localization error and decent dynamic ranges.
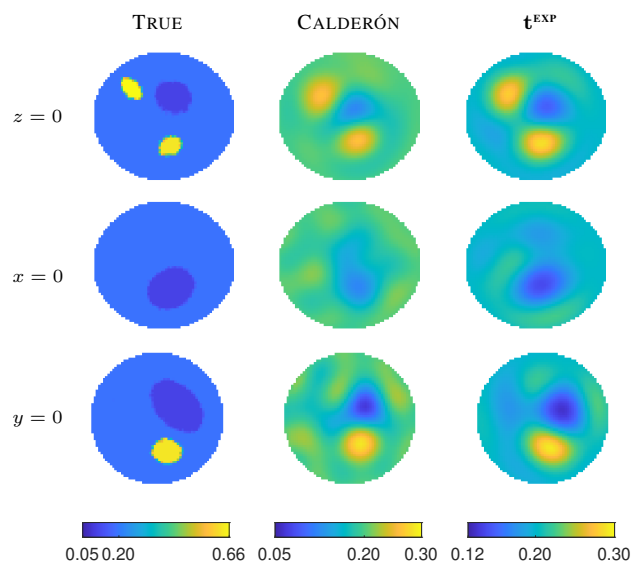
Figure 1: Cross-sections of Calderón and $\mathbf{t^{exp}}$ images compared to the truth for 0.1% noisy CEM voltage data. The colorbars for each column indicate the minimum, approximated background, and maximum conductivities.

4 Acknowledgements

References

[1] J Bikowski, K Knudsen, JL Mueller. *Inv Prob* **27**:19pp, 2011
[2] F Delbary, K Knudsen. *Inv Prob and Imag* **8**(4):991–1012, 2014
[3] AI Nachman. *Ann Math* **128**:531–576, 1988
[4] AP Calderón. In *Sem Num An and Appl to Cont Phys*, 65–73. Soc. Brasil. Mat., Rio de Janeiro, 1980
[5] SJ Hamilton, D Isaacson, V Kolehmainen, PA Muller, J Toivanen, PF Bray. *Inv Prob and Imag* 2021 (To Appear)

Session 9: Impedance Spectroscopy and Bioimpedance

In vivo Conductivity Tensor Images of Human Brain

Nitish Katoch[1], Bup Kyung Choi[1], Jin Woong Kim[2], Hyung Joong Kim[1] and Eung Je Woo[1]

[1]Department of Biomedical Engineering, Kyung Hee University, Seoul, Korea
[2]Department of Radiology, Chosun University College of Medicine, Gwangju, Korea

Abstract: Macroscopic conductivity of biological tissue at low frequency may exhibit anisotropy related with its structural directionality. Imaging of conductivity distributions inside the human body requires probing it by externally injecting conduction currents or inducing eddy currents. Here we propose a novel method to reconstruct conductivity tensor images using an MRI scanner without any current injection.

1 Introduction

Recently developed magnetic resonance (MR)-based conductivity tensor imaging methods can provide information about tissue properties as well as anisotropy from the contrast mechanism, which reveals changes in ionic concentration and mobility in the cellular space and can be visualized using MRI. This study reports the results of an in-vivo human brain imaging experiment using the CTI method. Five normal human subjects were scanned with a spatial resolution of $1.87 \times 1.87 \times 4$ mm^3 using a clinical MR scanner without any induced electrical current.

2 Methods

Five healthy volunteers without a documented history of any disease were recruited (KHSIRB-16-033). The volunteers were 25.4 ±4.5 years old (3 male and 2 female). All participants were performed using a 3T clinical MRI scanner (Magnetom Trio A Tim, Siemens Medical Solution, Germany). The image of the conductivity tensor was reconstructed using the CTI formula [1]:

$$\mathbf{C} = \frac{\alpha \sigma_H}{\alpha d_e^w + (1-\alpha)d_i^w \beta} \mathbf{D}_e^w = \eta \mathbf{D}_e^w \qquad (1)$$

where σ_H is the high-frequency conductivity at the Larmor frequency, α is the extracellular volume fraction, β is the ion concentration ratio of intracellular and extracellular spaces, d_e^w and d_i^w are the extracellular and intracellular water diffusion coefficients, η is position-dependent scale factor and D_e^w is the extracellular water diffusion tensor. The multi-echo spin-echo pulse sequence with multiple refocusing pulses was adopted to obtain the high-frequency conductivity (σ_H).

The imaging parameters were as follows: TR/TE = 1500/15 ms, number of echoes = 6, NEX = 5, slice thickness = 4 mm, number of slices = 5, matrix size = 128×128, and FOV = 240×240 mm^2. Multi-b diffusion weighted imaging data sets were obtained using the single-shot spin-echo echo-planar-imaging pulse sequence to calculate α, d_e^w, d_i^w, and D_e^w. The number of directions of the diffusion-weighting gradients was 15 with 15 b-values from 0 to 5000 s/mm^2. TR/TE = 2000/70 ms, and acquisition matrix = 64×64 which then extended to 128×128 for subsequent data processing steps. Other parameters were similar with multi-echo spin-echo imaging. An additional conventional T2 weighted scan of 2 minutes was also acquired for anatomical reference. The parameter β is set to the value of 0.41 as suggested in [1].
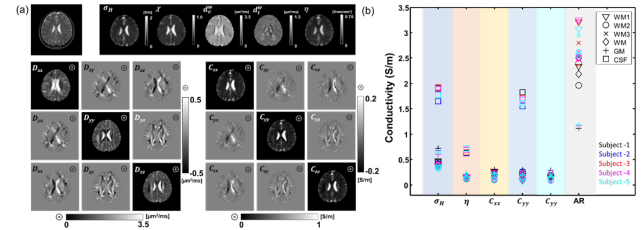
Figure 1: (a) In vivo CTI images of one human brain subject. Image of the T2-weighted high-frequency conductivity σ_H, extracellular volume fraction α, extracellular water diffusion coefficient d_e^w, intracellular water diffusion coefficient d_i^w and scale factor η between the conductivity tensor and the water diffusion tensor. **(a)** Quantitative analysis of measured conductivity values from all five subjects including their anisotropic ratio (ARs).

2.1 Results

Figure 1(a) illustrates the reconstructed CTI images of the brain from one subject using eq. (1). The recovered conductivity values of three different brain tissues including the white matter (WM), gray matter (GM), and cerebrospinal fluid (CSF) are shown in Fig. 1(b) for five subjects. In WM regions, conductivity values varied from 0.08 to 0.27 S/m. In GM regions, the values were between 0.60 to 0.72 S/m. The low-frequency conductivity of the isotropic CSF regions ranged from 1.55 to 1.82 S/m whereas its high-frequency conductivity values were in the range of 1.65 to 1.90 S/m. The ARs of the WM regions had much larger values of 1.96 to 3.25 compared with those of the gray matter regions.

3 Conclusions

Unlike other low-frequency conductivity imaging methods of MREIT and DT-MREIT [2,3], CTI does not require injecting currents into the imaging subject. This allows CTI to be readily applicable to in vivo human imaging studies. Without adding any special hardware, CTI can be implemented in a clinical MRI scanner for disease diagnosis and volume conduction modelling.

4 Acknowledgments

References

[1] SZK Sajib, OI Kwon, HJ Kim & EJ Woo *BEL*, s13534, 2018
[2] M Chauhan, A Indahlastari, & RJ Sadlier *IEEE TMI 37 966-976, 2018.*
[3] JK Seo & EJ Woo *IEEE TBME 61, 1390-9, 2014*

Imaging of Conductivity and Anisotropy in Muscle Tissues

Bup Kyung Choi[1], Nitish Katoch[1], Jin Woong Kim[2], Hyung Joong Kim[1], and Eung Je Woo[1]

[1]Department of Biomedical Engineering, Kyung Hee University, Seoul, Korea
[2]Department of Radiology, Chosun University College of Medicine, Gwangju, Korea

Abstract: High-resolution images of muscle tissues using conductivity tensor imaging (CTI) performed to validate its in vivo usefulness. The low- and high-frequency conductivity of muscle tissues obtained from the CTI and compared those with in vitro measurement by the impedance analyser. The anisotropy of the tissue was quantified using the anisotropy ratio (AR).

1 Introduction

Muscle is highly anisotropic because an applied current flows more easily along muscle fibers than across the fibers. Some clinical studies have suggested that the anisotropy of muscle may be beneficial for distinguishing between neurogenic and myopathic injuries and may be used as an indicator of disease progression. [1] We image the conductivity tensor distribution of anisotropic muscle tissues using a phantom with bovine muscle.

2 Methods

2.1 Preparation of muscle phantom

We designed two different muscles and agar, as shown in Fig. 1(a). The phantom consisted of an acrylic cylinder with a diameter of 50 mm and a height of 90 mm. Two resected bovine muscle blocks, each with a volume of $10 \times 10 \times 10$ mm^3, were positioned in the center of the phantom such that the muscle fibers were perpendicular to each other. *In vitro* measurements of the conductivity spectra in all muscle blocks were performed using an impedance analyzer to support the imaging experiment.

2.2 CTI experiment

The phantom was placed inside the bore of a 9.4T MRI scanner (Agilent Technologies, Santa Clara, CA, USA) and performed with a single channel body coil. The imaging parameters of multi-echo spin-echo were as follows: repetition time (TR)/echo time (TE) = 1500/15, 30, 45, 60, 75, 90 ms (6 echoes), number of excitations (NEX) = 5, and imaging time = 16 min. The imaging parameters of single-shot spin-echo echo-planar were as follows: TR/TE = 1800/39 ms, NEX = 2, and imaging time = 5 min. Diffusion weighting gradients was done in 12 directions with 13 b-values (0 to 3500 s/mm^2).

2.3 Conductivity tensor reconstruction

Conductivity tensor images of the muscle phantom were reconstructed using the MRCI toolbox (Sajib, 2017) with the following formula:

$$\mathbf{C} = \frac{\alpha \sigma_H}{\alpha d_e^w + (1-\alpha) d_i^w \beta} \mathbf{D}_e^w = \eta \mathbf{D}_e^w \qquad (1)$$

Detailed image reconstruction of the conductivity tensor was followed from the work of Katoch *et al.* [2]
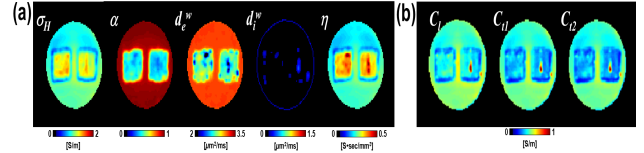
Figure 1: CTI results of bovine muscle tissues phantom

3 Conclusions

Figure 2 and Table 1 show the CTI analysis of bovine muscle tissues in the phantom. The conductivities of bovine A and B were higher than that of agar, which was designed to have a conductivity of 0.3 S/m (Fig. 2(b) and Table I). There was no clear difference in conductivity between the two bovine muscles (Fig. 2(c) and Table I). Meanwhile, the conductivity had a higher value along the fiber direction that was the longitudinal direction. Since the agar was not anisotropic, the conductivity tensor was similar in all directions. (Fig. 2(d-f) The anisotropy ratio was higher in the bovine muscles than in agar. (Table 1)
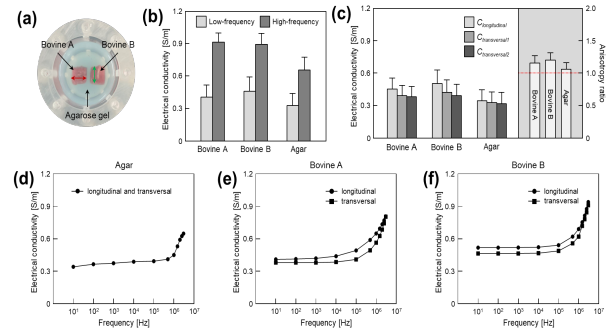
Figure 2: Analysis of CTI results of muscle phantom.

4 Acknowledgements

References

[1] K. Sogawa, H. Nodera, N. Takamatsu, A. Mori, H. Yamazaki, Y. Shimatani, Y. Izumi, and R. Kaji, *Radiology* 283:No2, 2017.

[2] N. Katoch, B. K. Choi, S. Z. K Sajib, E. A. Lee, H. J. Kim, O. I. Kwon and E. J. Woo *IEEE Trans. Med. Imaging* 38:1569-1577,2017

Table 1: Measurement of the isotropic conductivity, conductivity tensor, and anisotropy ratio (AR) of muscle tissues in the phantom

	Conductivity [S/m]		Conductivity tensor [S/m]			AR
	Low-freq.	High-freq.	C_l	C_{t1}	C_{t2}	
Bovine A	0.41 ± 0.11	0.92 ± 0.08	0.46 ± 0.10	0.40 ± 0.09	0.39 ± 0.09	1.17
Bovine B	0.46 ± 0.13	0.90 ± 0.10	0.51 ± 0.12	0.43 ± 0.11	0.40 ± 0.10	1.21
Agar	0.33 ± 0.11	0.66 ± 0.12	0.35 ± 0.10	0.33 ± 0.10	0.32 ± 0.11	1.07

EIT as a non-destructive method for evaluating cell viability

Marilisa Cortesi[1], Joseph Lovecchio[1], Roberta Ramilli[1], Andrea Samoré[1], Mariana Ionita[2], Emanuele Giordano[1], Marco Crescentini[1]

[1]University of Bologna, `marilisa.cortesi2@unibo.it`
[2]University Politehnica of Bucharest

Abstract: The study of cell viability in 3D cell cultures generally relies on destructive methods. To solve this issue, we have developed an EIT system capable of monitoring this and other variables of interest for *in-vitro* cultures. We here show an initial experimental validation of the proposed method and its comparison with a standard approach.

1 Introduction

To enable the long-term, non-destructive monitoring of cell viability in 3D cell cultures, we here present an hardware/software system (HSS) based on EIT. We previously developed this setup to quantify mineralization in artificial bone substitutes [1].

In this work, aerogel scaffolds were seeded with populations of cancer cells and maintained for a week. Cell density was evaluated at 3 and 7 days post seeding with both the proposed HSS and a standard method based on the evaluation of cell metabolism (Presto Blue).

Our results, albeit preliminar, show the potential of this setup for the multiparametric monitoring of scaffold-based 3D cell cultures.

2 Methods

2.1 Hardware/software system

The HSS used in this work combines an EIT setup, based on an impedance analyser, a custom connection board and sample holder fitted with 8 electrodes, and a software platform for the reconstruction of conductivity maps and the simulation of scaffold impedance changes due to cell behaviour. For this study, the reconstruction algorithm presented in [2] was used. It minimises a non-convex function based on the alternating direction method of multipliers and has been shown *in-silico* to yield more accurate reconstructions.

2.2 3D cell culture and experiments

Chitosan-Gelatin-Genipin (CGG) scaffolds were realised as in [3]. A total of 100K MDA-MB-231 cells, a highly aggressive breast cancer cell line, was seeded on top of each dried scaffold. Cultures were maintained in standard conditions (37°C and 5% CO_2) throughout the experiment. Measurements were conducted as detailed in [1], using an opposite stimulation pattern and an adjacent measuring one. In all experiments the measurement chamber was filled with 1 ml of Hepes buffer and the reconstructions were obtained considering a scaffold devoid of cells as reference.

3 Results

3.1 Conductivity time course

Figure 1 shows the conductivity maps and the corresponding quantification of $\Delta\sigma$ within the scaffold region, at the considered time points.

This result shows how the addition of the cells induces an increase in scaffold conductivity, due to the ions present in the cell culture media within the scaffold, while cell growth causes a reduction in this variable, as shown in [4]. The high uniformity of the reconstructed scaffold suggests a regular cell distribution throughout the structure.
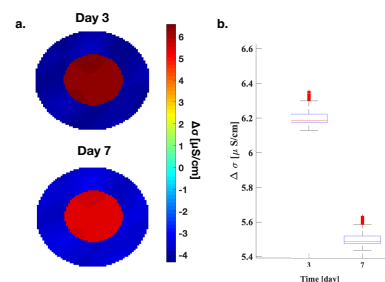
Figure 1: a. Reconstructed conductivity maps. **b.** $\Delta\sigma$ quantification within the scaffold region.

3.2 Comparison with Presto Blue

To verify the accuracy of these results we compared them with those of a test, commonly used to estimate the number of living cells, in which the signal is proportional to the number of cells. As we can see from Figure 2, the two methods provide inversely proportional results and show a qualitative agreement.
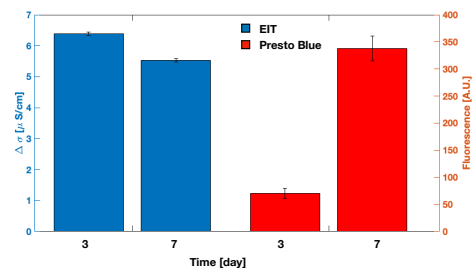
Figure 2: Comparison of the average $\Delta\sigma$ in the scaffold region and a standard viability assay.

4 Conclusions

The two measurements are coherent and in line with previous reports. The lower resolution of EIT warrants further analysis, which might results in upgrades of the HSS.

5 Acknowledgements

References

[1] M Cortesi, A Samoré, J Lovecchio, R Ramilli, M Tartagni, E Giordano, M Crescentini *Physiol Meas*, accepted, 2021

[2] M Huska, D Lazzaro, S Morigi, A Samoré, G Scrivanti *J.Sci.Comput.*, 84:1–29, 2020

[3] S Dinescu, M Ionita, AM Pandele, B Galateanu, H Iovu, A Ardelean, M Costache, and A Hermenean *BIO-MED.MATER.ENG*, 24:2249-2256, 2014

[4] H Wu, W Zhou, Y Yang, J Jia, P Bagnaninchi *Materials*, 11(6):930, 2018

Optimisation of the temporal dispersion model in unmyelinated nerves based on experimental study in subdiaphragmatic nerve of the pig

Ilya Tarotin[1], Svetlana Mastitskaya[1], Enrico Ravagli[1], Justin Perkins[2], Kirill Aristovich[1] and David Holder[1]

[1]Medical Physics and Biomedical Engineering, University College London, UK, ilya.tarotin@ucl.ac.uk
[2]Royal Veterinary College, Hertfordshire, UK

Abstract: Fast neural EIT could image neural activity within peripheral nerve but has not been employed for unmyelinated nerve where dispersion prevents a measurable impedance change at distances >4cm. Based on obtained experimental data, the dispersion model was modified and predicted SNR>2 at 20 cm from the onset.

1 Introduction

Variability in diameters and conduction velocities of C fibres in unmyelinated nerves causes dispersion of the compound action potential (CAP) which prevents imaging the activity at >4 cm from the site of stimulation [1]. Recent simulation results demonstrated the theoretical feasibility of recovering impedance changes (dZ) even at distances from stimulation where compound action potentials (CAPs) are not present [2].

The purpose of this study was to achieve dZ measurement at up to 20 cm from the stimulus in experimental setting. For this, a new stimulation and signal processing paradigm based on stimulus trains and band-pass filtering around the whole trains was used [2]. Compared to the coherent spike averaging, usage of trains could significantly reduce the noise and increase SNR in the measurements.

2 Methods

Pig subdiaphragmatic nerves which closely resemble those of the human [3], resected from terminally anaesthetized pigs were held in an organ bath perfusion chamber filled with oxygenated saline solution kept at ˜30 °C. Three silicone rubber cuffs with 6 radially arranged electrodes each were placed around the nerve 3, 15 & 20cm from a cuff for electrical stimulation (Fig. 1a). The study was divided into 3 stages: **1)** dZ and CAPs were recorded with respect to the electrode on the last cuff using continuous stimulation with f_{stim}= 2Hz, I_{stim} = 20 mA, PW=50 µs, f_{AC}= 0.4-2 kHz, I_{AC}= 200-300 µA (N=18). The model [2] was modified to match the measurements. **2)** The previously determined optimal stimulation paradigm for recording dZ far from onset [2] (10Hz trains, 24 stimuli/train, 3s rest between trains) was applied to the 2 nerves to test their long-term survival. The paradigm was modified and predictions for SNR at <50 cm from stimulus were obtained. **3)** (In progress) The updated paradigm was applied to N=15 nerves to record dZ at up to 20 cm from the onset, where CAP is not visible.

3 Results

1) Based on the CAP and dZ measurements (Fig. 1b), the number and type of the fibres and their CV were changed in the model to match the experiments (Table 1).

2) To achieve long-term survival of the nerve subjected to trains of stimuli, resting time between the trains was increased to 5s and the number of pulses per train decreased to 6; this improved the longevity of the nerve from ~0.5 to >10 hours (Table 1). With the updated paradigm and model parameters, measurable dZ was predicted at up to 20 cm from the onset with SNR=1.9±0.8 if averaging with 10Hz trains for 30 minutes (Fig 1c).

Table 1 Modification of model parameters based on experiments

Parameter	Previous [2]	Modified
C fibres No., CV	5K, (0.6±0.07)m/s	40K, (0.8±0.4)m/s
B fibres No., CV	–	200, (10±2) m/s
Time b/w trains	3 s	5 s
No. pulses/train	24	6
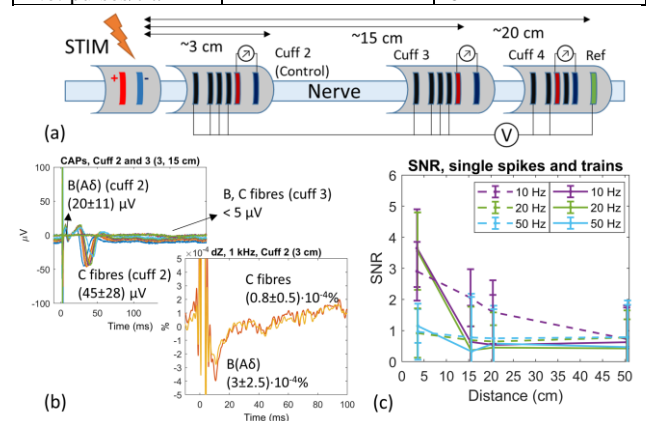
Figure 1: (a) Experimental setup; (b) Example of CAPs and dZ recordings at cuffs 2 and 3, colours are different cuff channels along the nerve; (c) SNR for single spikes (full) and trains (dashed) simulated with the modified model (30 mins averaging)

4 Conclusions

The conducted experiments allowed matching the previously designed model of temporal dispersion with experimental data. The modified model predicted feasibility of dZ measurement at distances up to 20 cm from the stimulus where no CAP is visible. The work in progress is conduction of the additional experiments and processing of the experimental data to validate this approach and record dZ where CAP is dispersed.

5 Acknowledgements

References

[1] I Tarotin et al. *Physiol meas.* 40: 034001, 2019
[2] I Tarotin et al. *The FASEB Journal* 34(S1), 1–1
[3] M Settell et al. *J Neural Eng* 17(2), 02602

Electrodeless Conductivity Tensor Imaging and its Validation using Giant Vesicle Suspension

Nitish Katoch[1], Bup Kyung Choi[1], Jin Woong Kim[2], Hyung Joong Kim[1] and Eung Je Woo[1]

[1]Department of Biomedical Engineering, Kyung Hee University, Seoul, Korea
[2]Department of Radiology, Chosun University College of Medicine, Gwangju, Korea

Abstract: Recently proposed MRI-based electrodeless conductivity tensor imaging method is tested on giant vesicle suspension phantom. Giant vesicles are cell-alike material with a thin insulating membrane. The measured conductivity values from the CTI method were compared with those measured using an impedance analyzer.

1 Introduction

The conductivity tensor imaging (CTI) method has been developed without injecting currents to recover conductivity tensor distribution in the human brain [1]. The fundamental concept of CTI is to extrapolate extracellular conductivity distribution from reconstructed conductivity information from the B1 phase of MRI. CTI requires B1 phase maps and microstructure maps from multi-b diffusion tensor images to calculate conductivity tensor distribution. Since the CTI technique could have potential in clinical application, a validation study has been deferred. In this study, a specially designed giant vesicle is used to experimentally validate the CTI technique. Giant vesicles are cell-like materials with thin insulating membranes and the giant vesicle suspension included both extracellular and intracellular spaces.

2 Methods

Giant vesicles dispersed in an aqueous solution were prepared as described by Moscho et al. [2]. The imaging phantom consists of three compartments and as shown in figure 1(A). The innermost compartment is giant vesicle suspension and the other two consist of EL #1 and EL #2.
A 9.4 T research MRI scanner was used with a single-channel mouse body coil. The high-frequency conductivity images were acquired using the multi-echo spin-echo sequence with an isotropic voxel resolution of 0.5 mm. The imaging parameters were as follows: TR/TE = 2200/22 ms, NEX = 5, FOV = 65 × 65 mm^2, slice thickness = 0.5 mm, FA = 90°, and image matrix size = 128×128. Diffusion-weighted MR imaging was separately performed using the single-shot spin-echo echo-planar-imaging sequence. The imaging parameters were as follows: TR/TE = 2000/70 ms, number of signal acquisitions = 2, other parameters were as same as the multi-echo spin-echo sequence. The number of directions of the diffusion-weighting gradients was 30 with 15 b-values. The electrical conductivity of all the electrolytes used in the study was measured using an impedance analyzer (SI1260A, AMETEK Inc., UK).

Figure 1: (A) T$_2$-weighted image, (B) Intermediate variable of conductivity tensor imaging (σ_H) high frequency conductivity, (α) extracellular volume fraction, (d_e^w), and (d_i^w) extra- and intracellular diffusion coefficient and (η) scale factor. (C) Conductivity spectra of giant vehicles and electrolytes. (D) Conductivity tensor images of experiment phantom.

2.1 Results

Figure 1(D) shows the reconstructed conductivity tensor images of giant vesicle suspension phantom calculated multiplying scale factor (η) to water diffusion tensors. The conductivity values of EL#1 and EL#2 at 10 Hz were 1.44 and 0.78 S/m., whereas using CTI the value was 1.45 and 0.85 S/m, respectively. The conductivity of the giant vesicle suspension using electrolyte #1 (1.44 S/m at 10 Hz) was 0.29 S/m at 10 Hz. The values of low-frequency conductivity tensor were 0.28, 0.30, and 0.29 S/m using CTI methods. The relative error was 1.1, 4.4, and 1.7% between impedance analyzers and the CTI method.

3 Conclusions

The effects of cell density, ion concentration, and mobility on the electrical conductivity could be observed from reconstructed CTI images [1]. The clinical usefulness of the method needs to be verified by future studies of human.

4 Acknowledgments

References

[1] A Mocho, O Orwar, BP Modi *PNAS*, 93:11443-11447,1996.
[2] SZK Sajib, OI Kwon, HJ Kim, EJ Woo *Biomedical Engineering letters*, 8:273-282, 2018.

Table 1: Mean and standard deviation values of the diagonal components of the conductivity tensor C and the intermediate variables of reconstruction using the CTI method. The mean ± SD values were computed from all pixels within each region.

Region	σ_H	α	d_e^w	d_i^w	η	C_{xx}	C_{yy}	C_{zz}
Giant Vesicle suspension	1.89 ± 0.02	0.13 ± 0.04	1.93 ± 0.12	0.98 ± 0.10	0.21 ± 0.04	0.29 ± 0.05	0.30 ± 0.07	0.29 ± 0.05
Electrolyte #1	1.86 ± 0.04	1.00 ± 0.02	2.90 ± 0.01	-	0.64 ± 0.01		1.45 ± 0.04	
Electrolyte #2	1.11 ± 0.04		2.85 ± 0.02		0.38 ±0.01		0.85 ± 0.03	

Measurement of the Left Atrium Appendage Electrical Conductivity with a Tetrapolar Probe over 0.1 Hz to 100 kHz

Hamza Benchakroun[1,2], Eoghan Dunne[2,3], Declan O'Loughlin[4], Martin O'Halloran[1,2]

[1]Electrical and Electronic Engineering, National University of Ireland Galway, Galway, Ireland.
[2]Translational Medical Device Laboratory, National University of Ireland Galway, Ireland.
[3] School of Medicine, National University of Ireland Galway, Ireland.
[4]Electronic and Electrical Engineering, Trinity College Dublin, Dublin, Ireland.
h.benchakroun1@nuigalway.ie

Abstract: This paper presents impedance measurements of the left atrium appendage using a tetrapolar probe from 0.1 Hz to 100 kHz. The results show that the conductivity of the left atrium appendage averages around 2.5 mS/cm, aligning with conductivities of cardiac muscle in the literature.

1 Introduction

Irreversible electroporation (IRE) is an ablation technique that alters the fundamental behaviour and connections of cells in a tissue using repetitive short duration, high voltage pulses [1]. This technique can be used for ablation of the left atrial appendage (LAA), therefore a treatment solution for atrial fibrillation (AF) [2], [3].

Electrical impedance tomography (EIT) is a low-cost, portable, and safe medical technology that can be used to monitor changes in conductivity over time [4]. The technology offers the potential to monitor the formation of a lesion during ablation of a tissue [5].

EIT can operate from the low Hz to low MHz [6]. The main operating frequency range of IRE, i.e., 0.1 Hz to 100 kHz [7]–[9], which overlaps with the EIT range. In this work, tissue measurements are captured over the frequency range of 0.1 Hz to 100 kHz to inform the development of both EIT and IRE devices.

The remainder of this paper is structured as follows: Section 2 describes the measurement set up and the tetrapolar probe used during the measurements; and Section 3 presents and discusses the results acquired from multiple *in vivo* experiments.

2 Methods

The acquisition of the complex impedance was performed using the methods described in [7] using a PGSTAT204 potentiostat/galvanostat with a tetrapolar probe. The probe was characterised experimentally and resulted in the cell constant of 0.032 m. The correlation coefficient between the characterisation data and the reference values in literature was 0.99 over the frequency range from 0.1 Hz to 100 kHz. The measurements were conducted on two bovine heart samples. The first sample was used to investigate the conductivity of the LAA epicardium and the endocardium with the membrane. The second sample was used to investigate the conductivities of the LAA endocardium without the membrane.

3 Results and Discussion

The acquired conductivities from the LAA regions are shown in Figure 1 along with conductivities of cardiac muscle from the literature [10].
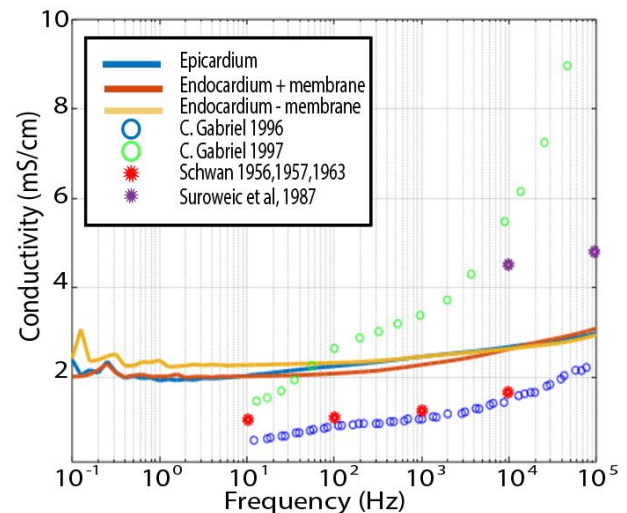
Figure 1: Plotted mean conductivities of the LAA along with the cardiac muscle data from literature for comparison [10].

The conductivities of the pericardium, and the endocardium with and without membrane of the LAA show similar behaviour and their conductivities average around 2.5 mS/cm over the frequency range 0.1 Hz to 100 kHz. The conductivity acquired from the two bovine heart samples are in good agreement with the range of conductivities for cardiac muscle found in the literature. These measurements and results can help inform future EIT imaging devices to monitor ablation of the LAA.

References

[1] D. C. Chang, J. A. Saunders, B. M. Chassy, and A. E. Sowers, Overview of Electroporation and Electrofusion Academic Press, San Diego, 1992.
[2] R. N. Doshi, 10.19102/icrm.2021.120105
[3] J. C. Weaver, Y. A. Chizmadzhev, 41 (1996) 135-160
[4] E. Dunne, A. Santorelli, B. McGinley, M. O. Halloran, G. Leader, E. Porter, *19th EIT*, Edinburgh, UK, Jun 2018.
[5] A. Bottiglieri, E. Dunne, B. McDermott, M. Cavagnaro, E. Porter, L. Farina, *14th EuCAP,* March 2020.
[6] D. S. Holder Electrical Impedance Tomography. Methods, History and Applications *CRC Press*, 2004.
[7] H. Benchakroun, D. O. Loughlin, N. Ištuk, M. O. Halloran, and A. La Gioia, *15th EuCAP 2021*, March 2021.
[8] R. E. Neal *et al.*, the Prostate, 10.1002/pros.22760
[9] N. Ištuk, A. La Gioia, H. Benchakroun, A. Lowery, *URSI GASS 2021,* Rome, Italy, March, 2021.
[10] C. Gabriel, 10.21236/ada303903 .

Impedance-optical Dual-modal Imaging for 3D Cell Culture

Zhe Liu[1] and Yunjie Yang[1]

[1]Agile Tomography Group, School of Engineering, The University of Edinburgh, Edinburgh, UK, y.yang@ed.ac.uk

Abstract: An impedance-optical dual-modal imaging and information fusion method is proposed to achieve quantitative 3D cell culture imaging. The effectiveness and robustness of the proposed method are verified by numerical simulation.

1 Introduction

Electrical Impedance Tomography (EIT) is a promising technique for non-destructive, label-free 3D cell culture monitoring [1]. However, the intrinsic low-resolution of EIT limits its wider adoption in this field [2, 3]. To improve EIT image quality, an impedance-optical dual-modal imaging framework is proposed to conduct quantitative 3D cell culture imaging. The framework consists of three components, i.e. a miniature impedance-optical sensor, guidance image processing algorithm and a deep learning model performing information fusion and image reconstruction. The network possesses good generalization ability, especially when an inaccurate mask is generated by the guidance image processing algorithm.

2 Methods

The proposed framework is shown in Fig. 1 and its working procedure is stated as follows. First, the miniature impedance-optical dual-modal sensor will simultaneously acquire a frame of voltage data and an RGB microscopic image (named the guidance image). Then, the guidance image will be converted into the binary mask image (named the mask) by the guidance image processing algorithm. Finally, the trained deep learning model will fuse the information from the voltage data and the mask image to generate a quality-improved EIT image. The simplified architecture of the proposed deep learning model is shown in Fig. 2. The function of the mask correction network is to correct the input mask image if it is not accurate, and the corrected mask image will be used as the input of the image reconstruction network whose function is to generate the ultimate EIT image. The bottom voltage feature extraction network is used to extract the latent information in the voltage data. In the reconstruction process, the information extracted from this subnetwork is shared by the mask correction network and the image reconstruction network and navigates these two subnetworks function properly.
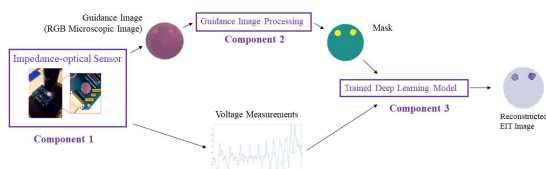
Figure 1: Schematic of impedance-optical dual-modal imaging framework.
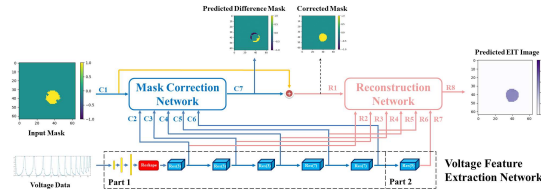
Figure 2: Simplified neural network for dual-modal EIT image reconstruction. The neural network requires the shape of the mask image is square. Therefore, pixels outside the inscribed circle are padded by zeros before feeding the mask image into the neural network, which also leads to square EIT image. Fig. 1 only display circular sensing area for both mask and EIT image.

3 Results

The proposed method is verified by numerical simulation. The results of mask correction operation are shown in Fig. 3 and the results of EIT reconstruction are shown in Fig. 4. The same rows in Fig. 3 and Fig. 4 correspond to the same phantom. EIT images adopt different colour bars from other types of images.
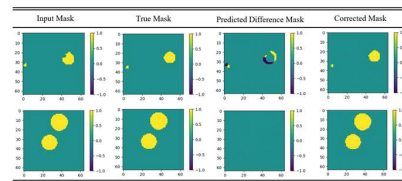
Figure 3: Mask Correction Results.
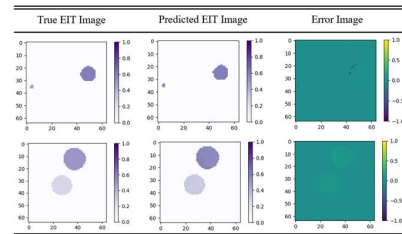
Figure 4: Image Reconstruction Results.

4 Conclusions

In this study, we combine EIT and microscopic imaging for quantitative EIT image reconstruction. The advantages of introducing another imaging modality into EIT inverse problem is verified by numerical simulation. The future work will extend the method to 3D imaging.

References

[1] Y. Yang, H. Wu, J. Jia, and P. O. Bagnaninchi, "Scaffold-based 3-d cell culture imaging using a miniature electrical impedance tomography sensor," in IEEE Sensors Journal, vol. 19, no. 20, pp. 9071-9080, 2019.

[2] R. H. Bayford, "Bioimpedance tomography (electrical impedance tomography)," *Annu. Rev. Biomed. Eng.,* vol. 8, pp. 63-91, 2006.

[3] P. Metherall, D. C. Barber, R. H. Smallwood, and B. H. Brown, "Three-dimensional electrical impedance tomography," *Nature,* vol. 380, no. 6574, pp. 509-512, 1996

Pressure Dependency of Conductivity Measurements: The Specific Case of the Lung

Niko Istuk[1,2], Hamza Benchakroun[1,2], Eoghan Dunne[1,2], Martin O'Halloran[1,2]

[1]Electrical and Electronic Engineering, National University of Ireland Galway, Galway, Ireland `niko.istuk@nuigalway.ie`
[2]Translational Medical Device Lab, National University of Ireland Galway, Galway, Ireland

Abstract: In this paper, we examined how the applied pressure influences the measurement of conductivity in lung tissue. We found that the conductivity of lung increases with increased pressure. The increase in conductivity can be explained by the air being pushed out of the lung under the applied pressure.

1 Introduction

The electrical conductivity of tissues at low frequencies is fundamental for medical electromagnetic applications, such as electrical impedance tomography. There are several studies in the literature reporting conductivity measurements of lung. However, knowledge of this data at frequencies below 100 kHz is limited due to measurement challenges. One of the challenges is the pressure dependency of the conductivity in soft tissue. Moqadam *et al.* [2] found that each type of tissue responds differently to compression, where the slopes of the conductivity-pressure plots differed between the tested tissues. Dodde *et al.* [1] explained the change in conductivity due to the applied pressure by changes to the electrolyte or fluid volume in the tissue. Under tissue compression, pressure gradients developed within the tissue and act to drive fluid out of both the intra- and extracellular spaces [1]. This results in decreased conductivity with added pressure intra- and extracellurar fluids contain electrolytes that mostly contribute to the overall conductivity of the tissue. Lung tissue is a specific case in that it is filled with air and by compressing the tissue, we also deflate the lung. Gabriel *et al.* [3] treated the inflated and the deflated lung separately, finding a lower conductivity for the inflated lung (0.042 S/m for inflated lung and 0.11 S/m for deflated lung). Given that air is much less conductive than the lung tissue, it is expected the conductivity increases as the air is expelled from the lung. This study aims to determine which one of the two effects, the increase in conductivity due to the air being expelled or the decrease in conductivity due to the liquid being expelled, is going to be more significant in impacting the conductivity

2 Methods

In this experiment, we performed the measurements on ovine lung that was acquired by the local abattoir. The lung was placed on a weighing scale under the probe. The weighing scale was zeroed before the probe made contact with the lung tissue. The probe was then brought into contact with the tissue and the pressure was monitored on the weighing scale (via applied force). We performed 10 measurements, changing the force (and consequently the pressure) from 1 N to 10 N. The acquisition of the complex impedance at five different frequencies (f = 10 Hz, 100 Hz, 1kHz, 10 kHz and 100 kHz) was performed using the methods described in [4] with a PGSTAT204 galvanostat (Metrohm Autolab B.V., Utrecht, The Netherlands) and a custom four-electrode probe.

Fig. 1 shows the results of the measurements at f = 1 kHz. The conductivity increases as the pressure is increasing. This can be explained by the fact that under the applied pressure, the air is pushed out of the lung. Since the air acts as a near perfect electric insulator, when it's pushed out of the lung, the increase in conductivity is expected. The same trend is observed at the other frequencies.
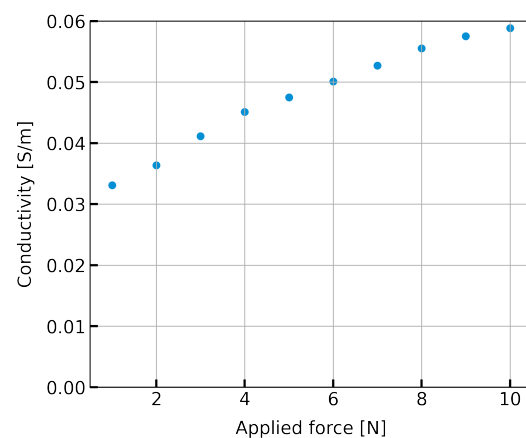
Figure 1: The measured conductivity of lung versus the applied pressure (f = 1 kHz). The conductivity increases as the pressure increases. This finding can be explained by the air being pushed out of the lung.

3 Conclusions

This study shows that lung tissue conductivity increases with the pressure. This is unlike other tissues for which the conductivity decreases. This effect is in contrast with the usual effect of decreasing conductivity with pressure due to the liquid being pushed out of the tissue The different behaviour can be explained by the fact that the conductivity of lung tissue depend on the amount of air in the tissue, which is not the case for other tissue types.

4 Acknowledgements

References

[1] R. E. Dodde, J. L. Bull, and A. J. Shih, Physiol. Meas., vol. 33, no. 6, pp. 1095–1109, Jun. 2012.

[2] S. M. Moqadam, P. Grewal, M. Shokoufi, and F. Golnaraghi, p. 12, 2015.

[3] C. Gabriel, A. Peyman, and E. H. Grant, Phys. Med. Biol., vol. 54, no. 16, pp. 4863–4878, Jul. 2009.

[4] H. Benchakroun, D. O'Loughlin, N. Ištuk, M. O'Halloran, and A. L. Gioia, in 2021 15th European Conference on Antennas and Propagation (EuCAP), Mar. 2021, pp. 1–5.

Session 10: Applications II

Improving Aortic Stent Sizing Through Integrated Impedance Measurements

Cristina Fiani[1], Kirill Aristovich[1] and James Avery[2]

[1]Medical Physics and Biomedical Engineering, University College London, UK, cristina.fiani.17@ucl.ac.uk
[2] The Hamlyn Centre, Imperial College London, UK

Abstract: Aortic stent sizing is a paramount step in Transcatheter Aortic Valve Replacement (TAVR). The extent to which impedance measurements can enable us to distinguish the size and shape of simplified balloon catheters was evaluated using an analytical approach and 3D EIT reconstructions. In simulations, the analytical approach outperformed the 3D reconstructions, enabling size and ellipticity to be distinguished within 1mV.

1   Introduction

Aortic stenosis is one of the most common heart valve diseases among the elderly over 65 years old [1]. The condition involves the obstruction of the left ventricle blood outflow; the aortic valve does not open properly, causing blood flow restriction. Patients with severe aortic stenosis have been recently treated with TVAR, aiming to insert a new aortic valve with a catheter [2]. Therefore, the prosthesis size selection relies on 2D or 3D imaging techniques which are shown to lack accuracy [3]. Poor sizing of the aortic stent assuming a circular aortic valve cross-section, leads to complications, including Paravalvular Leak (PVL) or the rupture of aortic walls [4].

Integrated impedance measurements and EIT, placing electrodes on the inner catheter may accurately determine the size and the shape of the balloon surface and, consequently, the aorta.

2   Methods

Balloons were assumed to be rigid and modelled as cylinders or elliptic cylinders, from the smallest possible diameter depending on the inner catheter up to 23mm with a step-size of 1mm and from 23 to 32mm with a step-size of 3mm. Elliptical balloons were kept with the minor axis as half the major axis. This allowed us to evaluate the shape and size distinguishability between the different models. Three typical TVAR catheter diameters, 9Fr (3mm), 14Fr (4.7mm) and 16Fr (5.3mm) were used with two rings of 8 or 16 electrodes, separated by 10mm.

The analytical approach was simply based on Ohm's law and the resistance formula to evaluate voltages obtained along the balloons. If we divide an elliptic cylinder into sectors and measure in a 90-degree sector (**fig. 1.a**), the voltages should increase from the major axis to the minor axis, as the sector area decreases.

For imaging, full EIT protocols were simulated in balloon catheter models with two rings of 8 electrodes. Absolute 3D images were reconstructed in larger cylindrical meshes using Gauss-Newton dual model iterative solver. To obtain the radius, we computed the polar coordinates of elements reconstructed in 12 sectors, with a threshold of 1/3, 1/2 and 2/3 of the maximum conductivity obtained.

3   Results

The difference between the voltages of the smallest sector and the biggest sector in the 90-degree sector (**fig 1.b**) reached 1mV at 17mm, 26mm and 29mm (9Fr, 14Fr, and 16Fr). The models' shape and size were still detectable after these limits by less than 1mV. However, 3D EIT reconstructions appeared to lack accuracy as the balloons' sizes increased (**fig. 1.c,d**). Detectability limits were defined at 9mm, 12mm and 12mm (9Fr, 14Fr, and 16Fr).
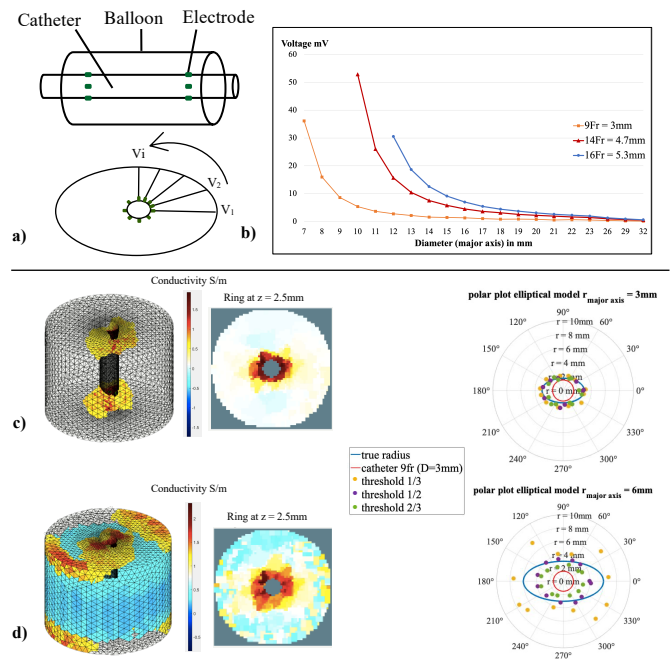
Figure 1: Analytical Approach a) Schematic of balloon with inner catheter and cross-section of elliptic cylinder divided into sectors. **b)** Difference between the voltage measurements of smallest sector in the 90-degree sector (67.5-90°) and of largest sector (0-22.5°) in elliptic cylinder models. **3D EIT Reconstructions. c)** Reconstructed elliptical model $D_{major\ axis}$ = 6mm 9Fr **d)** Reconstructed elliptical model $D_{major\ axis}$ = 12mm 9Fr. We can observe a higher spread in the 12mm model.

Conclusion

The analytical approach allowed us to distinguish the shape and size of all models. However, the detectability reached less than 1mV at 17mm, 26mm and 29mm (shape) and 16mm, 19mm and 20mm (size). Experimental validation is ongoing. Signal-to-noise ratio (SNR) and EIT reconstructions' optimisation will be further researched.

References

[1] B. Neal et al., J. Geriatr. Cardiol., 2016, DOI: 10.11909/j.issn.1671-5411.2016.12.004.
[2] E. Ferrari and L. von Segesser, Swiss Med Wkly, 2010, DOI: 10.4414/smw.2010.13127.
[3] A. M. Kasel et al., JCMG, 2013, DOI: 10.1016/j.jcmg.2012.12.005.
[4] N. K. Monigari and A. Agarwal, IntechOpen, 2019, DOI: 10.5772/intechopen.84909.

Magnitude and Regional Distribution of VQ Ratios in Anaesthetized Horses

Mark Campbell[1], Andy Adler[1], Ella Pittman[2], Manuel Martin-Flores[2], Joaquin Araos[2]

[1]Department of Systems and Computer Engineering, Carleton University, Ottawa, Canada, `markacampbell@sce.carleton.ca`
[2]Department of Clinical Sciences, College of Veterinary Medicine, Cornell University

Abstract: We evaluated the regional magnitude and distribution of ventilation / perfusion ($\dot{V}/Q$) ratios in anaesthetized horses at 25 and 50 minutes and found that the images were consistent across time. This suggests that the technique is stable for studying long-term $\dot{V}/Q$ ratio changes during anaesthesia.

1 Introduction

The regional $\dot{V}/Q$ ratio is the main determinant of gas exchange. General anaesthesia significantly impairs gas exchange in horses[2]. We were motivated to assess the magnitude and distribution of $\dot{V}/Q$ ratios over time in horses undergoing anaesthesia in dorsal recumbency.

2 Methods

Four supine recumbent, mechanically ventilated horses undergoing bilateral stifle arthroscopy were included. A custom-made EIT belt was placed prior to surgery. EIT recordings were obtained 25 (T25) and 50 (T50) minutes after anaesthesia induction. At each measurement, a bolus (100 mL) of 7.2% sodium chloride was injected IV. EIT data was collected using 1 ring of 32 electrodes. Images were reconstructed in MATLAB2019a using the EIDORS software package[1] and a horse-shaped forward model. Image elements were reconstructed using a background conductivity of 1 and a conductivity of 0.3 within the lungs. Images were referenced to the end-expiratory lung impedance value at the onset of the saline injection. $\dot{V}/Q$ images were then generated for each time point as follows: a tidal image was reconstructed from the breath at the lowest section of the saline curve. The perfusion image was reconstructed from the lowest point in the saline curve. Tidal and perfusion images were normalized so that each pixel represented the fraction of the average pixel value. The ratio of pixel values in the ventilation and perfusion images were then obtained to form the $\dot{V}/Q$ image. Changes in $\dot{V}/Q$ ratio over time were analyzed globally and regionally. Six lung regions were segmented by dividing the lungs into left and right then subdividing each lung into ventral, intermediate, and dorsal regions. Data was analyzed with 2-way ANOVA and reported as mean $\pm$ SD. Significance was determined at p < 0.05.

3 Results and Discussion

The global $\dot{V}/Q$ ratio was not different (p = 0.936) at T25 (1.14 $\pm$ 0.13) compared with T50 (1.14 $\pm$ 0.14). Likewise, no regional differences were seen at different times. The mean (T25 + T50) regional magnitude of $\dot{V}/Q$ ratios were therefore reported. In the right lung: ventral = 1.15 $\pm$ 0.07, intermediate = 1.31 $\pm$ 0.13, dorsal = 1.03 $\pm$ 0.04. In the left lung: ventral = 1.18 $\pm$ 0.13, intermediate = 1.16 $\pm$ 0.09, dorsal = 1.01 $\pm$ 0.07. The $\dot{V}/Q$ ratio in the ventral and intermediate regions was higher (p = 0.03) compared with the dorsal region in both lungs. The intermediate region was higher (p = 0.004) than the ventral region only in the right lung.
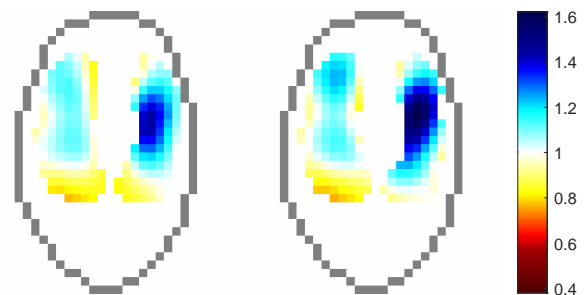
Figure 1: $\dot{V}/Q$ image of one horse at T25 (left) and T50 (right). Pixels values are the ratio of normalized ventilation to normalized perfusion at each time point.

4 Conclusions

EIT can be used to study regional $\dot{V}/Q$ ratios in anesthetized horses. No differences were found related to time, but there was topographic variation.

References

[1] A Adler, WRB Lionheart *Physiol Meas*, 27:S25–S42, 2006
[2] A Auckburally, G Nyman *Vet Anaesth Analg*, 44:397–408, 2017

Enhancing Ultrasound Imaging in Space with EIT

Kendall Farnham[1,3], Ethan K Murphy[1], and Ryan J Halter[1,2]

[1]Thayer School of Engineering, [2]Geisel School of Medicine, Dartmouth College, Hanover, NH USA
[3]kendall.farnham@dartmouth.edu

Abstract: We are combining ultrasound and EIT (US-EIT) to improve image readability for autonomous medical imaging on deep space missions. A 16-channel integrated US-EIT probe has been designed for dual-modality abdominal imaging, and preliminary phantom imaging has been performed using the array.

1 Introduction

A key challenge inhibiting deep space exploration is the danger associated with long duration isolation, microgravity, and radiation exposure, as current medical systems are unable to monitor, diagnose, or treat tissue injury within physical spacecraft constraints and communication limits. Ultrasound is the current imaging system used on the International Space Station, but the image complexity often requires telemedical support for guiding acquisition and diagnosis, making it a challenging solution for deep space[1]. One method to improve ultrasound image readability is to increase the contrast at injury sites with electrical impedance tomography (EIT), as impedance is sensitive to cellular content, blood flow, tissue type, and tissue injury, all of which are relevant for monitoring physiological effects of the space environment (e.g. tissue injury, muscle atrophy, thoracic function, cancer presence) [2]. By combining ultrasound and EIT (US-EIT), we can construct high contrast images for more effective acquisition and interpretation without the need for additional equipment or expertise. We are developing an integrated US-EIT system to provide a low cost, low-resource intuitive imaging solution that can accurately characterize deep internal injury (e.g. detect internal bleeding that needs immediate intervention) while meeting space travel constraints, enabling autonomous medical care for deep space missions.

2 Methods

A 16-channel electrode array has been designed on a flexible printed circuit board (PCB) to fit a C1-6 Flexible US transducer (GE Healthcare) for dual-modality abdominal imaging of deep internal bleeding (Fig 1a-b). To verify the array produces no artifacts on the ultrasound image, abdominal ultrasound images were acquired using the US-EIT probe with and without the electrode array (Fig 1c). For abdominal US-EIT imaging, ultrasound gel is placed under and around the array to maintain proper contact, and a mechanically linked set of distal electrodes is placed opposite the US-EIT probe, forcing current to flow through the anatomy of interest and ensuring sensitivity to deep tissues (Fig 1d). A 3D FEM mesh was developed in MATLAB for constructing images from the 16-channel US-EIT probe (Fig 1e). Phantom imaging experiments have been performed on saline and metal inclusions to validate the probe and mesh (Fig 1f-g), and more extensive testing

with biological phantoms of varying impedance profiles are in progress to determine image accuracy and sensitivity. Software for real-time US-EIT image reconstruction is being developed in MATLAB to overlay the EIT conductivity map on top of the ultrasound image during acquisition, in a sense "highlighting" the injured tissue. An FPGA-based wide bandwidth EIT data acquisition is being developed to integrate directly with state-of-the-art ultrasound equipment for a low-resource imaging system; this system will ultimately be used for validating US-EIT for internal bleeding detection.
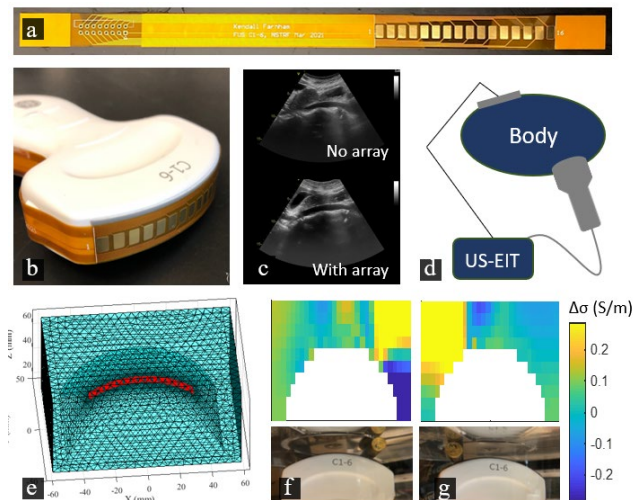
Figure 1: a) 16-channel electrode array on flexible PCB, b) integrated US-EIT probe for abdominal imaging, c) ultrasound image on left abdomen without electrodes (top) vs. with (bottom) showing no electrode artifacts, d) diagram of mechanical linkage system to distal electrodes, e) 3D FEM mesh for image reconstruction with the US-EIT probe, f-g) EIT conductivity image of metal rod in saline correctly tracks the high-conductivity phantom in both locations (image right and left, respectively).

3 Conclusions

Integrating EIT into state-of-the-art ultrasound equipment will provide a low-cost, low-resource medical imaging system that can accurately distinguish internal injury sites while meeting space travel constraints, enabling crew members to be proactive in the event of injury on long-duration deep space missions.

4 Acknowledgements

References

[1] NASA HRP ExMC, Antonsen E. et al (2017) *Evidence Report*, 16-51.
[2] Paulsen K. D. et al (1999) *Proc Annu Int Conf IEEE EMBS* 2012, 6220-6223.

Intradialytic Monitoring of Stroke Volume using EIT

Jin Won Mok,[1] Ju-Young Moon,[2] Ahrim Han,[2] Yang-Gyun Kim,[2] Sang-Ho Lee,[2]

Geuk Young Jang,[1] Tong In Oh,[1] Yongmin Kim,[3] and Eung Je Woo[1]

[1]Department of Biomedical Engineering, College of Medicine, Kyung Hee University, Seoul, Korea, tioh@khu.ac.kr
[2]Diviosn of Nephrologu, Department Internal Medicine, College of Medicine, Kyung Hee Univeristy, Seoul, Korea
[3]Department of Creative IT Engineering, POSTECH, Pohang, Korea

Abstract: Intradialytic hypotension is the most common complication in 20-30% of patients for hemodialysis. A clinical study was conducted to monitor changes in stroke volume using EIT technology in 5 patients who had occurred hypotension during hemodialysis within the last three months. Changes in hemodynamic parameters before and after intradialytic hypotension and treatment intervention were measured and analyzed.

1 Introduction

Hemodialysis (HD) is a treatment for patients with chronic renal failure. HD machines clean the blood by passing it through a dialyzer to diffuse and flush away wastes and excess water from the blood into the dialysate. Intradialytic hypotension (IDH) is considered to be one of the most frequent complications of HD. IDH is associated with a considerable symptom burden and an increased incidence of access failure, cardiovascular events, and mortality [1]. In clinical practice, blood pressure is periodically measured using NIBP (Non-Invasive Blood Pressure) during hemodialysis. However, the patient's hemodynamic status changes rapidly over time, and it is difficult to provide timely patient-specific treatment by monitoring them non-invasively. In this study, hemodynamic parameters extracted from electrical impedance tomographic (EIT) images were collected for five patients who frequently occurred IDH during hemodialysis. Here, we defined IDH as the case where the systolic blood pressure was less than 100 mmHg, and symptoms related to hypotension appeared. Changes in stroke volume and other hemodynamic parameters were measured and analyzed before and after IDH and treatment interventions such as passive leg raising (PLR), decreasing ultrafiltration rate, or lowering the dialysate temperature after hypotension events.

2 Methods

The procedure of the clinical trial is shown in Figure 1. First, we measured the patient's height and weight, and BCM (Fresenius Medical Care, Germany) was measured to assess dry weight and determine the fluid overload. The patient's blood pressure was measured at 20-second intervals using a ClearSight finger cuff and EV1000 (Edwards Lifesciences, USA), and the patient's hemodynamic status was evaluated through echocardiography before and after hemodialysis. In 4 hours of hemodialysis using an HD machine (5008, Fresenius Medical Care, Germany), impedance images were simultaneously acquired at 100 frames/s using a high-speed EIT system (AirTom-R, BiLab, Korea) and a pad electrode that included 16 electrodes. Additionally, blood pressure was periodically measured using NIBP every 30 minutes. The self-reported symptoms and treatment intervention were recorded in the case report.
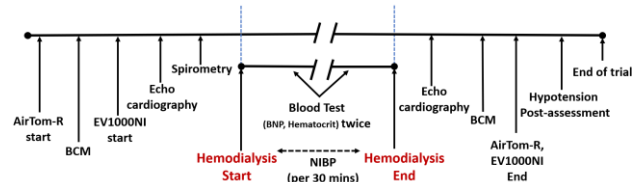
Figure 1: Clinical trial for hemodynamic monitoring during hemodialysis.

We calculated relative thoracic impedance (TI) changes from the reconstructed time-difference EIT images. We adopted the source consistency theory to extract time-series of boundary voltage data associated with cardiac blood flow (cardiac volume signal; CVS) [2]. Stroke volume (SV) and heart rate (HR) signals were derived from CVS waveforms. Five times of HD sessions were monitored for each patient. Nine IDH events occurred in a total of 25 measurements. In Figure 2, extracted TI and hemodynamic parameters (SV and HR) from EIT images measured for 4 hours, and cardiac output (CO) calculated from SV and HR were presented together with BP measured simultaneously. When systolic BP decreased under 100 mmHg, and the patient complained of symptoms such as pain, various treatment interventions were performed. We observed that SV significantly changed before and after the onset of IDH and according to the treatment intervention.
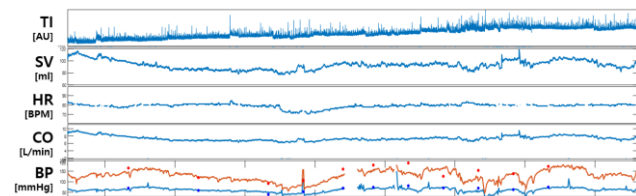
Figure 2: Extracted hemodynamic parameters (TI, SV, HR, CO) from EIT images synchronously measured with BP during hemodialysis.

3 Conclusions

From the results of the clinical study, we showed the possibility of real-time, non-invasive monitoring of hemodialysis patients with rapidly changing hemodynamic parameters using EIT technology. We look forward to developing into clinical technology for predicting IDH or for patient-specific treatment interventions and verification.

4 Acknowledgements

References

[1] Shoji T, *et al.*, *Kidney international*, 66:1212-1220, 2004
[2] GY Jang, *et al.*, *Sci Rep*, 10:11242, 2020

Electrical conductivity of trabecular bone: a preliminar simulation study

Lucas Basiuk[1], C. Manuel Carlevaro[1,2], Ramiro M. Irastorza[1,2]

[1]Grupo de Materiales Granulares, Departamento de Ingeniería Mecánica, FRLP, UTN, La Plata Argentina
[2]Instituto de Física de Líquidos, CONICET, La Plata, Argentina , `rirastorza@iflysib.unlp.edu.ar`

Abstract:

Recents experimental studies show that the electrical conductivity of bone is linearly correlated with the bone volume fraction. This is an interesting result because it can be used together with EIT technology to predict bone health non-invasively. In this work the mentioned linear relationship is numerically evaluated on cancellous bone samples using finite element methods.

1 Introduction

Dielectric properties of bone tissue were extensivelly published in literature [1]. Recently, Balmer et al. [2] have been performed experiments on cortical and cancellous bone to characterize the electrical conductivity. The results were valid for frequenciens circa 100 kHz because at this range the phase shift was approximately zero. The authors correlated the electrical conductivity (σ) of the samples with the bone volume fraction (BV/TV) and obtained the next expression:

$$\frac{\sigma}{\text{Sm}^{-1}} = (0.230 \pm 0.020) - (0.240 \pm 0.026)\frac{BV}{TV}. \quad (1)$$

In this study we intend to contrast the Eq. 1 using numerical models solved by finite element methods. Geometries were obtained from microCT measurements of bovine trabecular bone samples. Two cell models were compared: coaxial and parallel plate resistor (see Fig. 1).

2 Methods

2.1 Samples preparation

Four approximately cylindrical bovine trabecular bone samples (10 mm long, 16 mm diameter) were obtained from the femur head of animals from the local slaughterhouse within less than 24 hours post-mortem (stored at 4 °C). The marrow was removed from the samples, first by ultra-sonication in a 2% tergazyme solution using a B-220 Ultrasonicator (Branson Ultrasonics Americas, Danbury, CT, USA) and micro-CT were obtained using a Bruker SkyScan 1173.

2.2 Computer modeling

The model was based on an electric problem which was solved numerically using the Finite Element Method implemented in FEniCS `https://fenicsproject.org/`. Image processing and meshing were performed on a scikit-image (`https://scikit-image.org/`), 3D Slicer `https://www.slicer.org/`, and Gmsh `https://gmsh.info/`. As the biological medium is considered fully resistive, the problem takes its quasi-static form:

$$\nabla\sigma\nabla V = 0 \quad (2)$$

where σ depends on the position (can be bone matrix or bone marrow). Electric field vector E can be estimated as $E = -\nabla V$. A boundary condition of constant voltage (V_0) was set at the inner boundary (or upper plate) to simulate the active electrode during the electrical measurements, while the voltage at the outer boundary (or bottom plate) was fixed at zero (ground).
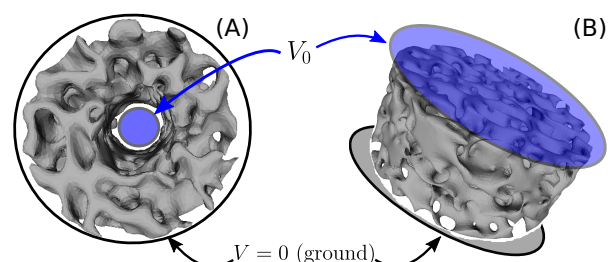
Figure 1: Geometry of the models: (A) coaxial cell and (B) resistor with parallel plates.

Using the two numerical models shown in Fig. 1 we estimate the effective conductivity of the sample by varying the conductivity of two components: bone (σ_b) and bone marrow (σ_m). The procedure is as follows, first we compute the power of the heterogeneus samples (the two geometries (A) and (B)). After that, we fit these values with the computed for homogeneus samples: cylindrical with a hole and cylindrical, respectively.

3 Discussions

Micro-CT based cancellous bone Finite Element models are widely used to estimate bone mechanical properties at tissue level. Regarding the electric properties it is not well stablished yet. In this work we performed simulations in order to validate the experimental results that explain the effective electrical conductivity as a linear function of the bone volume fraction.

4 Acknowledgements

References

[1] B Amin, M A Elahi, A Shahzad, E Porter, M O'Halloran, *Biomedical Physics & Engineering Express*, 5:022001, 2019
[2] T W Balmer, S Vesztergom, P Broekmann, S Stahel, P Büchler, *Scientific reports*, 8:1–8, 2018

Technology of pre- and postoperative monitoring of human lung function based on multi-frequency electrical impedance tomography

Grayr Aleksanyan[1]

[1]Department of Information and Measurement Systems and Technologies, Platov South-Russian State Polytechnic University (NPI),
graer@yandex.ru

Abstract: The paper proposes to conduct pre and postoperative monitoring of human lung function based on multi-frequency electrical impedance tomography (MEIT) using an algorithm for selecting the required frequency of the injected current.

1 Introduction

Electrical impedance tomography [1] has a number of advantages for solving the problems of monitoring the state of the lungs of patients. One of them is the potential for performing studies at different frequencies in order to select the one that is required for a particular person.

2 Methods

2.1 Brief description of the proposed technology

It is proposed to divide the whole process of MEIT measurement into two stages, taking into account the stage of treatment. At the stage of preoperative monitoring (the first stage), the vector of exposure parameters that should be applied to this patient in the future is determined. At the stage of postoperative monitoring (second stage), it is proposed to use the information obtained at the first stage when organizing monitoring of the functional state of the human lungs by the MEIT method. It is proposed to use the frequency of the injected current as a personalization parameter. The key element of the technology is the algorithm for selecting the required frequency of the injected current.

2.2 Development of an algorithm for selecting the required frequency of the injected current

An algorithm is proposed, which consists in calculating the rate of change in the recorded potential difference Ψ_{fk} for a given frequency range of the injected current (f1, f2, …, fk) with the determination of the frequency after which the rate of change of the EIT N potentials is minimal (1).

$$H_i = (\Psi_{(fk+1)} - \Psi_{(fk)}) \rightarrow \min,$$

$$\text{where } i = 1, 2, …, N (1)$$

Next, the injection parameters are reconfigured to the selected frequency and the process of EIT is started.

2.3 Experimental studies of the algorithm

The experimental design included 2 steps. At the first step, the amount of fat mass (M, kg) [2] was determined for each Pi subject using the MEDASS bioimpedance body composition analyzer [3]. Then all Pi were connected to the human lung MEIT information-measuring system. For each of them, EIT studies were performed in the frequency range from 50 kHz to 400 kHz at a current of 5 mA (frequency step 50 kHz). The result sofcalculating N are shown in Figure 1.
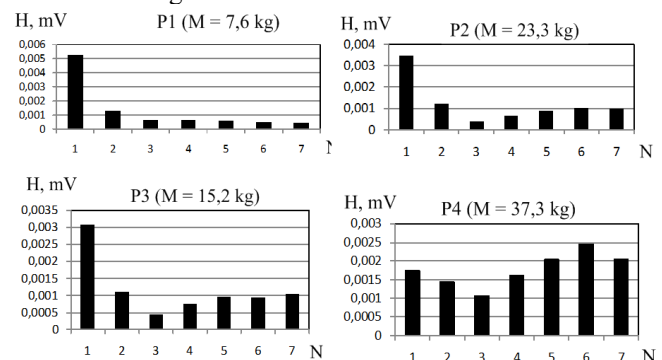
Figure 1: Calculated N value for the subject P1 – P4

3 Conclusions

The personalization approach based on the proposed algorithm solves one of the tasks of the EIT - obtaining an objective assessment of the electrical properties of the internal structures of the object under study. This makes it possible to formulate the initial conditions when starting an EIT study, which is important when implementing the technology for monitoring lung function in the pre and postoperative period. The results show that, by applying expression (1) to the measurement data, it is possible to determine the cutoff frequency of the injection current at which its further increase does not lead to an increase in the sensitivity of the method to the specifics of the object. That is, a frequency is observed after which the minimum deviation of the average values of the recorded potential difference N (for the entire frequency range) practically does not change with increasing frequency.

4 Acknowledgements

References

[1] Pekker, Ya. S., Brazovskiy, K. S., Usov, V. N. (2004). *Electrical impedance tomography*. Tomsk: NTL, 192.
[2] Nikolaev D.V. Bioelectric impedance analysis of human body composition, M. : Nauka, (2009), 392 p.
[3] Nikolaev, D.V. Bioimpedance analysis of the human body composition: Lectures , M.: RIO TSNIIOIZ, (2016), 152 p.

Author Index

EIT 2021

Thank You!

See you next year!